Trans-skull Ultrasound for Imaging and Therapy

A Dissertation
Presented to
The Academic Faculty

By

Scott Schoen Jr

In Partial Fulfillment
of the Requirements for the Degree
Doctor of Philosophy in the
School of Mechanical Engineering

Georgia Institute of Technology

December 2020

Trans-skull Ultrasound for Imaging and Therapy

Approved by:

Prof. Costas Arvanitis, Advisor
School of Mechanical Engineering &
Dept. of Biomedical Engineering
Georgia Tech & Emory University

Prof. Kenneth Cunefare
School of Mechanical Engineering
Georgia Tech

Prof. F. Levent Degertekin
School of Mechanical Engineering
Georgia Tech

Prof. Stanislav Emelianov
School of Electrical Engineering,
Dept. of Biomedical Engineering &
Dept. of Radiology
Georgia Tech & Emory University

Prof. Karim Sabra
School of Mechanical Engineering
Georgia Tech

Date Approved: November 17, 2020

There are some enterprises in which a careful
disorderliness is the true method.

—Herman Melville, *Moby-Dick*

To Mom & Dad
who have made everything possible

Acknowledgements

It would be difficult to overstate the importance to this thesis of my advisor, Dr. Costas Arvanitis. The results presented herein would likely never have been reached without his continuous discussion, direction, guidance, and insight provided during the last four years. His counsel, encouragement, advice, and example have been superlative, and I am fortunate to have been their beneficiary. In science or in life, I will now forever have the instinct to step back, consider the big picture, and solve the first-order problem to start. Any capability I will have now or in the future is, largely, his doing.

I would also like to thank my committee members, Drs. Ken Cunefare, Levent Degertekin, Stas Emelianov, and Karim Sabra whose guidance during the completion of my studies has made the presentation (I hope) better motivated, directed, and substantiated.

I will be quite sad to leave the Ultrasound Biophysics Lab, whose diversity of interest, expertise, and background has informed—both directly and indirectly—the development of my research. Dr. Anastasia Velalopoulou, Zhigen Zhao, Henry Lee, Arpit Patel, Chulyong Kim, Ashley Alva, Pradosh Dash, and Dr. Kong Wong (*honoris causa*) were excellent labmates all. And special thanks to my deskmate, classmate, and friend Yutong Guo, without whom navigating requirements, qualifying exam revision, and math classes would have been significantly more trying. Thanks also to my fellow students and ASA members who were invaluable resources throughout, especially Drs. Thomas Bowling, Matt Fronk, Bowen Jing, Charlsie Lemons, Brendan Nichols, Aprameya Satish, Chris Sugino, David Tan, & Yusuf Yaras as well as Ahmed Allam, Graham Collins, Steven Craig, Nick Durofchalk, Sait Kilnic, Jae-Kang Kim, Rossie Nho, Sush Surappa, Phoebe Welch, and Yingdan Wu.

Research requires funding, and the the National Science Foundation, National Institutes of Health, and Focused Ultrasound Foundation have provided the very concrete support on which any progress is based. Additionally, the Georgia Tech Student Government Association & College of Engineering, CRIDIC, the International Society for Therapeutic Ultrasound, the National Council of Acoustical Consultants, and the Acoustical Society of America supported many of the conference presentations that promoted the development of this research. I am thankful also for the Institute's facilities and administration that has made this work possible, and whose considered navigation was commendable during what I hope is the most trying time the world will see in my lifetime. I am also thankful to Camellia Henry, Dr. Laxminarayanan

Krishnan, and Joi Outlaw, whose assistance facilitated nearly very experiment and conference participation during my time at Georgia Tech.

Moving to Atlanta was hard, and I am indebted to those who made this transition more manageable, especially Dr. Mustafa Abassi, Dr. Wing Li, Peter & Leslie Nevels, Darrell Smit, Dr. Ben Treweek, and most especially my once and current roommate, Chris McKay (and his son Nico). Last, and possibly most, thank you to my family: Nancy, Scott, Katie, Jeff, Sarah, Anton, Tyler, Aidan, Sophie, Sadie, and Gavin, whose love and support over the last four years has made completion of this program a reality.

Finally, to Cassie. To list everything would double my page count.
I venture to say only: thank you. For everything.

No citations to Newton, Gauss, Euler, or Helmholtz appear in the bibliography, despite that their insights and influence suffuse the entirety of the work recounted here. In much the same way, the importance of countless family members, friends, teachers, coworkers, and mentors in Boston, Austin, and Atlanta not listed here to every aspect of my development as a person is implicit, but absolutely essential. I have been supremely fortunate to be close to almost exclusively excellent people, and to all of them I am obliged and grateful.

Contents

List of Tables

List of Figures

List of Abbreviations

ASA	Agular Spectrum Approach
CAM	Chorioallantoic Membrane
CEUS	Contrast-Enhanced Ultrasound
CFL	Courant–Friedrichs–Lewy (Condition)
CNR	Contrast-to-Noise Ratio
CT	Computed Tomography
DICOM	Digital Imaging and Communications in Medicine
EMST	Euclidean Minimum Spanning Tree
$F\#$	F-number (Ratio of Aperture to Focal Distance)
FFT	Fast Fourier Transform
FUS	Focused Ultrasound
MRI	Magnetic Resonance Imaging
PAM	Passive Acoustic Mapping *or* Passive Acoustic Map
PCD	Passive Cavitation Dectection
PCI	Passive Cavitation Imaging
PSF	Point Spread Function
PRF	Pulse Repetition Frequency
HASA	Heterogeneous Angular Spectrum Approach
MR	Morphological Reconstruction
MRI	Magnetic Resonance Imaging
SNR	Signal-to-Noise Ratio
SR	Super-resolution
SVD	Singular Value Decomposition
ULM	Ultrasound Localization Microscopy

SUMMARY

Ultrasound has emerged as a novel modality for the treatment and imaging of brain diseases. When enhanced by circulating microbubble agents, which scatter sound and vibrate in response to the incident ultrasound, it can enable a range of new therapeutic interventions and open new possibilities for imaging. Despite these advancements, the skull remains a major challenge both for therapy and imaging. This work proposes methods for fast, frequency-selective passive reconstruction of the acoustic field through human skull with applications including improved targeting for exploitation of nonlinear acoustic effects in the brain, controlling the microbubble dynamics, and super-resolution imaging.

"There may be alſo a Poſſibility of
diſcovering the Internal Motions and
Actions of Bodies by the ſound they make..."

—Robert Hooke, *Posthumous Works* (1705)

Chapter 1
Introduction and Background

The use of ultrasound as a medical imaging modality has become nearly ubiquitous in the last half-century, largely due to its large tissue penetration depth, low cost, and use of non-ionizing radiation.[1] More recent work has also demonstrated the utility of higher intensity ultrasonic fields for therapy, exploiting mechanisms as thermal ablation,[2] shock-wave pulverization,[3,4] and cavitation-aided liquefaction.[5] While ultrasound-mediated imaging and therapeutic techniques have seen broad clinical adoption, their use toward diagnosis and treatment of central nervous system diseases is significantly more limited due to the brain's robust and relatively impervious-to-sound encasement: the skull.

Through significant technological advancement in the last two decades, use of focused ultrasound (FUS) has enabled successful pilot studies toward the treatment of central nervous system diseases in humans.[6] Some techniques exploit controlled deposition of thermal energy,[7–11] while in others, stabilized microbubble contrast agents are used to induce localized mechanical forces to disrupt temporarily the blood-brain-barrier (BBB) with the aim of improving delivery and uptake of therapeutics.[12–14] Moreover, with current methods for corrected focusing through the skull, only a small part at the center of the brain can be treated. Hence different aberration correction methods that will potentially allow to expand the treatment envelope of current FUS systems are urgently needed in order to utilize the potential of this technology to the treatment of brain diseases. Additionally, to ensure treatment safety and efficacy, monitoring and control of the acoustic field is paramount.

Extant active acoustic imaging methods are largely ineffective for trans-skull applications: the impedance contrast presented by the skull has required workarounds such as thinning of the bone;[15] restriction to only the thinnest region of the skull (temporal window);[16] craniectomy to create an acoustic window;[17] or use in infants whose skulls are not fully formed.[18] Passive (i.e., listen-only) acoustic mapping methods have, at the cost of degraded resolution, demonstrated successful imaging through the skull.

However, current approaches[19,20] are computationally expensive, and have yet to be demonstrated with sufficient speed for real-time imaging, a necessity for therapeutic guidance. Therefore, efficient methods for imaging of the acoustic field through the skull are needed.

Addressing these challenges requires considered manipulation of ultrasound in the highly heterogeneous and complex acoustic environment represented by the skull. Thus, the immediate task is to understand and predict the propagation of these pressure waves. While full-waveform modeling[21–23] has made great strides in recent years, the size of the skull (~10 cm) is very large compared to the wavelength at the megahertz frequencies of interest (~1 mm). Thus representing the full geometry with simulation the requisite grid sizes—especially for realistic 3D environments—becomes intractable without recourse to specialized computing resources. Spectral approaches have been proposed to enable fast prediction[24] and reconstruction[25] of the acoustic field, but their derivations assume a homogeneous medium.

The central innovation of this work is extension of the frequency domain angular spectrum approach to account for heterogeneity of the medium—i.e., the presence of the skull in the region of interest. Following the derivation of the heterogeneous angular spectrum approach in Chap. 2, several applications to existing challenges in brain imaging and therapy are explored. Specifically, first the improvements enabled for focusing (Chap. 3) and passive acoustic mapping (Chap. 4) are evaluated. Next, given the relatively low resolution of passive maps, complementary methods based on recent techniques for improving the effective resolution are investigated (Chap. 5). Finally the feasibility of the improved focusing method is discussed toward targeted, low-frequency applications through exploitation of nonlinear acoustic phenomena (Chap. 6).

Chapter 2
The Heterogeneous Angular Spectrum Approach

2.1 Introduction

Most generally, the angular spectrum approach (ASA) is a method of solving the wave equation in the spatial frequency domain.[26] It may be considered a decomposition of the harmonic field[†] into plane waves that travel with a continuous spectrum of directions, with appropriate phases and amplitudes such that their summation yields fields of arbitrary spatial distribution.[27] Plane waves are mathematically convenient, as the propagation through space of each component may be modeled with a simple phase delay. Coupled with fast Fourier transform (FFT) algorithms,[28] the method enables exceptionally efficient computations and is naturally suited to real-time applications. In addition to generating specific field patterns, of particular interest for the ASA here is the recovery of the volumetric wave field from a surface measurement of the phase field (i.e., boundary condition), a process known as holography.[29]

However a major limitation of the ASA for biomedical acoustics is the assumption of a homogeneous medium. While the method is relatively robust to weak heterogeneity (density and compressibility changes on the order of a few percent) its performance in more complex environments, including that represented by the intervening skull, suffers from distortion caused by significant refraction and attenuation of the acoustic energy—effects not accounted for in its formulation.

In this chapter, a governing equation for the ASA in a heterogeneous medium is derived, and solutions are presented with general numerical algorithm, and an analytical result valid for a stratified medium. To prevent distraction from the through line of the derivations, the bulk of the evaluations and low-level details have been relegated to Appendix A; see there for full details.

[†]For linear acoustic propagation, the restriction to a single frequency does not sacrifice generality, as arbitrary finite duration time series may be written as summation of their Fourier series.

2.2 Canonical Formulation

Notation Convention Throughout this thesis, a negative time convention is used. That is, a harmonic function $f(t) = f_0 \cos \omega t$ will be written $f(t) = f_0 e^{-i\omega t}$, where the real part of f is to be taken implicitly. The choice is arbitrary, but dictates the sign of the kernel in the temporal and spatial Fourier transform pairs. Thus herein

$$\mathcal{F}[\,\cdot\,] \equiv \int_{-\infty}^{\infty} (\,\cdot\,) e^{i\omega t}\,\mathrm{d}t \tag{2.2.1}$$

$$\mathcal{F}_k[\,\cdot\,] \equiv \iint_{-\infty}^{\infty} (\,\cdot\,) e^{-i(k_x x + k_y y)}\,\mathrm{d}x\,\mathrm{d}y \tag{2.2.2}$$

Results for the positive time convention $\propto \exp +j\omega t$ can be obtained from the presented results via the substitution $i \to -j$.

The acoustic pressure p of interest is taken to be governed by the homogeneous wave equation[†]

$$\nabla^2 p - \frac{1}{c_0^2}\frac{\partial^2 p}{\partial t^2} = 0\,, \tag{2.2.3}$$

where c_0 is the (constant) small-signal sound speed. Since linear propagation is assumed, it is sufficient to consider a single frequency pressure wave, as arbitrary time series signals may be assembled from these harmonic components. Taking the temporal Fourier transform of Eq. (2.2.3) and use of the fact that $\mathcal{F}[\partial^2 p/\partial t^2] = -\omega^2 \tilde{p}$ [‡] gives the homogeneous Helmholtz equation

$$(\nabla^2 + k^2)\tilde{p} = 0\,, \tag{2.2.4}$$

where $\tilde{p} = \mathcal{F}[\,p\,]$ and $k \equiv \omega/c_0$ is the wavenumber. The ASA is derived by applying

[†]Equation (2.2.3) is valid for small-signal (linear) pressure waves in a lossless, inviscid, homogeneous medium. This chapter specifically address the latter requirement; restrictions imposed by the other assumptions are discussed in Sec. 2.7.

[‡]Note that p may be written as the inverse transform

$$p = \mathcal{F}^{-1}[\,\tilde{p}\,] = \frac{1}{2\pi}\int_{-\infty}^{\infty} \tilde{p}\, e^{-i\omega t}\,\mathrm{d}\omega\,,$$

so that

$$\frac{\partial p}{\partial t} = \frac{\partial}{\partial t}\left[\frac{1}{2\pi}\int_{-\infty}^{\infty} \tilde{p}\, e^{-i\omega t}\,\mathrm{d}\omega\right] = \frac{1}{2\pi}\int_{-\infty}^{\infty} -i\omega\tilde{p}\, e^{-i\omega t}\,\mathrm{d}\omega = \mathcal{F}^{-1}[\,-i\omega\tilde{p}\,]\,.$$

Taking the forward transform of this expression gives $\mathcal{F}[\partial p/\partial t] = -i\omega\tilde{p}$, i.e., that time derivatives of p become multiplications by $-i\omega$ in the frequency domain.

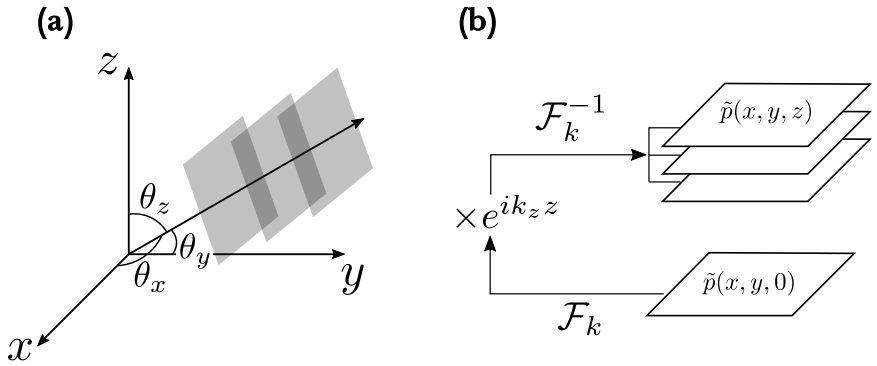

Figure 2.1: **(a)** Geometric interpretation of the wavenumber directional components. **(b)** Propgation of the field via multiplication by a transfer function in the spatial frequency domain.

the spatial Fourier transform $\mathcal{F}_k$ to to yield an ordinary differential equation for its angular spectrum $P(k_x, k_y, z) = \mathcal{F}_k[\,\tilde{p}\,]$

$$\frac{\mathrm{d}^2 P}{\mathrm{d}z^2} + k_z^2 P = 0\,, \tag{2.2.5}$$

where $k_z^2 = (\omega/c_0)^2 - k_x^2 - k_y^2$.

By application of the temporal and spatial transforms, the multivariate partial differential wave equation [Eq. (2.2.3)] has been transformed to an ordinary differential equation in z [Eq. (2.2.5)]. Note however that there is no computational advantage to this transformation in principle; while Eq. (2.2.5) is simpler to solve, a solution must be found for all temporal frequencies ω and for each set of spatial frequencies (k_x, k_y) corresponding to that frequency, and then their inverse transforms superimposed. However, in many applications, only a small band of frequencies are of interest and thus only a small subset of the data must be processed. This reduction comes at the cost of performing a Fourier transform of the data, but the ready availability of fast Fourier transform (FFT) implementations makes this an attractive trade-off.

The term "angular spectrum" is used since the transformation from $\tilde{p}$ to P is mathematically equivalent to writing the field as a continuous distribution of plane waves with a spectrum of wavenumbers $(k_x,\ k_y)$. From the identity $(\omega/c)^2 = k_x^2 + k_y^2 + k_z^2$, each of these wavenumbers are associated with an angle, which describe the direction of propagation of the plane wave component, i.e., $\cos\theta_i = k_i/k_0$ as shown in Fig. 2.1(a). Plane waves are exceptionally convenient mathematically, as their value at any point in space can be found via a simple phase shift $\boldsymbol{k}\cdot\boldsymbol{r}$, where $\boldsymbol{k} \equiv k_x\boldsymbol{e}_x + k_y\boldsymbol{e}_y + k_z\boldsymbol{e}_z$. Thus, if the pressure field is measured at some reference plane $z = 0$ (i.e., at the transducer face), and its angular spectrum at that plane $P_0 = P(k_x, k_y, 0)$ is computed. If there

are no backward-travelling waves, then Eq. (2.2.5) has the solution

$$P = P_0\, e^{ik_z z}\,. \tag{2.2.6}$$

The full acoustic field in any plane may then be reconstructed with Eq. (2.2.6) and evaluation of the inverse transform.

The efficiency of the ASA toward biomedical ultrasound applications compared to, e.g., delay-and-sum beamforming methods (see Chap. 4) lies in the fact that the shift and sum operation represents a convolution that is converted to a multiplication in the frequency domain. Additionally, the spectral selectivity means that only the frequencies of interest need be manipulated, rather than the entire time series for every receiver channel.

2.3 General Heterogeneity

Equation (2.2.6) is derived in the case that c_0 is a constant material property. In the case that the sound speed $c(\boldsymbol{r})$ changes slowly compared with the wavelength,[†] propagation may be described by $[\nabla^2 + \omega^2/c^2(\boldsymbol{r})]\tilde{p} = 0$. Then application of the spatial transform yields

$$\frac{\mathrm{d}^2 P}{\mathrm{d}z^2} + k_z^2 P = \Lambda * P\,. \tag{2.3.1}$$

In Eq. (2.3.1), $\Lambda = \mathcal{F}_k\left[k_0^2(1-\mu)\right]$, $k_0 = \omega/c_0$, $\mu = c_0^2/c^2$, c_0 is a reference (average) sound speed, and $*$ denotes a 2D convolution over the wavenumber components k_x and k_y. Comparing with Eq. (2.2.5), the heterogeneity appears as a source term in the governing equation. In the general case, the implicit solution of Eq. (2.3.1) may be obtained with a Green's function technique[30–32] to give, for the same source conditions,

$$P = P_0 e^{ik_z z} + \frac{e^{ik_z z}}{2ik_z}\int_0^z e^{-ik_z z'}\,(\Lambda * P)\,\mathrm{d}z'\,. \tag{2.3.2}$$

[†]The specific requirement is that $|\nabla\rho/\rho + 2\nabla c/c|(\omega/c) \ll 1$; see Appendix B.1. Thus while strictly it is *independently* required that the density varies slowly, the density and sound speed are intrinsically related through $c_0^2 = K/\rho_0$, where K is the bulk modulus of the fluid.

While Eq. (2.3.2) remains implicit, approximation of the integral with a first order Riemann sum may then be used to compute P at arbitrary z via

$$P^{n+1} \approx P^n e^{ik_z \Delta z} + \frac{e^{ik_z \Delta z}}{2ik_z} \, (P^n * \Lambda) \times \Delta z \,, \tag{2.3.3}$$

where $P^n = P(k_x, k_y, n\Delta z)$. The use of the first-order approximation to replace the integral imposes restrictions on the choice of step size Δz. Fundamentally, it is governed by the gradient of the medium heterogeneity with respect to the wavelength. A more detailed consideration is given in Appendix A.3.1, but as a general rule use of Δz less than 1/6 of the wavelength will give reasonable results.

2.4 Stratified Heterogeneity

In the special case of a stratified medium, i.e., one whose sound speed is a function only of the axial coordinate z, then the convolution in Eq. (2.3.1) may be evaluated[33,34] to give

$$\frac{\partial^2 P}{\partial z^2} + k_z^2 P - \lambda \, P = 0 \,, \tag{2.4.1}$$

where $\lambda = \mathcal{F}_k^{-1}[\Lambda] = k_0^2(1 - \mu)$. Assuming a solution of the form $P = A(k_x, k_y, z) \, e^{ik_z z}$ (WKB method[35]), and retaining only first-order terms[†] the solution for the angular spectrum is then

$$P = P_0 \exp \left[i \left(k_z z - \frac{k_0^2}{2k_z} \int_0^z 1 - \mu(z') \, \mathrm{d}z' \right) \right] . \tag{2.4.2}$$

Note that for a homogeneous medium, then $\mu = 1$, and the uniform case [Eq. (2.2.6)] is recovered.

2.5 Comparison of Results

Reference 36 presents a general forward simulation scheme that includes nonlinearity and attenuation. In the absence of these effects, Eq. (12) of that reference becomes

[†]Discarding the second derivative term specifically requires that $|(k_0^2/k_z^2)(1 - \mu)| \ll 1$; see Appendix A.3.2. Thus for $k_0 \sim k_z$ (paraxial approximation), this requirement is that $\mu \equiv (1 + c'/c_0)^{-2} \simeq 1 - 2c'/c_0 \sim 1$, i.e., that the relative magnitude of the sound speed changes should be small. Thus the stratified correction is more restrictive than the general case, as it is valid when the speed of sound changes are both gradual and small. The general case requires only the former condition.

(with the present notation)

$$M = \mathcal{F}_k \left\{ \left[k_0^2 \left(1 - c_0^2/c^2 \right) \right] \times \tilde{p} \right\} = \Lambda * P \,. \tag{2.5.1}$$

Substitution of this M into Eq. (11) of Ref. 36 recovers Eq. (2.3.2) obtained here, indicating the consistency of the results.

To compare the stratified result with the general case Eq. (2.3.3), rewrite Eq. (2.4.2) as

$$P = P_0 e^{ik_z z} \exp \left[\frac{1}{2ik_z} \int_0^z \lambda(z') \, \mathrm{d}z' \right] . \tag{2.5.2}$$

Expansion of the exponential term (justified below) gives

$$P \simeq P_0 e^{ik_z z} \left[1 + \frac{1}{2ik_z} \int_0^z \lambda(z') \, \mathrm{d}z' + \dots \right] . \tag{2.5.3}$$

Retention of first order terms and approximation the integral as a left Riemann sum gives

$$P^{n+1} \simeq P^n e^{ik_z \Delta z} + \frac{e^{ik_z \Delta z}}{2ik_z} P^n \lambda(z) \, \Delta z + \mathcal{O}\left[(\Delta z)^2 \right] . \tag{2.5.4}$$

In the stratified medium case, $\Lambda * P = \lambda P$, so that Eq. (2.3.3) agrees with Eq. (2.5.4) to $\mathcal{O}\left[(\Delta z)^2\right]$—which is the expected result as it is the first order solution of Eq. (2.4.1). Use of the truncated expansion in Eq. (2.5.3) requires that

$$\frac{1}{4} \left(\frac{k_0}{k_z} \right)^2 \left[k_0 \int_0^z (1 - \mu) \, \mathrm{d}z \right]^2 \ll 1 \,. \tag{2.5.5}$$

In the far field (the region of interest for most biomedical applications), the paraxial approximation dictates that first term is of order 1. Equation (2.5.5) is true then if $\mu \approx 1$, i.e., for relatively weak inhomogeneity—which is the condition under which the wave equation with $c \to c(\boldsymbol{r})$ is valid.[37]

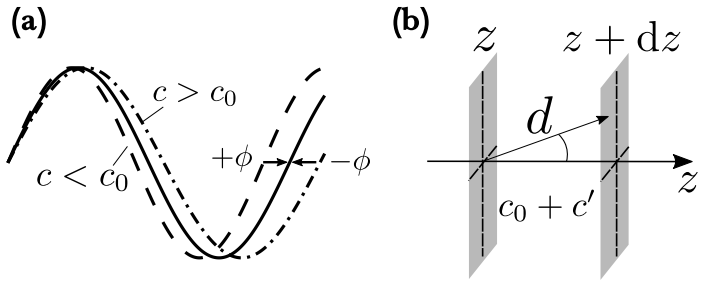

FIGURE 2.2: **(a)** The first term in the phase correction described by Eq. (2.5.8) is due to the dilation or contraction of the wavelength due to the change in sound speed c. **(b)** The second term in Eq. (2.5.8) accounts for the distance d between z values for the plane wave component having an orientation defined by k_z.

2.5.1 Interpretation of Results

By inspection, Eq. (2.4.2) represents a phase delay ϕ to the homogeneous medium case of

$$\phi = \frac{k_0^2}{2k_z} \int_0^z 1 - \mu(z')\,\mathrm{d}z' \,. \tag{2.5.6}$$

Equation (2.5.6) may be thought of as accumulation of phase shifts incurred as the wave travels through an infinitesimal width $\mathrm{d}z$, i.e., $\phi = \int \mathrm{d}\phi$, such that

$$\mathrm{d}\phi = (k_0^2/2k_z)\,(1-\mu)\;\mathrm{d}z \,. \tag{2.5.7}$$

Since Eq. (2.4.2) required that c'/c_0 is small, $\mu(z) \equiv (1 + c'/c_0)^{-2}$ can be expanded so that

$$\begin{aligned} \mathrm{d}\phi &\simeq \frac{k_0^2}{2k_z}\left[1 - \left(1 - 2\frac{c'}{c_0}\right)\right]\mathrm{d}z \\ &\simeq \frac{k_0^2}{2k_z}\left(2\frac{c'}{c_0}\right)\mathrm{d}z = \left(\frac{c'}{c_0}k_0\right)\left(\frac{k_0}{k_z}\,\mathrm{d}z\right) \,. \end{aligned} \tag{2.5.8}$$

The term $(c'/c_0)k_0$ has the form of an effective wavenumber, accounting for the dilation or contraction of the wavelength due to the difference in sound speed from c_0 [Fig. 2.2(a)]. The second term $(k_0/k_z)\,\mathrm{d}z$ is the distance between the two infinitesimally separated planes for a plane wave traveling with propagating wavenumber k_z. The extra phase then assumes the familiar form $\phi \sim k_{\mathrm{eff}} d$, see Fig. 2.2(b). With these solutions for the ASA in heterogeneous media in hand, their application to problems in trans-skull ultrasound are now considered; namely efficient focusing to correct for dis-

tortions induced by the skull; passive beamforming for source localization accounting for aberration induced by the same; improving the effective resolution of the obtained images of the vasculature; and evaluating the feasibility of nonlinear acoustic effects in the brain.

2.6 Effects of Discretization

Before considering applications of the theory, some practical details of its implementation should be addressed. The formulation of the ASA and HASA in this chapter has thus far assumed that the full, continuous pressure field is known at every point in the $z = 0$ plane for all time. However, in any practical application, the field is discretely sampled in time (digital conversion) at a finite number of receiver positions (due to the limited spatial extent of the transducer and the discrete positions of each element).

The effects of temporal discretization are perhaps more familiar, and for which the Shannon-Nyquist[†] theorem[39,40] states that accurate reconstruction of a discretely sampled function requires the continuous signal to be sampled at a rate at least twice that of the highest frequency contained in the signal for accurate reconstruction from its Fourier series. The spatial analog is a consequence of the same theory; namely that reconstruction of a spatial signal with highest spatial frequencies k_x and k_y, must be sampled at intervals Δx and Δy that satisfy[41]

$$\Delta x \leq \frac{\pi}{|k_x|} \quad \text{and} \quad \Delta y \leq \frac{\pi}{|k_y|}\,. \tag{2.6.1}$$

Equivalently, this requirement is that field is sampled at least twice per wavelength, since $|k_x| \leq |k| = 2\pi/\lambda$. Note however that this statement represents a lower bound on the sampling (i.e., any field with wavelength λ may be reconstructed with this sampling). But, for the transverse components of the wavenumber $k_x, k_y \propto k_0 \sin(\theta)$, where θ is the azumuthal angle; thus if the received wavefronts are approximately normal to the receiver plane, then these wavenumbers will be appreciably smaller than

[†]The conventional name is used here, though as noted by Ref. 38, the naming convention rarely captures the nuance of its development:

> *The numerous different names to which the sampling theorem is attributed in the literature—Shannon, Nyquist, Kotelnikov, Whittaker, to Someya—gave rise to [...] discussion of its origins. However, this history also reveals a process which is often apparent in theoretical problems in technology or physics: first the practicians put forward a rule of thumb, then the theoreticians develop the general solution, and finally someone discovers that the mathematicians have long since solved the mathematical problem which it contains, but in "splendid isolation."*

k_0, and the spatial variation of the field will be appreciably larger than λ. Therefore, spatial sampling of the field may be coarser than two samples per wavelength, at the cost of reduced angular resolution.

The separate issue of a spatially finite sampling of the field must also be considered. Mathematically, the effect of a measurement by an aperture of length L may be seen by application of a window function (i.e., $\mathrm{rect}(x)$, defined to be unity for $|x| < 1$ and 0 otherwise) to the full field. In 1D, this becomes

$$P_0 = \mathcal{F}_k \left[\mathrm{rect}\left(\frac{x}{L}\right) \cdot \tilde{p}(x) \right] = P * L \,\mathrm{sinc}\, \frac{k_x L}{2} \,. \tag{2.6.2}$$

When $k_x L \lesssim 1$ the aperture has the effect of introducing spatial frequencies not present in the true signal.[†] This effect can be mitigated with the use of zero padding. That is, L may be made arbitrarily large by assuming the field vanishes everywhere outside the aperture, i.e., computationally appending 0s to the measured data; see Fig. 2.3(a). Qualitatively, this approximation requires that any sources of interest lie squarely within view of the aperture.

Some care must be taken in the padding, since assumption of a vanishing field for $|x| > L/2$ may introduce sharp changes in the boundary condition. Representing this field in the spatial frequency domain requires very high spatial frequencies, whose propagation may introduce significant errors in the reconstructed field. Mathematically, these effects are identical to spectral leakage due a rectangular apodization function in time series analysis. To avoid such artifacts, the measured data are windowed, such the pressure amplitudes decay smoothly to 0 at the ends of the aperture. A Tukey window is typical for applications,[41,42] namely,

$$W(x) = \begin{cases} \frac{1}{2}\left\{1 + \cos\left[\frac{2\pi}{\xi L}\left(x + \frac{1-\xi}{2}\right)\right]\right\} & x \in \left[-L/2,\, L(\xi-1)/2\right) \\ 1 & x \in \left[L(\xi-1)/2,\, L(\xi+1)/2\right] \\ \frac{1}{2}\left\{1 + \cos\left[\frac{2\pi}{\xi L}\left(x - \frac{1-\xi}{2}\right)\right]\right\} & x \in \left(L(\xi+1)/2,\, L\right] \end{cases} , \tag{2.6.3}$$

where ξ is a parameter representing the fraction of L over which a cosine taper is applied. For $\xi = 0$, Eq. (2.6.3) gives a rectangular window, while for $\xi = 1$ gives a cosine window, see Fig. 2.3(b). With these concerns in mind, for all results that employ the ASA or HASA presented herein, the following processing steps have been applied in the numerical implementation

[†]Conversely, note that as $L \to \infty$, the second term approaches a delta function $L\,\mathrm{sinc}\,\frac{k_x L}{2} \to \delta(k_x)$. And since $P * \delta(k_x) = P$, an infinite aperture recovers the continuous result,

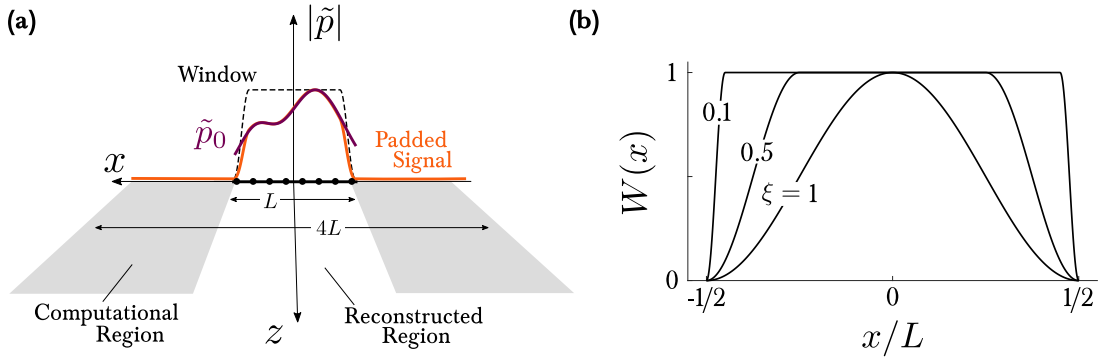

FIGURE 2.3: **(a)** Schematic of computational domain for reconstructions and effect of windowing. **(b)** Tukey window functions [given by Eq. (2.6.3)] for the indicated values of ξ.

1. Measured data have been zero padded such that the size of the padded aperture is four times the width of the physical aperture [Fig. 2.3(a)].

2. A Tukey window with $\xi = 0.25$ was applied to the measured data.

Thus while for simplicity P_0 is taken to mean $\mathcal{F}_k\left[\tilde{p}(x, y, 0)\right]$, it is strictly the padded, apodized version given by Eq. (2.6.2). The stated conditions are not necessarily optimal for all cases, but represent a reasonable values to limit the number of variables for different applications, and were seen to give reasonable results for axial distances on the order of the array aperture (i.e., for $z \sim L$).

2.7 Summary of Contributions

Presented in this chapter were two results that enable extension of the fast, frequency domain angular spectrum approach to account for propagation in heterogeneous media. The first, given by Eq. (2.3.3) is a numerical approach that marches in the axial direction z and accounts for arbitrary spatial variation of the sound speed c_0, provided these variations occur over scales that are large with respect to the wavelength. The second, Eq. (2.4.2), is an analytical correction to the phase of the angular spectrum, and is valid when the sound speed varies only in the direction perpendicular to the initial condition, and when the magnitude of these changes are small (i.e., $|(c - c_0)/c_0| \ll 1$). Coupled with considerations for their practical implementation (Sec. 2.6), these techniques may now be evaluated for applications in several aspects of trans-skull ultrasound.

Chapter 3
Efficient Transcranial Focusing

3.1 Introduction

The use of focused ultrasound to manipulate brain tissue through the skull acoustically is of significant clinical interest. The potential of focused ultrasound to create isolated regions of high temperature or mechanical force noninvasively was realized nearly a century ago;[43,44] however its use for applications in brain diseases has been stymied by the skull effects: namely the reflection, refraction, and absorption of acoustic energy.[45] Early approaches for FUS in the brain used a single or a few radiating piezoelectric elements, and required removal of portions the skull near the treatment area.[46–48] While single element, trans-skull focusing was demonstrated[49,50] skin burns[51] and skull heating due to acoustic absorption[52] prevented clinical adoption. In addition to absorption, aberration caused by distortions of the field due to the skull, cause a loss of coherence and a shifted or weakened focal region,[53] a problem that also complicates trans-skull mapping (see Chap. 4). In this chapter, current challenges for fast calculation of focal corrections to handle the skull are introduced, and the HASA developed in the previous chapter is evaluated for its ability to compute these corrections efficiently.

3.1.1 Transcranial FUS Therapy

Advances in transducer technology eventually enabled construction of arrays of individual elements whose phases could be controlled independently, leading to methods to correct for skull aberrations.[54–56] While these corrections nominally required invasive measurement,[55] the use of MRI or CT for image guidance[53,57–59] allowed these corrections via simulation.[60] Subsequently, hemispherical arrays,[61–63] whereby tens to hundreds of individual elements are arranged concentrically with diameters of about 30 cm, were developed. These arrays distribute the transducers over a large area, so as to reduce skull heating, and allow implementation methods to correct aberrations, and

thus provided the basis for the first clinical uses.[7] Currently, these systems are in use to treat essential tremor,[9,64] and chronic pain,[8,65,66] while ongoing work is evaluating its use in treating Alzheimer's disease,[14] depression,[67,68] and Parkinson's disease.[69]

While great strides have been made to date, hemispherical arrays are limited to the central region of the brain for thermal ablation, necessitate liquid cooling of the skull, and require expensive MRI guidance.[70,71] Single element techniques have also found uses at lower intensities for neuromodulation[72] and BBB disruption with intracranial implants[12] in humans. Additionally, recent novel fabrication techniques have enabled realization of transducers for imaging[72–75] and therapy[76–78] hold promise for further innovation and enabling of US guidance. Many of these applications take advantage of recent developments in microbubble contrast agent technology, which enable further enhancement and localization of the mechanical and thermal effects of FUS.[79] However, to enable adaptive focusing at the periphery of the brain and at shorter timescales, efficient accurate methods for transcranial focusing are needed.

In this chapter, the heterogeneous angular spectrum approach from Chap. 2 is applied to trans-skull focusing. First, phase and amplitude shadings are extracted from the field predicted with HASA. Then, with numerical simulations, the improvement in focal accuracy, intensity, and distributions are evaluated as functions of array aperture, and frequency. Finally, the efficiency of the focusing technique is considered.

3.2 Theory and Methods

3.2.1 Focusing in With Phased Arrays

Phased arrays allow independent control of individual elements of the transducer, and thus the ability to steer and focus the resulting field. For the case of a homogeneous medium with speed of sound c_0, the distance from each element n to the target focus position (x_f, z_f) is

$$r_n = \sqrt{(x_n - x_f)^2 + z_f^2}, \tag{3.2.1}$$

since the array is taken to be aligned with $z = 0$ (see Fig. 3.1). Thus, if the identical transmitted signals for each element n are delayed in time by

$$\tau_n = \frac{r_n}{c_0}, \tag{3.2.2}$$

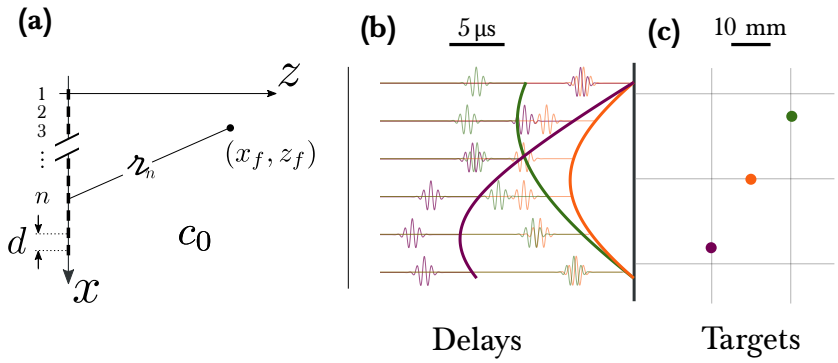

FIGURE 3.1: **(a)** For a desired focal target (x_f, z_f), the travel time from each element n may be calculated. **(b)** Delaying the transmitted signals from each element by the appropriate delay allows **(c)** coherent, constructive interference at the desired focal point.

then the emissions will line up at the focus, resulting in constructive interference and high amplitude [see Fig. 3.1].

However, in the case where c_0 varies in space, Eq. (3.2.2) is no longer valid. A straightforward correction computes the travel time over the ray from the element to the focal point

$$\tau_n = \int_{\ell_n} \frac{\mathrm{d}s}{c(\boldsymbol{r})}, \tag{3.2.3}$$

where $c(\boldsymbol{r})$ is the spatially-varying sound speed, and ℓ_n is the line segment between element n and the focus. Equation (3.2.3) is equivalent to finding an effective sound speed c_{eff} for each path, and computing the delay $\tau_n = r_n / c_{\text{eff},n}$. This technique however has two central deficiencies: the first is that diffraction is not considered. A changing medium will result in diffraction such that the path ℓ_n is no longer a line, and so the travel time must be computed, e.g., with ray theory.[80] The second is computational expense; the integral Eq. (3.2.3) must be evaluated for every focal target and every array element. While parallelizable, this operation is inherently intensive and thus a more efficient method is desirable.

Another approach posits that, rather than computing the traversal time over all paths from each element to the target focus (which ignores, e.g., multiple scattering) the delays might be measured. The process of time reversal[81,82] invokes acoustic reci-

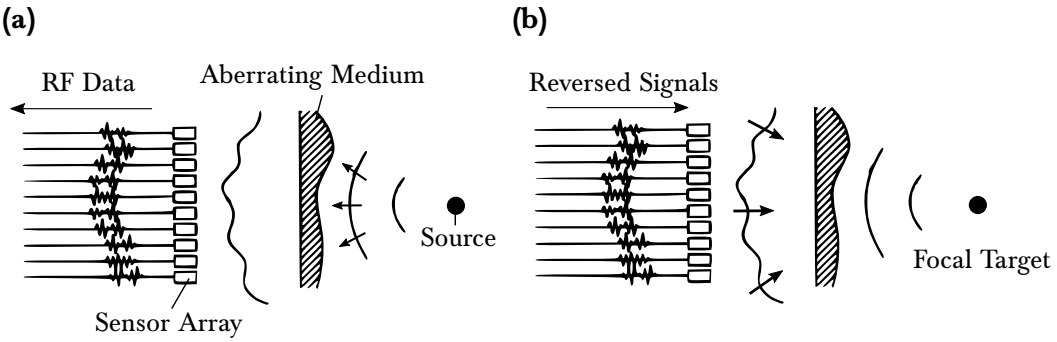

FIGURE 3.2: In time reversal, **(a)** signals due a point source are measured (or recovered from a full simulation). **(b)** Reversing these time series signals allows focusing at the original source location. Adapted from Fig. 5 of Ref. 81.

procity:[†] a consequence of which is that the measured field will be identical under exchange of the source and receiver. Thus, if the signals at the transmitter locations due to a point source at the target are known, they can then be reversed in time[‡] to achieve trans-skull focusing on transmit (see Fig. 3.2). Thus the problem of focusing in a complex medium may be addressed by determining the amplitude changes and phase delays at each element due to a point source at the target.

While robust and conceptually simple, determination of these time-domain signals is non-trivial in trans-skull contexts. These phase and amplitude modulations may be determined experimentally via measurement of the field due to an induced cavitation source at the target location inside the skull;[79,84–86] however, cavitation events in the brain are not always desirable, and the relatively high cavitation threshold requires additional corrections or high power arrays.[87] Use of corrections based on analysis of time domain signals measured from contrast agent microbubble emissions has been demonstrated,[88] though the location of these cavitation events cannot be controlled precisely. Alternatively, a point source can be placed within the skull to enable effective trans-skull therapy;[55,89–91] however this technique requires invasive placement at the target, which is not possible in realistic scenarios. For these reasons, several simulation techniques have been proposed for aberration correction, including finite difference time domain (FDTD)[60,92] and k-space propagation models.[7,62,93] In these methods,

[†]While a powerful fundamental result, acoustic reciprocity holds strictly only for linear, lossless propagation. While the former restriction is a reasonable approximation one for trans-skull applications, losses present a more relevant challenge[83] for this method and require more sophisticated time-reversal processes with amplitude correction.[55]

[‡]The term "conjugated" is sometimes used, since the complex conjugate of the frequency domain pressure is equivalent to reversing the time domain signal: $\mathcal{F}^{-1}[\tilde{p}^*] = p(\boldsymbol{r}, -t)$.

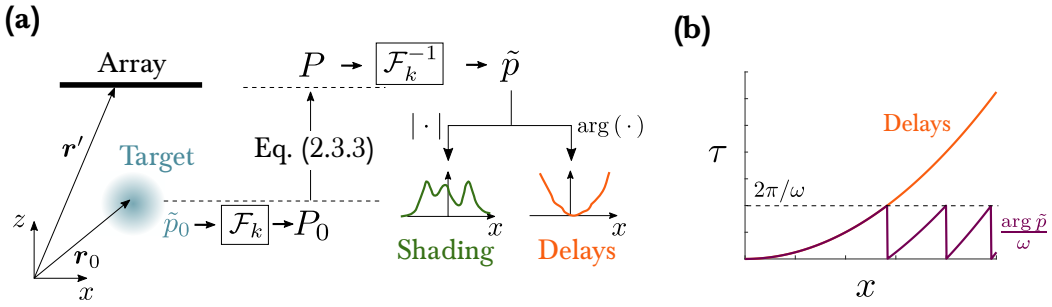

FIGURE 3.3: Illustrative calculation of focal delays. **(a)** Focal delays and amplitude shading are calculated from the magnitude and phase of the field projected from an initial point source at the target location. This field is calculated with the HASA algorithm Eq. (2.3.3). **(b)** While the phase of the computed distribution at the receiver is bounded by 2π [i.e., $e^{i(\phi+2\pi)} = e^{i\phi}$], these values must be distinguished for finite signals.

the simulation of the acoustic propagation due to a point source inside the brain is used to estimate the required phases for aberration correction. While these methods can be very precise, as they may account for a broad range of physical effects including, e.g., mode conversion, viscosity and nonlinearity, there exists a fundamental trade-off between their accuracy and required computational complexity.[94]

The ASA has been applied to this problem with step-wise *locally* homogeneous approximations.[62,95] While these methods offer improved efficiency to full simulation methods, current implementations require field transformations at each step,[95–97] whereas the heterogeneous ASA developed in Chap. 2 does not. Thus, it is next considered if the HASA may be applied to compute the requisite parameters for trans-skull focusing in a highly efficient manner.

3.2.2 Correcting Focal Aberration with HASA

The HASA allows the focal delays to be calculated as a function of space to enable focusing through heterogeneous media. Consider that a perfect focal point may be presented as a delta function at the target location $\boldsymbol{r}_0$

$$\tilde{p}_0 = \delta(\boldsymbol{r} - \boldsymbol{r}_0)\,. \tag{3.2.4}$$

If this spatial impulse is taken as the source condition, propagation of this field to the transducer location $\boldsymbol{r}'$ with Eq. (2.3.3) [or Eq. (2.4.2) in the case of a stratified medium] will yield the phase and amplitude of the distorted field. Then the appropriate shading

$|\tilde{p}(\boldsymbol{r}')|$ and crucially time delays

$$\tau = \frac{\arg\left\{ \mathcal{F}_k^{-1}\left[P(k_x, k_y, z')\right] \right\}}{\omega} \tag{3.2.5}$$

may be applied to each element to generate a focal spot through the complex medium; see Fig. 3.3(a). Strictly, Eq. (3.2.5) must be evaluated for each frequency in the transmitted signal's bandwidth, and the shifted sine waves superimposed. However in practice, the delay is calculated only for the center frequency ω_0. Thus, for a relatively narrow bandwidth (fractional bandwidth $\lesssim$0.1), the transmitted signal from a transducer at $\boldsymbol{r}'$ would be given by

$$s(\boldsymbol{r}', t) = w(t) \cdot \left|\tilde{p}(\boldsymbol{r}', \omega_0)\right| \cos \omega_0 [t - \tau(\boldsymbol{r}')], \tag{3.2.6}$$

where $\tau(\boldsymbol{r}')$ is given by Eq. (3.2.5), and $\tilde{p} = \mathcal{F}_k^{-1}[P]$. Here also, $w(t)$ is a window function, chosen to be a Tukey window [Eq. (2.6.3)] with width L chosen to be 40 cycles at ω_0, and cosine fraction $\xi = 0.1$.

Importantly, in the case of finite duration signals, the difference between the total phase and the wrapped (or principal phase $\operatorname{Arg} \tilde{p}$) must be made, as the time delays are not equivalent $\bmod 2\pi/\omega$

$$\arg \tilde{p} = \operatorname{Arg} \tilde{p} + 2\pi n\,; \tag{3.2.7}$$

see Fig. 3.3(b). Thus a simple phase unwrapping, whereby large jumps in the phase are replaced by successive additions of 2π is used. While in some applications noisy phase variations can make accurate unwrapping more challenging,[98] the focusing problem, which requires evaluation of Eq. (3.2.5) rather than experimental measurement, is fortunately not subject to measurement noise.

3.2.3 Simulations

Simulations of trans-skull focusing were performed in the open-source ultrasound simulation toolbox k-Wave[23] with linear compressional behavior considered. To create a realistic acoustic environment, the sound speed, density, and attenuation were defined from clinical CT data of a human skull using a semi-empirical relationship to relate the Hounsfield unit H (a normalized intensity value for the specific CT image) to the

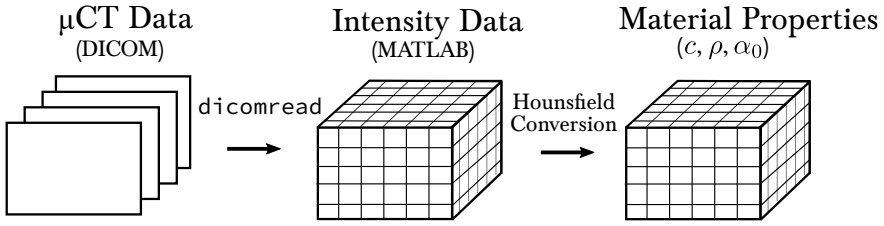

Figure 3.4: Data processing pipeline. The raw CT data files are read in from DICOM format to (single-precision) MATLAB values, which may then be interpolated to the desired grid spacing and assigned material properties, as with Eqs. (3.2.9) to (3.2.11)

density and speed of sound in the skull;[21] see Fig. 3.4 Defining the porosity

$$\Psi = 1 - H/1000\,, \tag{3.2.8}$$

the sound speed, density ρ_b, and attenuation of the skull were defined to be

$$c = \Psi c_w + (1 - \Psi)\, c_b \tag{3.2.9}$$

$$\rho = \Psi \rho_w + (1 - \Psi)\, \rho_b \tag{3.2.10}$$

$$\alpha = \alpha_{\min} + (\alpha_{\max} - \alpha_{\min})\Psi^{\gamma}\,, \tag{3.2.11}$$

where the b and w represent the maximum values of pure water and solid bone, respectively; these values were taken to be $c_b = 2500\,\mathrm{m/s}$ and $\rho_b = 2000\,\mathrm{kg/m^3}$. The implementation of k-Wave enables a spatially dependent attenuation coefficient α to model power law absorption, that is

$$\alpha = \alpha_0 \cdot f^{\beta} \tag{3.2.12}$$

where f is the frequency in megahertz. As the exponential dependence must be uniform for the entire grid, an average value of $\beta = 1.2$ was used.[99] A time step of 40 ns and spatial grid size of $\Delta x = \Delta y = 200\,\mu\mathrm{m}$ were used (CFL number 0.44) to ensure stability of the simulations.

Additionally, much as the sharp transitions in the measured spatial distribution $\tilde{p}_0$ due to the finite aperture may lead to the artificial introduction of very high spatial frequencies (Sec. 2.6), similar effects were observed for numerical delta functions (i.e., a binary source mask equal to unity only at the point of the target focus). Instead, a smoother cosine window (i.e., Tukey window with fractional width $L = 7$ grid points

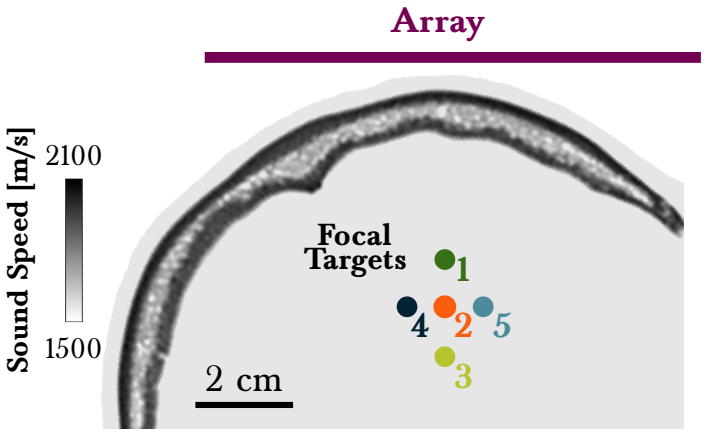

Figure 3.5: Geometry for trans-skull focusing simulations. Focal Targets were defined 40 mm to 60 mm from the array axially and ±15 mm transversely from the axis. Focal errors and amplitudes were then evaluated for each as a function of array aperture and frequency.

$\xi = 1$) was centered at the target location and this was used as the source condition.

3.3 Results

The results of the trans-skull simulation for various frequencies, with and without the correction are shown in Fig. 3.6, compared with the pure water case. The improvement offered with HASA–computed delays depends on the aperture, frequency, focal target, and array position. In the following sections, the effect of the correction of the focal accuracy, amplitude, and area are evaluated.

3.3.1 Focal Spot Accuracy

First, the effect of the phase correction on transmit focal accuracy for various focal targets as a function of frequency was evaluated (Fig. 3.7). For each of the five target focal positions shown in Fig. 3.5, the focal delays were computed geometrically with Eq. (3.2.2) and then with corrections given by Eqs. (2.3.3) and (3.2.5). Then, the position of peak pressure for the resulting field was compared with the target focal position, and the error defined as the Euclidean distance between the two. Aberration errors in focal targeting were generally larger at off-axis focal positions. Across all focal positions and frequencies, the focal error was reduced from 2.1 ± 1.2 mm without phase corrections to 1.3 ± 1.0 mm with the correction. The error was largest for low frequencies, but in this case it is still sub-wavelength (e.g., at 250 kHz, the wavelength

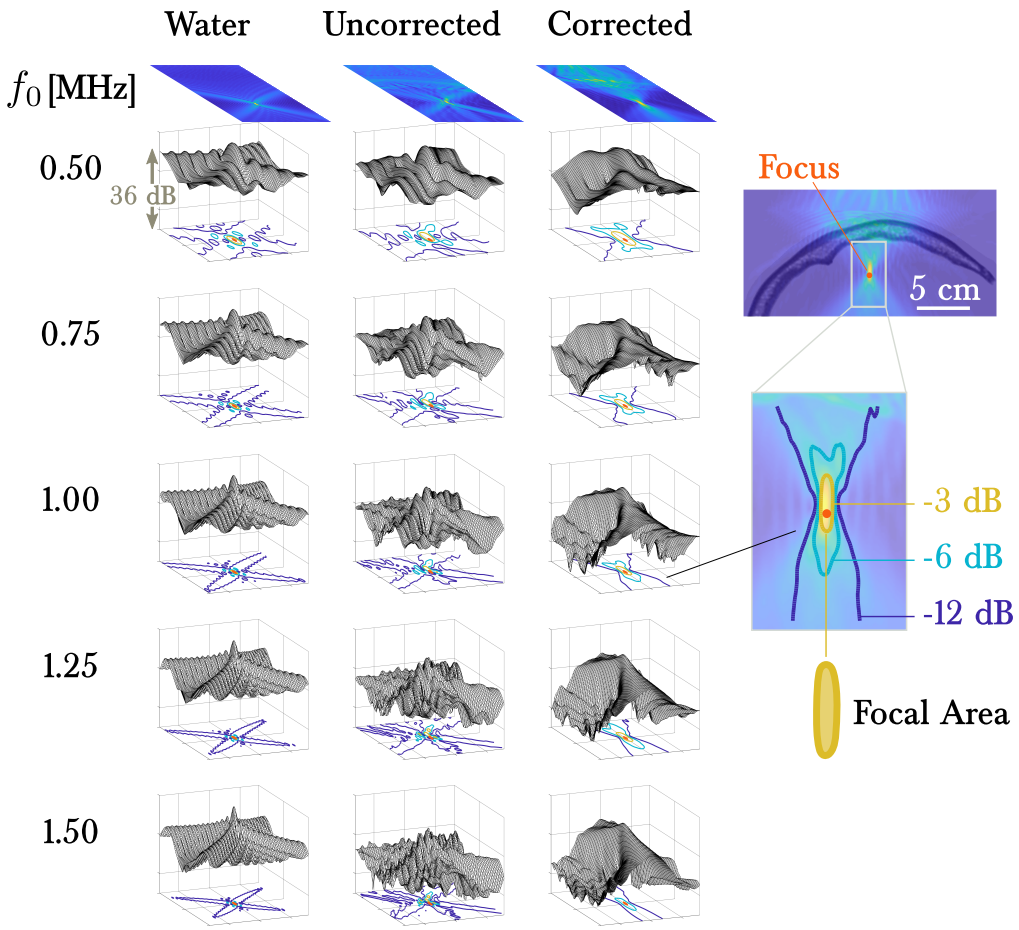

Figure 3.6: Simulated focal fields (i.e., peak pressure amplitude) from a 100 mm aperture array in water (left column), through the skull with geometric focusing (middle column) and with phase and amplitude corrections given by Eq. (3.2.5) for the indicated frequency.

in the brain is approximately 6.2 mm). Importantly, the corrected case had no outliers. See, for example Fig. 3.8, representing focusing with and without corrections for 1.25 MHz at position 4 in Fig. 3.5. The trans-skull field is severely aberrated in the uncorrected case, causing an uneven distribution with several high pressure regions. The highest pressure is well away from the target focus (blue circle), resulting in an uncorrected focal error was 5.1 mm [Fig. 3.8(a)]. In the corrected case [Fig. 3.8(b)], the focal field varies more uniformly and has error 0.6 mm. While the phase aberrations (and thus time delays) do not appear drastically different [Fig. 3.8(c), top], they are vital to ensure successful focusing. Additionally, the amplitude shading over the elements [Fig. 3.8(c), bottom] is important to ensure spatial uniformity of the field. While

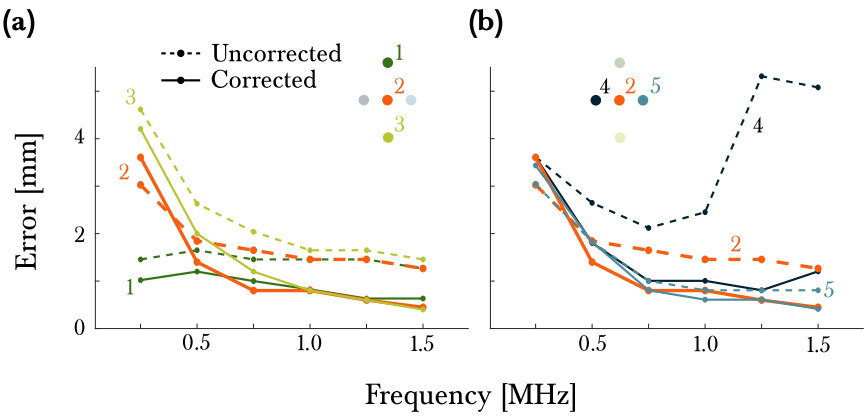

Figure 3.7: Effect of Frequency on Trans-skull Focusing Accuracy. For each focal target (as indicated and defined in Fig. 3.5), the focal error for various textbf(a) axial, and **(b)** transverse positions are shown for the uncorrected (dashed lines) and corrected cases (solid lines).

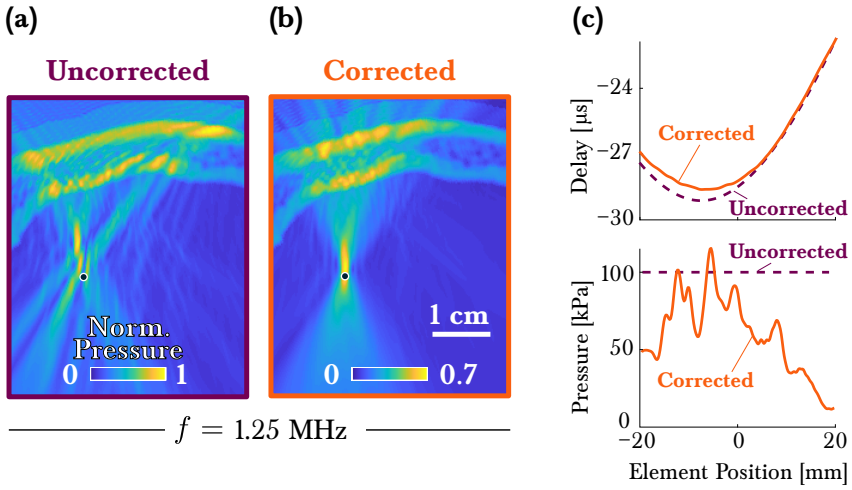

Figure 3.8: Focal Correction with the HASA. **(a)** Normalized pressure field for $f = 1.25\,\text{MHz}$ using geometric delays at position 4 in Fig. 3.5 with 50 mm aperture. **(b)** Normalized pressure field with corrected delays from Eq. (3.2.5) and amplitude shading. **(c)** Computed time delays and amplitude shading over the face of the array.

Table 3.1: Mean and standard deviation focal location error and spot size with uncorrected [Eq. (3.2.5)] and the corrected [Eq. (3.2.2)] focusing delays, averaged over all frequencies and positions shown in Fig. 3.5.

	Uncorrected		Corrected	
Aperture	**Error [mm]**	**Size [mm^2]**	**Error [mm]**	**Size [mm^2]**
50 mm	2.1 ± 1.2	6.8 ± 5.7	1.3 ± 1.0	12.6 ± 16.9
100 mm	2.2 ± 0.7	7.5 ± 6.4	1.0 ± 0.4	9.6 ± 10.9

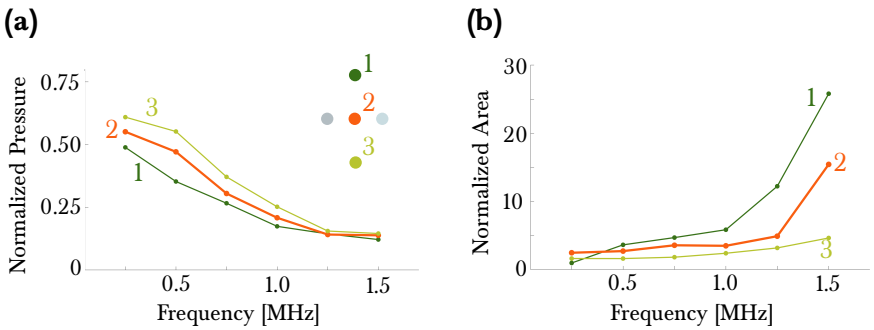

Figure 3.9: Focal spot characteristics for axial positions. **(a)** Normalized corrected focal pressure for the indicated focal target position (as shown at top right and in Fig. 3.5) as function of frequency, normalized to the no-skull case. **(b)** Normalized area of the focal region for the indicated focal target position, again normalized to the free-field case.

the phase delays ensure better coherence at the focus, it is possible that with uniform shading, side lobes or regions of spurious coherence could cause other pressure peaks. The shading used also means that the total energy emitted in the corrected case was less, such that the peak pressure amplitude was slightly lower in the corrected case. Collectively, these results indicate that the HASA enables improved focal targeting accuracy.

3.3.2 Focal Spot Characteristics

Next, the characteristics of the focal spot were evaluated, again as function of frequency, and compared to the case of geometrical focusing in water. In this way, the effect of the skull may be ascertained both in terms of insertion loss and aberration Figure 3.9 displays the focal amplitude and spot size for the three axial focal spots (labeled 1–3 in Fig. 3.5). At lower frequencies, the focal amplitude is comparable to the water case (peak pressures above 50 % of the no-skull case, and with focal spot size quite similar. However, at higher frequencies, losses due to absorption become larger (recall this was modeled as $\alpha \propto f^{1.4}$) such that the peak pressure is approximately 10 % of the water case [Fig. 3.9(a)]. The absolute size of the focal spot in the corrected case also decreased (e.g., from $22.9 \pm 13.8\,\mathrm{mm}^2$ at 250 kHz to $6.5 \pm 3.7\,\mathrm{mm}^2$ at 1.5 MHz for the 100 mm aperture); however, this decrease with frequency was slower than in the homogeneous medium case, and thus the size of the focal spot *relative to the homogeneous case* did increase [Fig. 3.9(b)]. In the case for the focal depth was constant and only the transverse location of the focus, the trends were quite similar, though the focal area increase was less dramatic; see Fig. 3.10

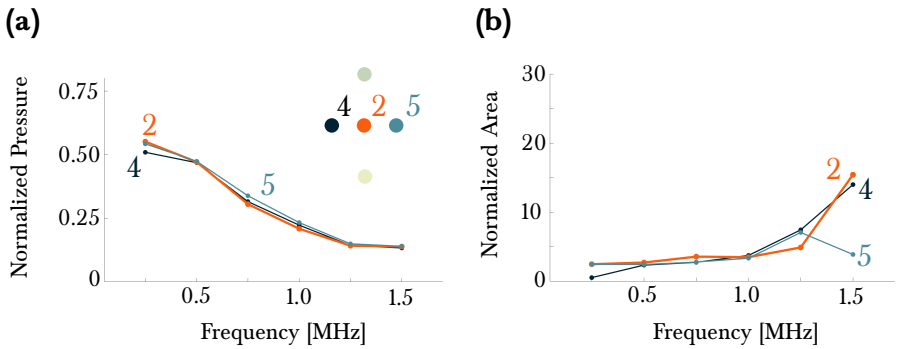

Figure 3.10: Focal spot characteristics for transverse positions. **(a)** Normalized corrected focal pressure for the indicated focal target positions 2, 4, and 5 (as shown at top right and in Fig. 3.5) as function of frequency. Amplitudes are normalized to the water only (i.e., no skull) case. **(b)** Normalized area of the focal region for the indicated focal target position, again normalized to the free-field case.

3.3.3 Influence of Array Standoff

To assess the impact of the standoff distance of the array form the skull on focusing, the focal accuracy was determined for various stand-off distances d (i.e., the distance from the skull to the array) for different apertures and targets [Fig. 3.11(a)]. The targets were maintained at an axial distance of $z = 40\,\mathrm{mm}$. Results indicate that the focal accuracy and improvement were comparable for different standoff distances ($0.6 \pm 0.3\,\mathrm{mm}$ with the correction and $1.6 \pm 1.3\,\mathrm{mm}$ without. The focal error did not have a strong trend with d, as changing the position of the skull represents a somewhat arbitrary change in the heterogeneity $c(\boldsymbol{r})$. Again the lack of outlier cases highlights the importance of the correction. Figure 3.11(c) shows that for the off-axis position with a small aperture, the error was nearly 7 mm without the correction, and 1.4 mm with the correction and 50 mm aperture. Thus the HASA correction is relatively robust to the array's position relative to the skull (though any trends are specific to the particular arrangement).

3.3.4 Computational Efficiency

Simulation of a point source in the computational domain over which the focusing simulations were performed required approximately 2 min—this is the time required for a time reversal implementation depicted in Fig. 3.2. The corrections computed with the HASA required just $166 \pm 37\,\mathrm{ms}$. The efficiency is further underscored in the three-dimensional case: full wave simulations require on the order of 1 s *per time step* for the most efficient pseudospectral methods,[100,101] such that simulating the field would

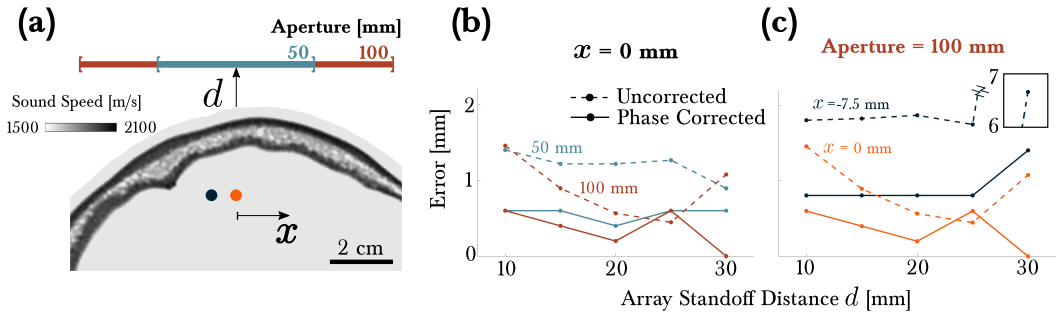

FIGURE 3.11: Effect of array standoff distance on trans-skull focusing. **(a)** Simulation geometry and target locations. **(b)** Error in focal maxima from $x = 0\,\mathrm{mm}$ as a function of standoff distance for the indicated aperture. **(b)** Error as a function of standoff distance for a 100 mm aperture at for the indicated focal target.

require tens of minutes or hours for a single point. While these simulations account for, e.g., nonlinearity, absorption, and multiple scattering, their clinical utility is currently more limited. Therefore the HASA-derived corrections offer an attractive means for efficient, adaptive trans-skull focusing.

3.4 Summary of Contributions

In this chapter, the efficacy of the heterogeneous angular spectrum approach developed in Chap. 2 was applied to the problem of trans-skull focusing. Via a simulation study, the focusing accuracy was improved by nearly 70 % over a range of frequencies and apertures. Calculation of the phase and amplitude corrections required on the order of hundreds of milliseconds with little optimization on nonspecialized hardware. Compared to time-reversal method, the required computation time was orders of magnitude smaller, and extends naturally to three dimensions. Together, these results suggest focal corrections with HASA have great potential for clinically relevant applications where variable focusing without computationally expensive full simulations.

Chapter 4
Aberration Correction in Passive Acoustic Mapping

4.1 Introduction

4.1.1 Trans-skull Imaging

While interest in using sound to probe the interior of the body was postulated[†] over 300 years ago,[102] it was the technological developments impelled by two world wars enabled the first ultrasonic imaging in the middle of the 20$^{\text{th}}$ century. Earliest 1D images were demonstrated in the 1940s,[103] and techniques were soon applied[104,105] for biomedical imaging.[‡] Significant advances in microprocessor technologies 1980s enable fabrication of phsed array imaging transducers.[1] These arrays enabled electronic steering of the focus, and thus 2D (B-mode) images, without mechanical scanning. In the intervening years, advances in transducer technology, signal processing techniques, and computational power have greatly improved the clarity, contrast, and temporal resolution of the acoustic images attainable at present.

Despite such progress, active imaging of the brain with ultrasound remains quite limited. The skull's density and stiffness, each roughly 50–100 % greater than that of soft tissue, cause a large impedance mismatch, and thus significant reflection of incident energy. This loss is compounded since the incident *and* reflected energy must be transmitted in an active imaging approach. Further complication is caused by absorption: at megahertz frequencies, the skull has a significant absorption coefficient, such that compensation for transmission loss via increased acoustic amplitudes induces significant heating that can be damaging. Passive cavitation imaging (i.e., use of passively recorded microbubble emissions excited by a separate therapy transducer)

[†]Robert Hooke's impressive foresight is highlighted in the summary of this work, p. xv. Though Hooke concedes in the following sentences that such capabilities may seem, at the time, "phantastick", he credits such fantastical thinking for great insight, perhaps equally as wisely.

[‡]Coincidentally, some of the earliest work in active ultrasound imaging of the body was in the brain.[106,107] However, the presence of the skull was problematic then too, and the results of early work has been attributed to "fortuitous artifacts."[108]

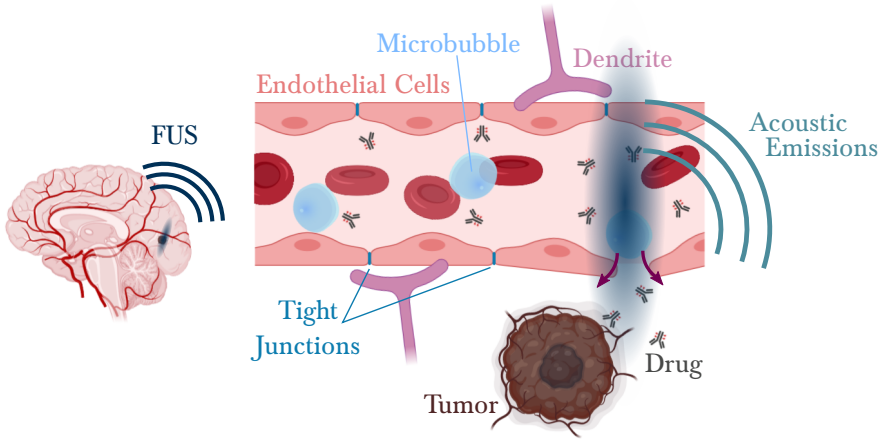

Figure 4.1: Targeted transcranial focused ultrasound excites the introduced microbubble contrast agents. The resulting mechanical forces exerted by the bubbles loosen the tight junctions between the endothelial cells and allows transport of drugs across the blood-brain barrier, while their acoustic emissions contain information about the level of excitations.

reduces these concerns by half, as the acoustic energy for imaging need only transit from within the brain to the sensor, with excitation provided by a separate therapeutic array.[109,110] Additionally, the exploitation of the signal coherence by the sensor array enables increased sensitivity to detect the relatively low-amplitude signals. However, previously described PAM techniques that can account for medium heterogeneity are computationally expensive and thus extension of such techniques can benefit significantly therapeutic monitoring.

4.1.2 Aberration in Passive Acoustic Mapping

Skull aberrations induce complications in the problem of of source localization, a priority in monitoring microbubble-enhanced ultrasound therapy. Recent work has demonstrated that such techniques make possible, e.g., transient disruption of the blood-brain barrier to enhance delivery and uptake of therapeutic agents;[57,111,112] see Fig. 4.1. The induced microbubbuble oscillations, termed acoustic cavitation, will in turn radiate spherical waves, and these echoes may be used to infer details about the nature of the activity.[25] Real-time monitoring of this activity usually relies upon passive cavitiation detection (PCD) whereby a single receiving element is used to record bubble emissions Imaging of this acoustic cavitation from the bubbles' emitted signals is termed passive acoustic mapping (PAM), and several techniques for guiding microbubble-enhanced FUS interventions have been presented to date.[113–115]

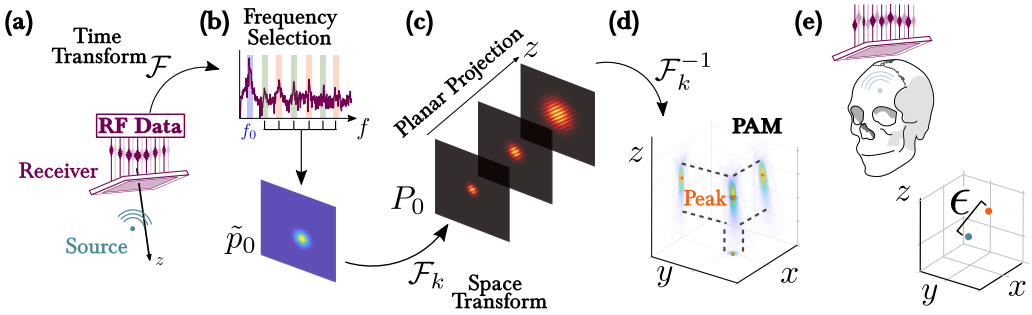

FIGURE 4.2: Uncorrected ASA results in aberration for complex media. **(a)** Acoustic emissions from a point source are recorded by a receiver array. **(b)** The RF data are then transformed in time to select the frequencies of interest. The spatial distribution of the field at this frequency at the receiver $\tilde{p}_0$ is obtained. **(c)** The field $\tilde{p}_0$ is transformed into the spatial frequency domain to give its angular spectrum P_0, which is projected through the volume with Eq. (2.2.6). **(d)** The inverse transform is performed to obtain the intensity field (i.e., PAM) throughout the region. **(e)** If the signal passes through the skull, aberration in the reconstruction leads to localization error ϵ.

Direct implementations do not account for medium heterogeneity,[25,116–119] though recent efforts have incorporated human skull aberration corrections into both frequency-domain[110,120] and time-domain[19–21,94,121] PAM implementations. However, to obtain the corrections, these methods require either invasive measurement[55,86] or point-by-point projections to all potential targets, and thus are either unrealistic or time consuming (up to several minutes) unless GPUs are used to speed up the computations.[94] The problem of computational speed is well addressed by the ASA method,[25] however its unmodified formulation with a constant speed of sound results in aberration for trans-skull applications; see Fig. 4.2.

Additionally, the spectral selectivity inherent to frequency domain methods is important for characterizing the type of oscillation.[25,119] Time domain methods[116–118] can incorporate filtering to extract certain frequency content, but they retain the entire series and generally incur high computational loads, again unless GPU units are used to speed up the computations.[118] Reconstructions on the order of milliseconds are also important for closed-loop control of the microbubble dynamics[115] and improved temporal resolution during microbubble imaging.[15,20] Thus there is a need for fast and frequency selective reconstructions to visualize the cerebrovascular microbubble dynamics through the skull, which will have important implications for image guided therapy and imaging.[122]

This chapter provides an overview of extant PAM techniques, and the trade-offs

represented by using the angular spectrum approach to this end. Then, the heterogeneous correction derived in Chap. 2 is applied to the problem of passive acoustic mapping in trans-skull applications. Finally, the first-order correction valid for stratified media is considered for biologically relevant scales and frequencies.

4.2 Passive Acoustic Mapping

In this chapter, the use of passive acoustic mapping for source localization in heterogeneous media using solutions derived in Chap. 2. As motivation for the use of the angular spectrum approach, the underpinnings of passive acoustic mapping of acoustic caviation [sometimes termed "passive cavitation imaging (PCI)"] are presented in this section. Note that the term "intensity" in the context of PAMs refers to the image intensity, rather than to the acoustic intensity. While these two should be approximately proportional, no transfer function (i.e., the conversion between the transducer's output voltage and the corresponding pressure in pascals) was attempted.[†] While quantitative PAM is possible with such considerations,[119] the present interest is in the spatial distribution and harmonic content of the signals, and thus the proportionality between the PAMs and the acoustic intensity field is not considered.

4.2.1 Time Domain

Conventional delay-and-sum beamforming sums the time-shifted signals $s_n(t)$ from each sensor n with delays associated the travel time position in the image. Specifically, the intensity map $I(\boldsymbol{r})$ is obtained from[113,116]

$$I(\boldsymbol{r}) = \int_0^T \left(\left| \sum_{n=1}^{N} \wp_n s(t - \tau_n) \right|^2 \right) \mathrm{d}t \tag{4.2.1}$$

where $\wp_n \equiv |\boldsymbol{r} - \boldsymbol{r}_n|$ is the distance from the pixel at $\boldsymbol{r}$ to the sensor at $\boldsymbol{r}_n$, and $\tau_n = \wp_n / c_0$ is the travel time between the pixel and sensor; see Fig. 4.3. The first term in the integrand of Eq. (4.2.1) represents the scale, shift, and sum operation. The principle in this calculation is that if the signals are shifted by delays given by their travel time from the true location, then they will sum coherently, thus giving a large intensity value at that location. Conversely, if delays associated with source-free regions are applied,

[†]While the knowledge of the physical field values (i.e., in pascals) is important for a full simulation, the acoustic field of interest for transcranial PAM is radiation due to cavitating microbubble contrast agents. The strength of these oscillations is well correlated with spectral content of the radiated signals, which may serve as a proxy for the acoustic intensity; see Sec. 4.2.4.

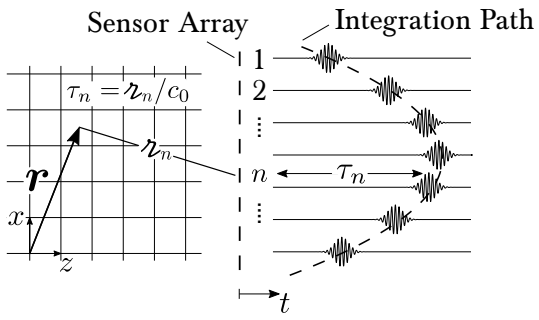

FIGURE 4.3: Delay-and-Sum Geometry. The delays τ_n are determined by the distance $\mathscr{r}_n$ from the pixel at $\boldsymbol{r}$ relative to the sensor n. This in effect defines a parabolic integration path in $\mathscr{r}$-t space (right, after Ref. 123) to compute that pixel's intensity.

the summation will be incoherent, and the intensity will be correspondingly smaller—exacerbated by the square operation. Alternatively, Eq. (4.2.1) can be understood as associating an integration path in $\mathscr{r}$–t space, as in Fig. 4.3. The scaling by $\mathscr{r}_n$ accounts for geometrical spreading between the source and receiver. In practice, the calculation is made such that incoherent background is removed

$$I(\boldsymbol{r}) = \int_0^T \left(\left| \sum_{n=1}^{N} \mathscr{r}_n s(t-\tau_n) \right|^2 - \sum_{n=1}^{N} \left| \mathscr{r}_n s(t-\tau_n) \right|^2 \right) \mathrm{d}t \,, \tag{4.2.2}$$

where the second term serves to subtract off the "DC" contribution.[123]

4.2.2 Frequency Domain

The Fourier transform has the convenient property that translation of a time domain signal imparts only a phase difference in its transform, since

$$\begin{aligned} \mathcal{F}\left[p(t-t_0)\right] &\equiv \int_{-\infty}^{\infty} p(t-t_0)\, e^{i\omega t}\, \mathrm{d}t \\ &\overset{t'=t-t_0}{\Longrightarrow} \int_{-\infty}^{\infty} p(t')\, e^{i\omega(t'+t_0)}\, \mathrm{d}t' = e^{i\omega t_0} \int_{-\infty}^{\infty} p(t')\, e^{i\omega t'}\, \mathrm{d}t' = e^{i\omega t_0} \tilde{p} \,. \end{aligned} \tag{4.2.3}$$

Thus the time delays in Eq. (4.2.1) [or Eq. (4.2.2)] may be replaced with phase delays $\phi_n = \omega\tau_n = \omega\mathscr{r}_n/c_0$ of the frequency domain signals $\tilde{s}_n(\omega)$. In this case, the recon-

structed intensity field is formed via[119,124,125]

$$I(\boldsymbol{r}) = \int_{\Omega} \left(\left| \sum_{n=1}^{N} \mathcal{r}_n \tilde{s}_n \, e^{i\omega\tau_n} \right|^2 \right) \mathrm{d}\omega \tag{4.2.4}$$

where Ω is the set of frequencies at which the map is to be formed. Equation (4.2.4) has two chief advantages over the time domain version Fig. 4.3 for the purposes of caviation monitoring. First is that the time shift (a convolution) has been replaced by a phase shift (multiplication), which is a less computationally demanding operation. As discussed in Chap. 2, while the transform must be computed, FFT algorithms are sufficiently efficient to mitigate this consideration. The second advantage is the inherent frequency selectivity offered by the choice of the integration frequency range Ω. Since acoustic emissions due to cavitation are relatively narrowband, the region of integration can be reduced substantially to the smaller bandwidths of interest, further reducing the computational burden.

4.2.3 Angular Spectrum Approach

The angular spectrum approach (ASA) employs one further Fourier transform of the data. Just as Eq. (4.2.4) replaced the temporal delays with phase shifts, these still must be computed for every pixel, due to the presence of $\mathcal{r}$. However, as shown in Chap. 2, the field may be computed throughout the region with use of Eq. (2.2.6). Let $S_0 = \mathcal{F}_k \left[\tilde{s} \right]$ so that

$$I(\boldsymbol{r}) = \int_{\Omega} \left(\left| \mathcal{F}_k^{-1} \left[S_0 \, e^{i\sqrt{\omega^2/c_0^2 - k_x^2} z} \right] \right|^2 \right) \mathrm{d}\omega \tag{4.2.5}$$

Note that there is no scaling by $\mathcal{r}_n$ in Eq. (4.2.5), as the propagation is described by plane waves which are not subject to geometric spreading. The efficiency is made plain in the argument of the transform in Eq. (4.2.5), as the calculation may be achieved via a single array multiplication. The order of computation times for the three methods is shown in Fig. 4.4, and highlights the importance of exploiting the ASA's efficiency: as the number of points becomes large—especially in the case of volumetric imaging—inherent efficiencies are essential to keep computation times tractable.

In the case of the heterogeneous ASA, the argument of the inverse transform in

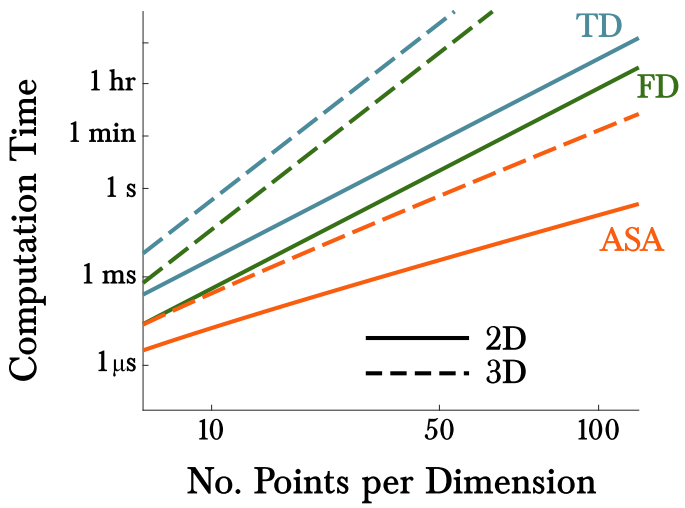

Figure 4.4: Approximate computation times for PAM with the time domain (TD), frequency domain (FD) and angular spectrum (ASA) methods. Example is for a 1000 point time series, 2.5 GHz processor, and 5 % bandwidths for the frequency domain methods.

Eq. (4.2.5) is replaced with either the analogous form of Eq. (2.3.3):

$$S^{n+1} \approx S^n e^{ik_z \Delta z} + \frac{e^{ik_z \Delta z}}{2ik_z} (S^n * \Lambda) \times \Delta z \tag{4.2.6}$$

[where $S^n = S(k_x, k_y, n\Delta z)$] in the general case, or

$$S(k_x, k_y, z) = S_0 \exp\left[i \left(\sqrt{\omega^2/c_0^2 - k_x^2} z + \phi \right) \right], \tag{4.2.7}$$

[where ϕ is the phase correction given by Eq. (2.5.6)] in the stratified case. Note that Eq. (4.2.6) precludes the use of a single matrix multiplication, since S must be calculated in each plane sequentially. Fortunately, an element-wise multiplication (i.e., Hadamard product) product may still be used for the analytical stratified case Eq. (4.2.7).

4.2.4 Effect of Bandwidth

As discussed in the previous sections, the benefit of the ASA for PAM is partially numerical (due to the recasting of the convolution as a multiplication to the efficiency of the FFT), but also due to the relatively narrow bandwidths of interest in PAM for therapeutic modeling. Microbubble oscillations have well-established[126–129] spectral characteristics depending on the nature of their oscillations. The classical Rayleigh-

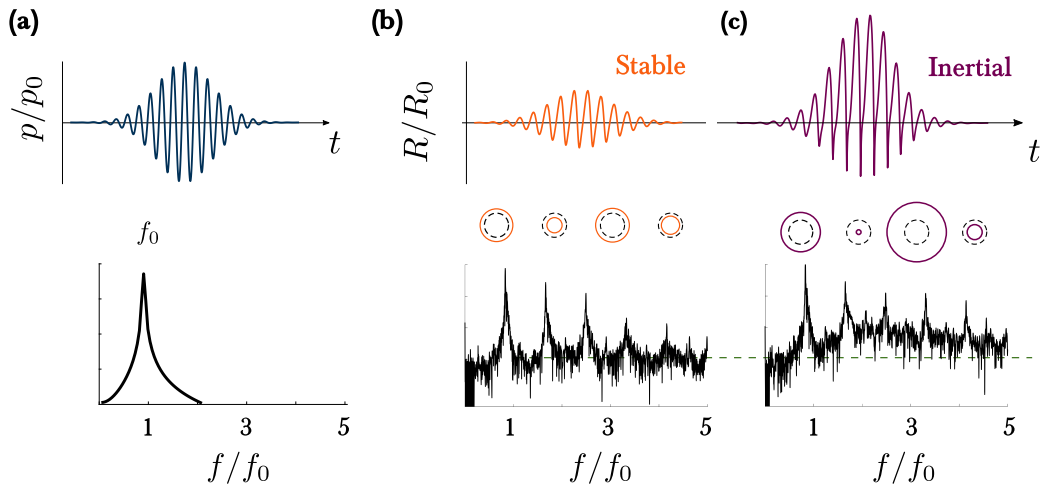

FIGURE 4.5: **(a)** Incident acoustic signal is a narrowband pulse (top) with center frequency f_0 (spectrum at bottom). **(b)** For smaller-amplitude excitations, the oscillations are stable about the equilibrium radius R_0, and harmonics and ultraharmonics are seen in the spectrum. **(c)** For stronger excitations, bubble collapse events occur, and there is a rise in the broadband baseline (green dashed line). Bubble radii computed from Ref. 126 with $|p| = 100$ and 500 kPa respectively, and spectra taken from experimental data.

Plesset equation governs the radius R of a free gas bubble in a liquid:[†]

$$\underbrace{\frac{p_{\text{bub}}(t) - p_\infty(t)}{\rho_0}}_{\text{Forcing}} = \underbrace{R\ddot{R} + \frac{3}{2}\left(\dot{R}\right)^2}_{\text{Nonlinear Oscillator}} + \underbrace{\frac{4\nu_{\text{liq}}\dot{R}}{R} + \frac{2\gamma}{\rho_L R}}_{\text{Damping}}, \tag{4.2.8}$$

where ν_{liq} is the kinematic viscosity of the liquid, and γ is the surface tension. That Eq. (4.2.8) has the form similar to that of a damped nonlinear oscillator is borne out by the observed dynamics. For a narrowband harmonic excitation with frequency f_0 [Fig. 4.5(a)], the resultant bubble oscillations (and thus pressure radiated into the fluid and received by the imaging array)[‡] will comprise largely harmonic ($f = nf_0$, where $n = 1, 2, \ldots$) and ultra-harmonic [$f = (n + 1/2)f_0$, where $n = 0, 1, 2, \ldots$] components; see Fig. 4.5(b). These relatively small-amplitude [$R(t)/R_0 \sim 1$] oscillations are termed "stable cavitation" and are the type that are most highly correlated with reversible

[†]This simplified model neglects losses due to radiation, thermal effects, and the presence and dynamics of an encapsulating shell. A more complete contemporary model is described in Ref. 126; see also Sec. 5.3.2.

[‡]Strictly, the pressure radiated by the oscillating bubble is not proportional to its radius R; rather $p_{\text{rad}} = (\rho_{\text{liq}}/r)\left(R\ddot{R} + 2R^2\right) + \mathcal{O}[(R/r)^{-4}]$, where r is the radial distance and ρ_{liq} is the liquid density.[130]

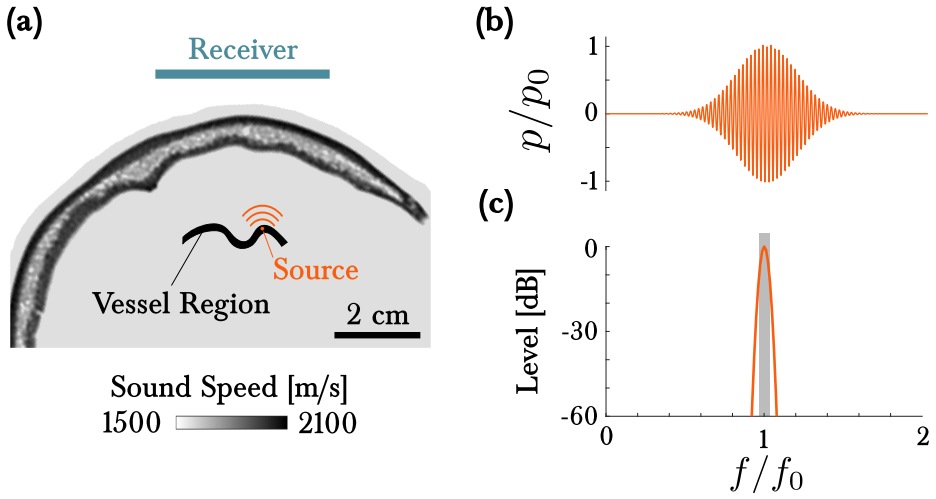

Figure 4.6: Geometry and source signal for trans-skull simulations. **(a)** Sound speed map used in simulation. **(b)** Normalized time series signal and **(c)** spectrum of the source pressure specified in the simulation. Gray box indicates bandwidth used for beamforming.

blood-brain barrier opening.[131–134] Larger amplitude oscillations due to stronger excitations lead to bubble collapse events, termed "inertial cavitation", and which are associated with more destructive phenomena such as tissue ablation.[113,135,136] These collapses give rise to radiation that is impulsive, and manifests as a rise in broadband emissions [Fig. 4.5(c); note the position of the dashed green line indicating a rise in the broadband baseline from (b)].

Thus, the frequency content corresponding to indications of stable cavitation represent a few narrow bands in the spectrum. Thus, the PAM reconstruction need be computed only for a limited number of frequency bins, such that these harmonic and ultraharmonic components are in Ω [in Eq. (4.2.5)]. Then, the number of operations may be reduce from $N_t/2$ (where N_t is the number of time samples, typically a few thousand) to several or tens. In the case of inertial cavitation, some care must be taken, since a narrow frequency range may not be an accurate representation of the baseline. In such cases a few regions can be chosen (e.g., offset quarter multiples of the excitation, between the ultraharmonics where no bubble signal is expected) to provide a reasonable capability to detect inertial cavitation.[115]

4.3 Methods

4.3.1 Simulations

Acoustic simulations were performed in k-Wave,[23] a pseudo- spectral time domain acoustic simulation toolbox for MATLAB. While the heterogeneous ASA is fully applicable to volumetric reconstructions (i.e., recovery of a three dimensional field from the measurement over a 2D virtual array, see Sec. 5.4.1.3), simulations in this chapter were performed in 2D to reduce the computational time required for the many simulations. The computational environment was the same as that used for the skull focusing simulations (Sec. 3.2.3), and its geometry is shown in Fig. 4.6(a).

Bubble emissions were approximated as Gaussian pulse sources, with center frequencies of 400 kHz, 800 kHz, 1.2 MHz and 5 % fractional bandwidth. These frequencies were chosen as to coincide with the frequency range of multiples (i.e., bubble harmonic frequencies) in the approximate range of the fundamental frequency modes of clinical transcranial FUS systems.[137]

Additionally, to determine the effectiveness of the stratified ASA correction for biomedically-relevant scales, a stratified medium which comprised a mean sound speed of 1540 m/s, augmented by a 25 % Gaussian profile with variance of 30 mm.[†] A mean density of 1043 kg/m^3 and attenuation of 0.54 dB/cm/MHz were defined for the entire medium[138] and 99 narrowband sources of 1 MHz were distributed uniformly in the medium as in Fig. 4.7(a). Finally, while the ASA is relatively robust to the addition of noise to the raw channel RF data,[25] uniformly weighted (i.e., white) noise, with amplitudes up to 5 times the peak value of the RF data were add prior to beamforming to investigate the performance of the phase correction in the presence of measurement noise.

4.3.2 PAMs and Source Localization

The reconstructed source location (x_r, z_r) was assumed to be the position of peak intensity of the PAM $I(x, z)$, as computed from Eq. (4.2.5) with Eq. (4.2.6) for the trans-skull case or Eq. (4.2.7) in the stratified case. The pseudo-code algorithm to the fully heterogeneous case is given by algorithm 1. The error was defined relative to the

[†]Use of the the stratified correction with the skull gave localizations that were actually worse than the uncorrected case. This result might be expected, as this situation violates three of the assumptions of its derivation (the medium is not stratified, the sound speed changes are not small, and the sound speed changes change abruptly over a wavelength). The latter is likely the most disruptive to the result, see Appendix A.3.2.

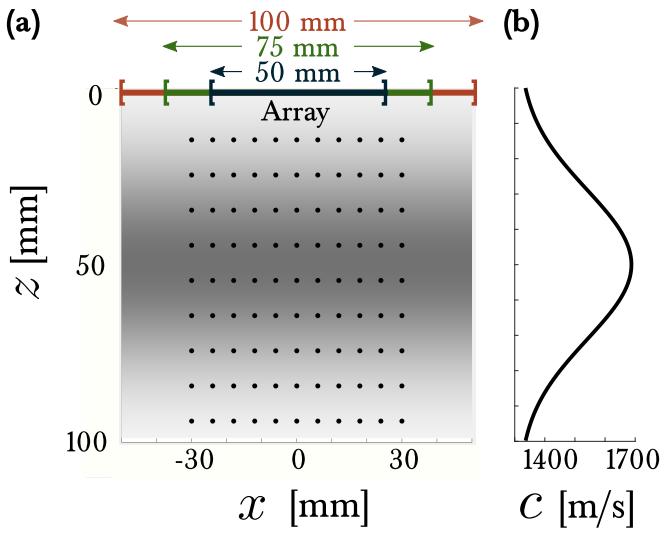

Figure 4.7: **(a)** Positions of sources in the stratified simulations. **(b)** Sound speed profile as a function of the axial distance z from the transducer array.

known source position from the simulation $(x_{\text{true}}, z_{\text{true}})$ as

$$\epsilon = \sqrt{\epsilon_x^2 + \epsilon_z^2} = \sqrt{(x_r - x_{\text{true}})^2 + (z_r - z_{\text{true}})^2}\,. \tag{4.3.1}$$

This straightforward approach works well in the case of a single source, but in the case of multiple sources of varying intensties, a more sophisticated approach would be required (see Sec. 5.2.1).

4.3.3 Experimental Validation

To demonstrate the feasibility of the proposed aberration correction method, *in vitro* experiments were performed. A custom 13-by-13 element matrix transducer array (Imasonic, Voray-sur-l'Ognon, France) was positioned in a 3D printed frame. The transducer was connected to a 256-channel research ultrasound system (Verasonics, Kirland, WA, USA) and controlled with a MATLAB interface. A right parietal segment of a human skull (Skulls Unlimited, Oklahoma City, OK, USA) approximately 10 cm-by-5 cm-by-0.5 cm was degassed overnight (approximately 12 hours) and affixed to the frame. The frame was then placed in a degassed water tank.

To determine the localization accuracy, a source with a known position relative to the transducer is required. An omnidirectional hydrophone (Reson Slangerup, Denmark) was connected to an arbitrary waveform generator (Keysight, Santa Rosa, CA,

input : Time series RF data $p(x,0,t)$, Sound Speed $c(\boldsymbol{r})$, Step Size Δz, Frequencies $\{f_n\}$
output: Intensity map $I(x,z)$

// Define auxiliary functions;
$c_0 = \text{avg}\, c(\boldsymbol{r})$;
$\mu = c_0^2/c^2(\boldsymbol{r})$;
$\lambda = (\omega/c_0)^2(1-\mu)$;
// Take temporal transform of RF data $(z=0)$;
$p(x,0,t) \rightarrow \tilde{p}(x,0,\omega)$;
// Initialize;
$I(x,z) = 0$;
for f_i *in* $\{f_n\}$ **do**
  // Take spatial transform at that frequency;
  $\tilde{p}(x,0,\omega_i) \rightarrow P(k_x,0,\omega_i) = P_0$;
  // Propagate to depths;
  for $j = 1; j <= N; j++$ **do**
    // Compute convolution in spatial domain;
    $\left(P^{j-1} * \Lambda\right) = \mathcal{F}_k\{\mathcal{F}_k^{-1}[P^{j-1}] \cdot \lambda(x, j\Delta z)\}$;
    // Step forward by Δz;
    $P(x, j\Delta z, \omega_i) = P^j = P^{j-1} e^{ik_z \Delta z} + \frac{e^{ik_z \Delta z}}{2ik_z}\left(P^{j-1} * \Lambda\right) \times \Delta z$;
  end
  // Take inverse and add in contribution;
  $\tilde{p}(x,z,\omega_i) = \mathcal{F}_k^{-1}\left[P_0 e^{ik_z \Delta z}\right]$;
  $I(x,z) \mathrel{+}= \|\tilde{p}(x,z,\omega_i)\|^2$
end

Algorithm 1: Algorithm for computation of PAMs from time series RF data.

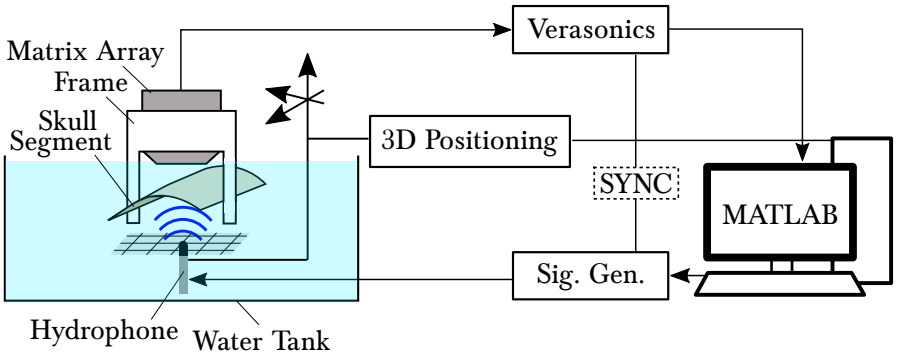

Figure 4.8: Experimental setup for the 3D PAM experiments. A hydrophone was used as a proxy for cavitation source, and scanned through a grid of known positions. Acoustic emissions were recorded through the skull by the matrix array transducer.

USA), and a 40-cycle windowed sine pulse was applied at the hydrophone's center frequency 1 MHz. A transmitted frequency above the matrix array's center frequency (but within its 50 % bandwidth) was chosen as the HASA correction is more valid for higher frequencies; see Appendix A and B.1. Passive recording of the acoustic signal by the the matrix array was synchronized through an output trigger of the waveform generator. The position of the hydrophone was controlled with a three-axis positioning system (Velmex, Bloomfield, NY, USA). The experimental setup is illustrated in Fig. 4.8. As the array pitch (1.8 mm) was larger than the acoustic wavelength (1.5 mm), the data were interpolated by a factor of 6.[†]

4.3.3.1 Registration

To implement the corrections calculated with the HASA, knowledge of the sound speed field relative to the transducer is required. The material properties were extracted from a micro-CT scan in the same manner as for the simulations [i.e., with Eq. (3.2.9)]. Three removable fiducial markers were placed in shallow (several millimeters) holes drilled into the skull surface for the micro-CT scan. Once in the frame, a plane wave volumetric image of the skull segment with the markers was acquired (21 angles in 1 degree increments about the x and y-axes, 42 angles total). The sound speed data, obtained from the CT image as described in Sec. 3.2.3, and ultrasound image, obtained from the plane wave acquisition, were then registered using these markers to obtain the appropriate geometry for the evaluation of the HASA PAM calculation. Once the acoustic image was obtained, the markers were removed from the skull for the trans-skull imaging experiments.

4.3.3.2 Evaluation Metrics

To assess the improvement afforded by the HASA for passive localization accuracy, two metrics were defined. First was the accuracy of the individual peak positions in the PAM relative to the true source position (i.e., the localization error). However, due to the sequencing of the Verasonics hardware and 3D positioning software, individual passively-recorded time series were not associated one-to-one with individual source positions; instead they could be compared to the entire set of all known source

[†]Note that this operation does not inject information into the measured data, but instead enables a finer computational grid available from the CT data. The discretization requirement Eq. (2.6.1) requires sampling twice per wavelength in the x- and y-directions. Since the received signal is due to a source approximately normal to the array, the principal wavenumber component will be in the z direction. Thus $k_x \sim k_y \sim 0$, and the sampling requirement is met for $F\#$ on the order of 1.

positions. Thus rather than the true error, instead the lower bound on the error was established. That is, if the reconstructed peak is at $\boldsymbol{r}_r$, the N true hydrophone positions were at $\{\boldsymbol{r}_i\}$ then the lower bound on the error was

$$\epsilon_{\min} = \min_N \left| \boldsymbol{r}_r - \{\boldsymbol{r}_i\} \right| \tag{4.3.2}$$

Since proximity to any of the source positions is sought by the lower bound metric, these errors will be significantly lower than the true source localization error. However, these values averaged over all sources will represent the relative accuracy of the localized points.

The second metric was an image correlation with a ground truth reference. First the reference image was created by superimposing uniform amplitude 2D Gaussian distributions with size approximately equal to the system point spread function[†] at each source location. Then a composite image is formed in the same manner from the peak locations in each PAM, by superimposing Guassians, but with each Gaussian amplitude equal to the amplitude of the PAM at the detected peak location. The product of these two images was then computed, and the image correlation was defined as the sum total intensity of all pixels over the product image, normalized by the total intensity of the composite image; i.e.,

$$\text{Correlation} \equiv \frac{\Sigma_\Omega I(\boldsymbol{r}) \circ I_{\text{ref}}(\boldsymbol{r})}{\Sigma_\Omega I(\boldsymbol{r})}, \tag{4.3.3}$$

where $\circ$ represents the Hadamard (element-wise) product, and Ω is the entire image domain. The correlation value is a measure of how well the peaks match with what would be expected for a perfect reconstruction.

[†]See also Sec. 5.1.

4.4 Results

4.4.1 Effect of Frequency on Localization

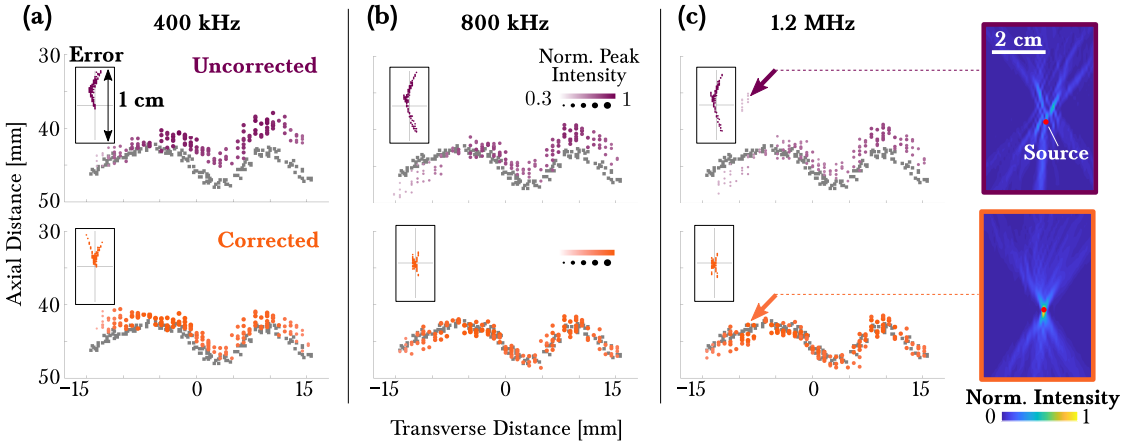

Figure 4.9: Frequency dependence of source localization accuracy for trans-skull PAM. Comparison of source localizations and associated errors (insets) for the uncorrected (top, purple) and corrected (bottom, orange), for **(a)** 400 kHz, **(b)** 800 kHz, and **(c)** 1.2 MHz sources beamformed with a 50 mm aperture. The size and transparency of the makrers indicates the relative amplitude of the PAM peak at that location. At far right in (c) are representative corrective and uncorrected maps for the indicated source localizations.

Figure 4.9 demonstrates the improvement in localization accuracy and signal strength when the corrected version Eq. (2.3.3) of the ASA is used compared with the uncorrected case Eq. (2.2.6). Qualitatively, the corrected source locations recovered from the corrected PAMs (orange) appear much closer to the true source positions (gray) than do the uncorrected localizations (purple). Without the correction the mean localization error was 2.3 ± 1.4 mm over all frequencies, while in the corrected case it was reduced to 0.9 ± 0.6 mm. The intensity of the peaks in the PAMs (indicated by the size and transparency of the markers) was also seen to be approximately 35 % higher in the corrected case. Crucially, the localizations in the corrected case presented no outliers—note the PAMs shown in Fig. 4.9(c), for which the uncorrected case results in centimeter-scale error, while in the corrected case the error is sub-wavelength.

The insets of each of Fig. 4.9(a–c) show the distribution of the localization errors relative to true positions [i.e., an marker at (0, 0) of the inset indicates perfect localization of that source]. While a slight error bias toward the transducer was seen at the lowest frequency of 400 kHz (likely due to the smaller relative aperture;[139] see

Fig. 4.10), the distribution of errors in the corrected case showed no bias and small magnitude in the 800 kHz and 1.2 MHz. That the improvement was most pronounced at higher frequencies is unsurprising, since the slowly-varying medium assumption $|\nabla c|/c \ll \lambda$ is more valid at these frequencies.

4.4.2 Effect of Aperture on Localization

To determine the effect of the receiver aperture on localization error, the source frequency was fixed at 400 kHz, and the aperture was increased from 50 mm up to 100 mm, while keeping the element spacing constant ($\Delta x = 200\,\mu\text{m}$).[†] Figure 4.10 indicates that a wider aperture enables improved accuracy. While some error was seen at 400 kHz for the corrected case [Fig. 4.9(a) and Fig. 4.10(a)], a wider aperture [such that the kd becomes similar to the 800 kHz case of Fig. 4.9(b)] reduces this error comparably; see Fig. 4.9(c).

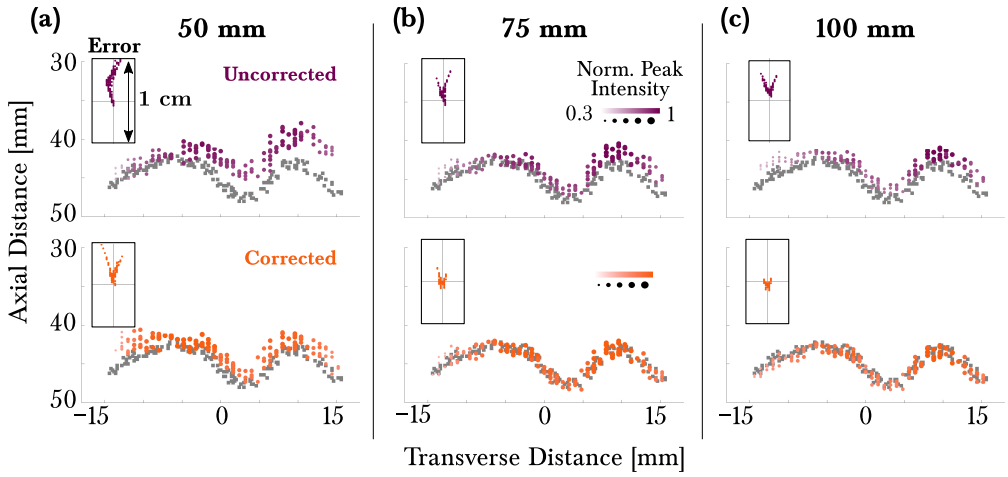

Figure 4.10: Frequency dependence of source localization accuracy for trans-skull PAM. Comparison of source localizations and associated errors (insets) for the uncorrected (top, purple) and corrected (bottom, orange), for 400 kHz sources beamformed with **(a)** 50 mm, **(b)** 75 mm, and **(c)** 100 mm apertures. As in Fig. 4.9, the size and transparency of the markers indicates the relative amplitude of the PAM peak at that location.

Finally, to determine the localization error over a larger field of view of the transducer, a grid of sources were positioned as shown in Fig. 4.11. These sources were taken to have center frequency 1 MHz and beamfored with and without the correction as before. Figure 4.11(b–c) demonstrate that, especially for larger apertures and along

[†]While a constant pitch increases the number of elements for the larger apertures, the improvement in localization is mostly due to the larger spatial sampling of the field.

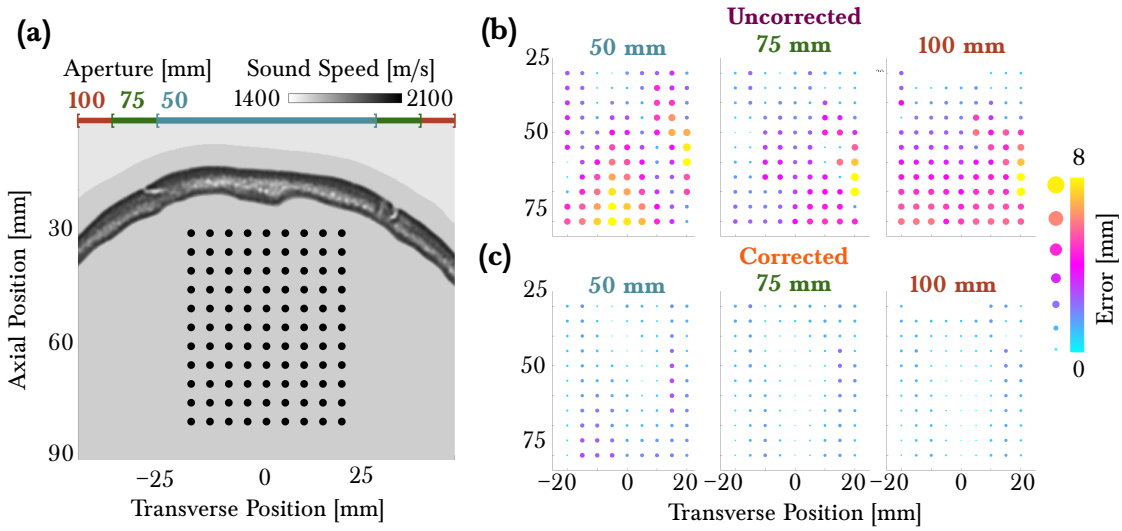

Figure 4.11: Effect of source position on source localization accuracy for trans-skull PAM. **(a)** Position of 1 MHz sources with respect to the array position and medium properties. **(b)** Localization accuracy for the indicated aperture size for each source in (a) for the uncorrected case. **(c)** Localization accuracy for the indicated aperture size for each source in (a) for the corrected case.

the array axis, the reduction of localization accuracy is substantial. Importantly, there are no outlying localizations with nearly centimeter scale errors as in Fig. 4.11(b). Table 4.1 summarizes the mean errors and peak intensities for the localizations in Fig. 4.11.

4.4.3 Stratified Results

The stratified medium solution derived in Chap. 2 is more restrictive than the general HASA as it requires not only that the change in sound speed occur over scales that are long compared with the wavelength, but also that this gradualness is significantly

Table 4.1: Mean and standard deviation PAM localizaion error and peak intensities with uncorrected [Eq. (4.2.5)] and the corrected [Eq. (4.2.6)] beamforming, computed over the positions shown in Fig. 4.11.

	Uncorrected		Corrected	
Aperture	**Error [mm]**	**Intensity**	**Error [mm]**	**Intensity**
50 mm	3.7 ± 2.2	0.73 ± 0.46	1.2 ± 0.7	1.0 ± 0.60
75 mm	2.5 ± 1.7	0.66 ± 0.36	0.9 ± 0.5	1.0 ± 0.47
100 mm	3.5 ± 1.9	0.62 ± 0.28	0.8 ± 0.4	1.0 ± 0.39

greater than the magnitude of the sound speed change (see Appendix A.3.2). As the sound speed changes in the skull compared to water and tissue are relatively large (60 %) *and* that the changes are abrupt meant that the source localization for the trans-skull simulations was not improved.

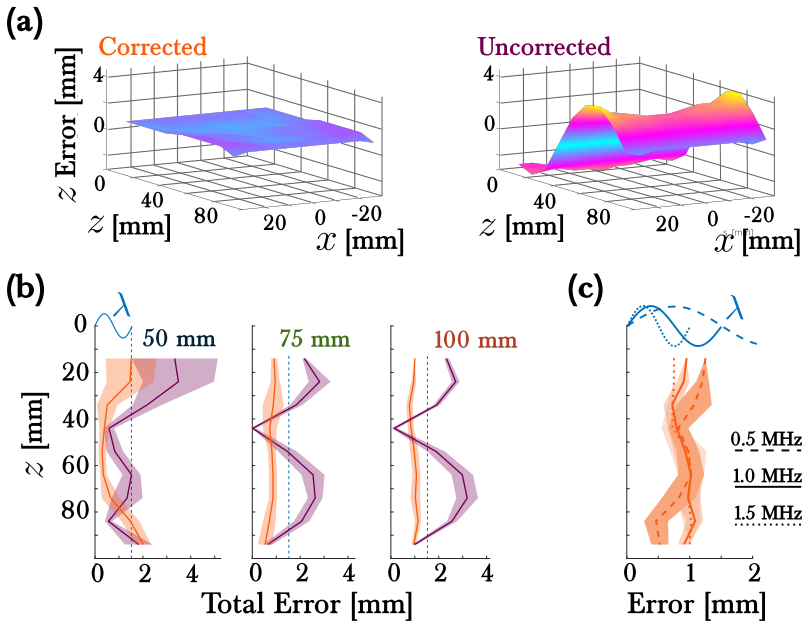

Figure 4.12: **(a)** Axial localization errors for the corrected (left) uncorrected (right) beamforming, for the source positions shown in Fig. 4.7(a). **(b)** Mean total error as a function of depth (averaged over all lateral positions) for the indicated aperture for the corrected (orange) and uncorrected (purple) cases. **(c)** Mean total error as a function of depth (averaged over all lateral positions) for 100 mm aperture for the corrected case with the indicated source frequency.

However, its utility at scales of relevance to other parts of the body was investigated with the test case shown in Fig. 4.7. Figure 4.12 demonstrates the improvement in source localization due to the phase correction for 1 MHz sources. Without the phase correction, the error was 2.05 ± 1.00 mm, while with the phase correction it was 0.97 ± 0.20 mm. The error in both the corrected and uncorrected case was principally in the vertical (axial) direction ($|\epsilon_{z,\text{avg}}/\epsilon_{x,\text{avg}}| = 34.6$ and 35.6 for the corrected and uncorrected cases, respectively) and is plotted in Fig. 4.12(b). To understand the effect of the beamforming aperture, the data were beamformed and the soruces were localized using three different aperture sizes. For the 50 mm aperture, some localizations in the corrected case have larger errors, however for larger apertures (75 mm and

Table 4.2: Mean and standard deviation PAM localizaion error and peak intensities with uncorrected [Eq. (4.2.5)] and the corrected [Eq. (4.2.7)] beamforming, computed over the positions shown in Fig. 4.7(a).

	Uncorrected		Corrected	
Aperture	**Error [mm]**	**Intensity**	**Error [mm]**	**Intensity**
50 mm	1.7 ± 1.3	1.0 ± 1.3	0.96 ± 0.81	1.0 ± 1.3
75 mm	1.9 ± 0.94	1.0 ± 1.0	0.81 ± 0.27	1.0 ± 1.0
100 mm	2.1 ± 1.0	1.0 ± 0.84	1.0 ± 0.2	1.0 ± 0.85

100 mm) which cover the horizontal extent of the sources, the corrected localization accuracy was within approximately one half wavelength [Fig. 4.12(b), orange]. In the uncorrected case, (purple) the error was largest for depths near 25 mm and 75 mm. These are the extrema of $\mathrm{d}c/\mathrm{d}z$, and thus where discounting the medium variation is most egregious. The mean effect of aperture on the localization error and peak intensity is summarized in Table 4.2. Interestingly, unlike in the trans-skull case, the peak amplitudes were quite similar with and without the correction, perhaps because the medium imparts a more systematic phase aberration. Thus without correction, the coherence is still high, just corresponding to the incorrect spatial location.

Finally, the absolute localization accuracy did not depend strongly on the wavelength [Fig. 4.12(c)]. The absolute localization error was similar for all frequencies (mean 0.91 mm, 0.97 mm, and 0.88 mm for 0.5 MHz, 1.0 MHz, and 1.5 MHz, respectively), as was the improvement relative to the uncorrected case at that frequency (mean improvement 55 %, 57 %, and 53 %). The short wavelength criterion was roughly met in all cases; for the longest wavelength (500 kHz), $|\mathrm{d}^2A/\mathrm{d}z^2| \sim 0.4$.

Thus the stratified medium correction, while no applicable to the specific problem of trans-skull imaging, does improve the accuracy of source localization at biologically relevant scales and frequencies.

4.4.3.1 Effect of Noise

While all simulations presented heretofore assumed ideal measurement, any realistic application of these techniques will be subject to measurement noise. To demonstrate the robustness of both the homogeneous and stratified ASA solutions to noise, the RF data from the simulations whose results are reported in Fig. 4.12 (100 mm aperture, 1 MHz sources) were beamformed after the addition of uniform white noise with amplitude 1 to 5 times that of the maximum value of the recorded RF data. The resulting PAMs show clear peaks with comparable error to the noiseless case

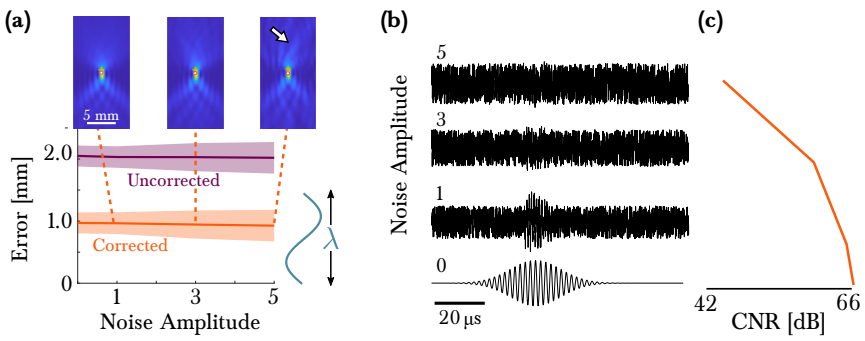

FIGURE 4.13: Effect of noise on localization accuracy at the biomedical scale (Fig. 4.12, 1 MHz sources, 100 mm aperture). **(a)** Mean localization error as a function of the added noise level for the uncorrected (purple) and corrected (orange) ASA. **(b)** Center channel waveforms from the simulation after addition of the indicated amount of noise.

[Fig. 4.13(a)] despite apparent total corruption of the time series data [Fig. 4.13(b)]. Averaged over the entire grid [Fig. 4.7(a)], the error without noise was 0.97 ± 0.20 mm and 2.00 ± 0.97 mm in the corrected and uncorrected cases, respectively. At the noise level of 5, the average errors were 0.93 ± 0.25 mm with the correction and 2.0 ± 1.0 mm uncorrected. The noise manifests in the PAMs as irregular interference patterns [arrow in Fig. 4.13(a)], which can cause aberrant high intensities and thus spurious localizations at still larger noise values. While the CNR of the images was reduced from 66.1 dB in the noiseless case to 43.2 dB when the added noise had amplitude up to 5 times that of the mean signal level, it remained at tens of decibels over all cases. However, Fig. 4.13 confirms that both the conventional and stratified medium ASA techniques are suitable for noisy conditions.

4.4.4 Experimental Results

Figure 4.14 shows the results from the ASA and HASA for trans-skull PAM localizations. When there was no skull between the source and receiver, the ASA recovers the shape and position of the source (i.e., the emitting hydrophone) as expected [Fig. 4.14(a)]. However, when the skull was introduced, the intensity of the image was reduced significantly (approximately 30 dB). Additionally, when no correction was used, noticeable aberration is present in the reconstructed image. The image in Fig. 4.14 indicates that while there is still evident coherence in the PAMs (note that the extracted peaks retain the "T" shape traced by the source), the localizations are shifted by approximately 1 mm in the horizontal direction.

Use of the ASA correction improves both degradations: first, the PAM intensity is

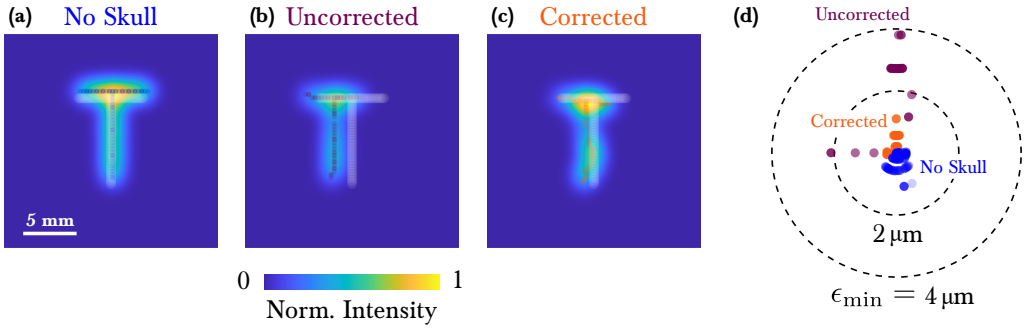

Figure 4.14: Composite images from peak localizations from 3D PAM experiments. Localized points (colored dots) compared with the truth positions of the source (white dots). **(a)** Reconstructed map without the skull segment. **(b)** Map with the skull and without corrections applied. **(c)** Corrected trans-skull map with. Scale is the same (b) and (c), which are 30 dB below (a). **(d)** Distribution of lower bound errors for the corrected, uncorrected, and no-skull cases.

larger by a factor of about 2.09 relative to the uncorrected case. Additionally the mean lower bound error[†] was reduced over all cases: without the HASA corrections, this bound was $1.3 \pm 1.3\,\mu m$, while with the corrections it was $0.2 \pm 0.3\,\mu m$, very close to the result for the no skull case ($0.2 \pm 0.2\,\mu m$). As seen in Fig. 4.14(d), the skull introduced a somewhat systematic error in the uncorrected case (purple), which was ameliorated with the ASA correction (orange). Thus the HASA provide a viable means of correcting aberration in volumetric trans-skull imaging.

4.4.4.1 Influence of Registration Parameters

Given the relatively low imaging frequency of the matrix array (820 kHz, wavelength 1.8 mm), the resolution of the resulting volumetric image was significantly degraded from that of the CT image (voxel size 0.1 mm). Thus while fiducial markers were used to ensure the position and orientation of the surface were approximately correct [Fig. 4.15(a)], optimizing the alignment proved somewhat delicate. Figure 4.15(b–c) demonstrates the effect of changes in the skull registration values on the correlation metric obtained with the image formed when the registration was altered slightly. Note that the micro-CT data and volumetric ultrasound image were interpolated to

[†]While all true source positions were known, due to collection constraints, individual PAMs could not be assigned to individual truth positions (i.e., the RF data acquisitions were unindexed). Thus for each localization, its distance to the *nearest* of all source positions was recorded to establish a lower bound on the localization accuracy. That is, the mean lower bound error is the mean distance between the colored dots and the white dots in Fig. 4.14.

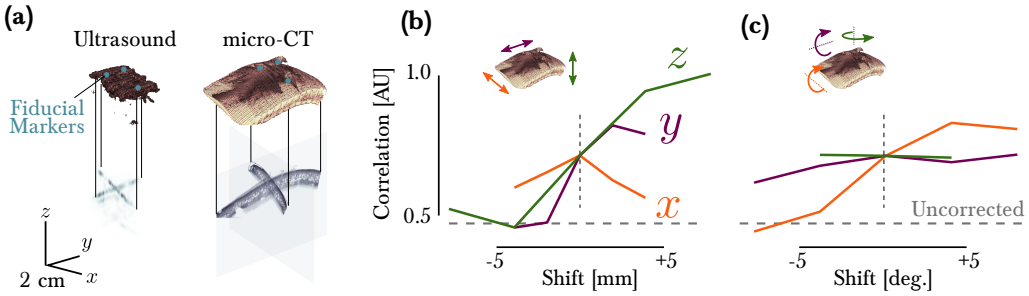

Figure 4.15: Effect of skull registration **(a)** Registered acoustic (left) and micro-CT (right) images of the skull segment used for the trans-skull experiment with representative cross sections. **(b)** Variation of the image correlation metric when the registered data was shifted in each dimension. **(c)** Variation of the image correlation metric when the registered data was rotated about each dimension. Dashed gray line indicates the correlation metric for the uncorrected map.

the same voxel size (200 µm), such that the registration did not require scaling. Thus, there were six degrees of freedom: rotation and translation along x, y, and z. For instance, in Fig. 4.15(b) it is seen that the correlation is most sensitive to the shift in the z-direction; if the registered skull position were taken to be 6 mm closer to the array (with all else equal), then the resulting image correlation would be not much better than the uncorrected case. Performing the correction with the sound speed field shifted 6 mm in the opposite direction increases the correlation, however the mean error lower bound rises to 5.3 ± 4.9 µm compared to the baseline case. The correlation was seen to be less sensitive to rotation [Fig. 4.15(c)], with the most dramatic effects seen for changes in θ_x (i.e., the roll angle). This was likely due to the relatively large roll angle of the skull as positioned in the holder. Together, the results represented in Fig. 4.15 demonstrates that the quality of the resulting corrected PAM is sensitive to registration of the skull, especially to translations. While registration of the sound speed data and physical arrangement of the transducer is necessary, this capability is extant in present transcranial FUS applications.[140,141]

4.4.5 Computational Efficiency

As iterated throughout this work, a central advantage of the ASA is its computational efficiency. While both the full and stratified corrections incur additional computational expense compared to the uncorrected case, they are still of great interest compared to other aberration correction methods provided that the order of magnitude is com-

Table 4.3: Mean and standard deviation PAM computation times for the uncorrected [Eq. (4.2.5)], corrected [Eq. (4.2.6)], and stratified [Eq. (4.2.7)] beamforming.

	Uncorrected	**Corrected**
HASA	44 ± 4 ms	166 ± 37 ms
Stratified	43 ± 44 ms	125 ± 125 ms

parable (recall Fig. 4.4). Table 4.3 reports the computational times required for the uncorrected and corrected 2D PAMs in the stratified and heterogeneous ASA cases described in Secs. 4.4.1 to 4.4.3. Note the grid sizes differed between the trans-skull and stratified cases, but the comparison between the corrected and uncorrected are fair for each. The results confirm that the ASA remains computationally efficient in both the stratified and fully heterogeneous cases. For the experimental case, the HASA correction required approximately 1/3 more time than the uncorrected case. For 234-by-234-500 point computational grid, 2.100 ± 0.016 s were required for the conventional ASA, while the HASA took 2.780 ± 0.041 s per point. These computations could be improved with more considered vectorization of the operations.

4.5 Summary of Contributions

In this chapter, it was demonstrated through experimental and simulation studies that the HASA method derived in Chap. 2 can address successfully localization errors caused by aberrations induced by a non-uniform medium. In the simulated trans-skull case, errors were seen to be reduced from about 3 mm to less than 1 mm across a range of frequencies, apertures, and source positions. While the skull did not well enough approximate a stratified medium for the analytical solution, this result did appreciably reduce the localization error for more slowly-changing layered media. In volumetric experimental experiments, the error lower bound was reduced five-fold and the image correlation doubled with the HASA compared to the uncorrected case. Additionally, the stratified medium correction provided sub-wavelength localization accuracy at biologically relevant scales and frequencies. Finally the methods were shown to be computationally efficient. While the corrections require an approximately threefold increase in computation time compared to the homogeneous ASA, these times remained an order of magnitude below those required for spatial domain calculations. Together, these results indicate significant relevance of the method to applications in trans-cranial passive acoustic mapping.

Chapter 5
Improving Resolution

5.1 Introduction

5.1.1 Limitations on Resolution

Ultrasonic imaging, like any wave-based imaging, is hindered by fundamental physical limitations of diffraction due to the spatial extent of the wave, as well as the finite aperture of the imaging array.[41] This constraint— termed the "diffraction limit"— was first stated[142–144] as the required separation of two point ideal sources such that their diffraction patterns do note overlap[†]

$$\Delta x_{\min} \approx 0.61\lambda \times \frac{d}{a}, \tag{5.1.1}$$

where λ is the wavelength, d is the distance from the aperture and a is the radius of the circular aperture through which the sources are imaged; see Fig. 5.1. The constant of proportionality in Eq. (5.1.1) corresponds to the first root of the the Bessel function $J_1(x)$, which defines the spatial extent of the source image.

For megahertz frequencies in tissue, and imaging depths and apertures of centimeter order, the resulting theoretical resolution limit is on the order of 1 mm. A more full characterization of the maximum achievable resolution is given by the point spread function (PSF) of the system,[1] which includes effects such as aberration, and

[†]In the case of a circular aperture, the intensity pattern is governed by

$$I \propto \left[\mathrm{Jinc}\left(ka\sin\theta\right)\right]^2,$$

where $\mathrm{Jinc}\,\xi \equiv J_1(\xi)/\xi$ For small angles, (i.e., the object is near the center of the aperture), $\sin\theta \simeq \theta$, and the first null of $J_1(\xi)$ occurs at $\xi = 3.8317$. Then, since $\Delta x = d \cdot \theta$, the first minimum of the intensity occurs at[145]

$$ka\sin\theta = ka\sin\left(\Delta x/d\right) \simeq \left(\frac{2\pi}{\lambda}\right) a\frac{\Delta x}{d} = 3.8317 \implies \Delta x = 1.2197\frac{d\lambda}{2a}.$$

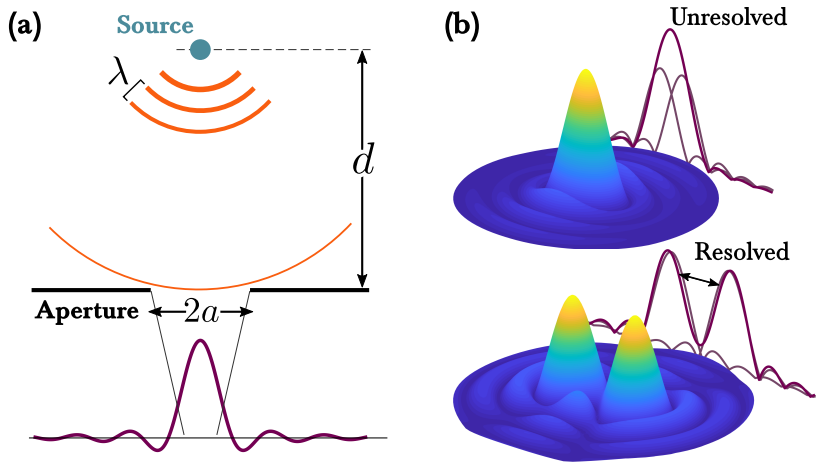

FIGURE 5.1: Effect of diffraction on image resolution. **(a)** When a point source is imaged through a circular aperture of radius a, the resulting intensity distribution has spatial extent governed by the incident wavelength. **(b)** Resolving two sources requires spatial separation according to Eq. (5.1.1).

provides a lower limit on its ability to resolve closely spaced point sources. While this blurring of subwavelength sources in the image is an inevitable consequence of the physics recent work has sought to exploit acquisition and data processing techniques to circumvent the limitation characterized by the PSF.

5.1.2 Super-resolution

"Super-resolution" refers in general to any method that achieves an effective resolution below the classical limit given by Eq. (5.1.1). Improving the resolution of optical systems has been of interest in biology for many decades, as the size of cellular structures falls below this limit for optical wavelengths ($\Delta x_{\min} \sim 200\,\mathrm{nm}$).[146] Techniques involving larger effective apertures[147,148] improved the effective resolution, but were still subject to diffraction. Seminal advances[†] came at the beginning of the 21st century through patterned excitations,[149–152] and the successive localization of stochastically blinking photophors.[153–155] Such advances have enabled visualization of cellular structures as small as 20 nm,[156] representing a tenfold improvement of the classical limit.

Inspired by these optical techniques in optical microscopy,[154,155] and with evidence that scattering from individual microbubble contrast agents could be detected,[157] acoustic techniques exploit the successive localization of individual microbubble contrast agents over time, which are sufficiently sub-wavelength to be treated as point

[†]The 2014 Nobel Prize in chemistry was awarded to E. Betzig, S. Hell, and W. Moerner "for the development of super-resolved fluorescence microscopy."

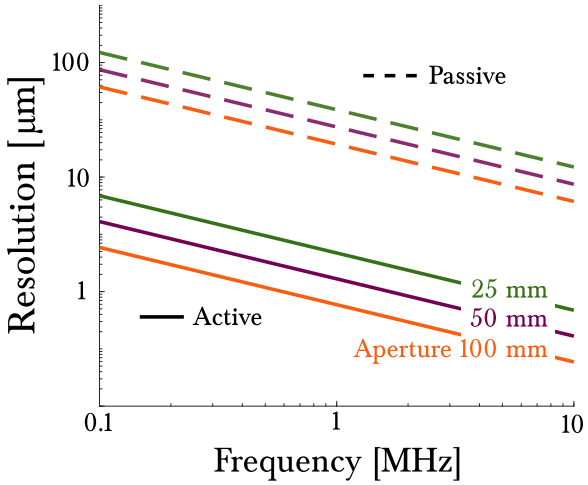

Figure 5.2: Lower bounds on the lateral resolution for active (solid lines) and passive (dashed lines) images with the indicated aperture at 10 cm depth in water. The active limit is given by Eq. (10) of Ref. 164, with SNR of 60 dB, 50 % bandwidth, signal correlation $\rho = 0.9$, and a time kernel scaled relative to 30 μs for 5 MHz.[165] The passive limit is given by Eq. (11) of Ref. 124.

sources.[158] These so-called "super-resolution" (SR) or "ultrasound localization microscopy" (ULM)[†] techniques use successive localizations of single point source separated in time to allow identification of sources that are too closely spaced (i.e., below the diffraction limit) to be resolved simultaneously.[15] This is of particular importance for PAM, whose resolution is typically worse than active methods due to the lack of time-of-flight information [see Fig. 5.2].

In SR techniques, intensity peaks in the acoustic image are replaced with a single point from one[158] or several[15] bubbles isolated in each frame with non-overlapping PSFs, and thus the beamforming and point source localization methods are of primary importance. Most existing literature employs active acoustic imaging (e.g., B-mode or ultrafast plane wave imaging),[166] wherein the (linear) signal scattered by a single bubble forms the basis for the point source localization [Fig. 5.3(a)]. Localization is most commonly performed by Gaussian fitting of the peaks of the image intensity due to the bubble sound scattering[19,167–170] and reduction of the PSF to a single point. However, in the presence of several sources in the same image, only strong scatterers—which might erroneously including linear tissue response rather than contrast agents—meet the acceptance criterion per frame, which incurs a narrower dynamic range and limits the number of bubbles super-localized per frame, increasing acquisition time. Other

[†]Strictly, ULM is a specific super-resolution technique that uses super-localization of microbubbles. While other acoustic super-resolution techniques that do not rely on ULM have been proposed,[159–162] this is the method most widely studied for the applications discussed here.[163]

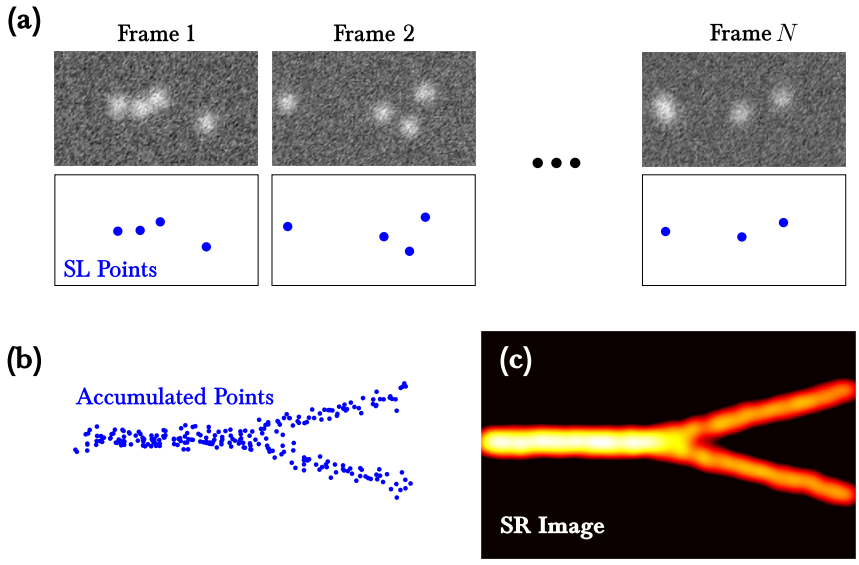

FIGURE 5.3: Procedure for ultrasound localization microscopy. **(a)** Super-localized points are isolated from the raw contrast-enhanced ultrasound frames. **(b)** Once many peaks are isolated, they can be **(c)** combined to form the final super-resolution image.

localization methods include, center of mass calculations,[158,171] time domain fitting of the RF data,[172–174] statistical approaches,[160,161] and the use of acoustic metamaterials.[162,175] These SR approaches have demonstrated better than an order of magnitude improvement in the effective resolution (up to 20-fold), and produced intriguing images of vasculature and good estimates of flow velocities in microvessels.[15,171,176,177]

One of the main challenges in these methods is the separation of the bubble signal from random motion and tissue scattering; this can be exacerbated in low flow vessels (below 1 mm/s,[178] which are also the vessels of interest for SR techniques due to their size.[179] Contrast harmonic imaging, in which bubble localization is based on microbubble nonlinear echoes, could potentially mitigate this problem,[158] albeit at the cost of lower frame rate and increased risk of microbubble collapse or deflation due to the need for strong nonlinearities (i.e., high SNR), which might prevent effective bubble tracking.[166] Additionally, full accounting of out of plane motion necessitates volumetric imaging,[180] which requires extended acquisition times and added computational expense.[172] PAM based on the ASA is well suited to address these issues, since it has excellent frequency selectivity compared to active methods,[19] may detect sources even at SNRs below 0 dB,[25] is significantly more efficient than time domain methods[19,20,181] (which is of particular importance for 3D imaging), and allows for corrections due to heterogeneity of the medium as discussed previously.

While both passive and active methods are able to resolve vessels at an order of magnitude below the diffraction limit, currently the analysis of the vascular structure, which is important for diagnosis, is in its infancy.[180,182–184] Likewise, methods for accurate and quantization-free estimation of microvascular velocity have received more attention only recently, with methods originally developed for transportation analysis[185] providing the most promising approach.[167,171] Formal and computationally efficient methods to analyze the SR image content could play major role in determining the lower limit on the number of points required, which is important for optimizing the acquisition time, reducing motion artifacts, and extracting diagnostically useful information.

In this chapter two methods are proposed for application in acoustic super-resolution imaging. The first is a method based on morphological image processing techniques to super-localize intensity peaks due to microbubbles from the raw contrast-enhanced frames. The second technique employs local projection of the peaks to identify vascular structure and size. The performance of these methods on both PAM data and from an *ex ovo* chicken embryo model are evaluated and results compared to the diffraction limited case. Together, these methods—which are both computationally efficient and agnostic to image dimension (i.e., 2D or 3D data) or modality—have significant promise for microvascular quantification.

5.2 Super-resolution Methods

The proposed vessel imaging and quantification process comprises two steps: first, individual bubbles must be super-localized within the diffraction-limited image to obtain a point cloud (peak detection). Then, the peaks are associated in time and space to infer information about the vessel's size, structure, and flow velocity.

5.2.1 Peak Detection

The first task in the generation of super-resolution is super-localization, in which the signal due to microbubble scattering is isolated from the raw acoustic image, and replaced with a point representing the contrast agent position. The steps involved in using MR to accomplish task are enumerated in the following sections.

5.2.1.1 Filtering, Interpolation, & Smoothing

Some pre-processing of the data common in many SR techniques enables improved localization of the microbubbles. First, SVD filters are applied to remove the most

slowly changing (i.e., signal due to scattering from tissue) and most quickly changing (i.e., pixel intensity fluctuations due to noise) from the image stack. The details of the filter itself are elaborated in Appendix C.

Next, the maximum resolution of a digital image is most basically limited by its pixel dimensions. As the processing of raw images described in this chapter aims to improve the image resolution, all raw images must be interpolated such that the new pixel size is, at most, smaller than the size of the objects whose identification is desired. The choice of pixel size for an imaging system is motivated by balancing the lower fundamental limit on resolution (i.e., that imposed by wavelength, bandwidth, sampling, noise, etc.) and practical considerations such as the required memory and available buffer size (interpolating an image four times requires 16 times as many pixels). Finally, prior to the peak isolation process, the data are smoothed with a Gaussian filter with spatial extent on the PSF. This step serves to regularize the intensity variations in the image and identify the peak regions as discussed in Sec. 5.2.1.2.

5.2.1.2 Morphological Reconstruction

The reconstruction technique proposed herein employs techniques from mathematical morphology, specifically the dilation. Though generalizable to continuous distributions, its development and motivation for many of its techniques are in the context of image processing (i.e., on discrete grids). Initially, its fundamental operations were defined on binary images, though the analysis was subsequently extended to grayscale images.[186] In a manner similar to the convolution operation, the fundamental operations of morphology employ an image and template, termed a "structuring element". For a function $f(\boldsymbol{r})$ on some region $\mathcal{D}$ with template $b(\boldsymbol{r}')$[†]

1. The **dilation** of f by template b is defined as

$$(f \oplus b)(\boldsymbol{r}) = \sup_{\boldsymbol{r}' \in \mathcal{D}} [f(\boldsymbol{r}') + b(\boldsymbol{r} - \boldsymbol{r}')].$$

   That is, every value of f is replaced with the maximum value of $f + b$ within a neighborhood defined by local support of $b(\boldsymbol{r}')$.

2. The **erosion** of f by template b is defined as

$$(f \ominus b)(\boldsymbol{r}) = \inf_{\boldsymbol{r}' \in \mathcal{D}} [f(\boldsymbol{r}') - b(\boldsymbol{r} - \boldsymbol{r}')].$$

[†]These functions are often discussed in terms of digital images, which take discrete values (e.g., $f \in [0, 255]$). However, the formulation for continuous functions extends naturally to discrete-valued data.

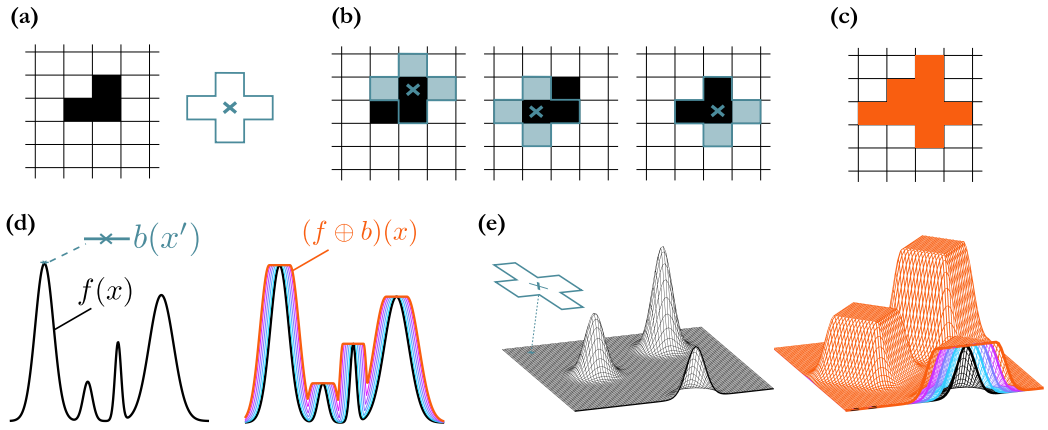

Figure 5.4: Morphological Dilation. **(a)** A binary image and template (blue). **(b)** For each non-zero point, points within the region of the template are added to the set. **(c)** The dilated binary image. **(d)** For a continuous 1D function, the dilation is its maximum value as weighted by the template (blue line). **(e)** The process may be extended to 2D with a 2D template (blue), and the process may be iterated.

That is, every value of f is replaced with the minimum value of $f - b$ within a neighborhood defined by b.

The process of dilation is illustrated in Fig. 5.4.

The definition of morphological reconstruction may now be stated. First, denote as $\delta_g(f)$ as the dilation of f under g, that is to say

$$\delta_g(f) = (f \oplus b) \wedge g\,, \tag{5.2.1}$$

where $\wedge$ represents the point-wise minimum. Then, write iterated dilations as $\delta_g^{(n)}(f)$, that is,

$$\delta_g^{(n)}(f) = \underbrace{\delta_g(\delta_g(\cdots(\delta_g(f))\cdots))}_{n \text{ times}} \tag{5.2.2}$$

The reconstruction of f from g is then written

$$\rho_g(f) = \bigvee_n \delta_g^{(n)}(f)\,, \tag{5.2.3}$$

where the $\vee$ notation indicates that the point-wise maximum is taken, and the iteration is repeated until it stabilizes (i.e., until the output ceases to change upon further iterations). The reconstruction operation described by Eq. (5.2.3) repeatedly dilates the grayscale image until it is restricted by the mask.

In its use for super-resolution, the mask is defined as a scaled version of the original image. As suggested by Vincent,[187] the subtraction of the reconstructed signal from the original results in easily segmented peak regions (or "h-domes") representing local maxima. The chief advantage of this technique is that the resulting local domes will have comparable amplitudes in the reconstructed image, even when their amplitudes in the original image are quite different; see Fig. 5.5. However, information about the size (i.e., spatial extent) of the intensity peak is retained in the reconstructed image; see Sec. 5.2.1.4.

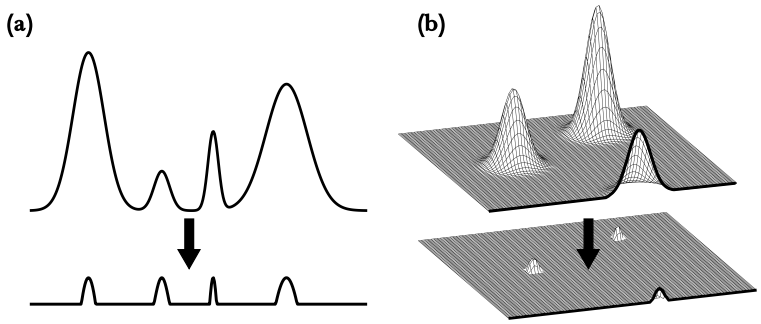

Figure 5.5: Peak regions ("h-domes") found via morphological reconstructions with a shifted version of the image intensity. Intensity distribution (top) and resulting peak regions (bottom) for **(a)** 1D, and **(b)** 2D intensity distributions. Distributions were taken to have peak intensity of unity, and morphological offset $h = 0.1$ was used.

5.2.1.3 Super-Localization

While the MR technique described in Sec. 5.2.1.2 identifies peak regions within the ultrasound image, it remains to identify the peak location. While the location of the peak intensity or centroid of the region are reasonable choices, the notion that an isolated point scatterer will appear as the PSF in the image suggests that knowledge of the PSF should be exploited. Here, once the peak regions have been identified, the PSF of the system is cross-correlated with each peak region. The maximum value of this convolution identifies the best agreement between the observed in the image, and that expected for a point source, and therefore the most likely position of the scatterer. This method produced the smallest axial error in a systematic study, unless detection of the scattering event from the time series data is possible.[188]

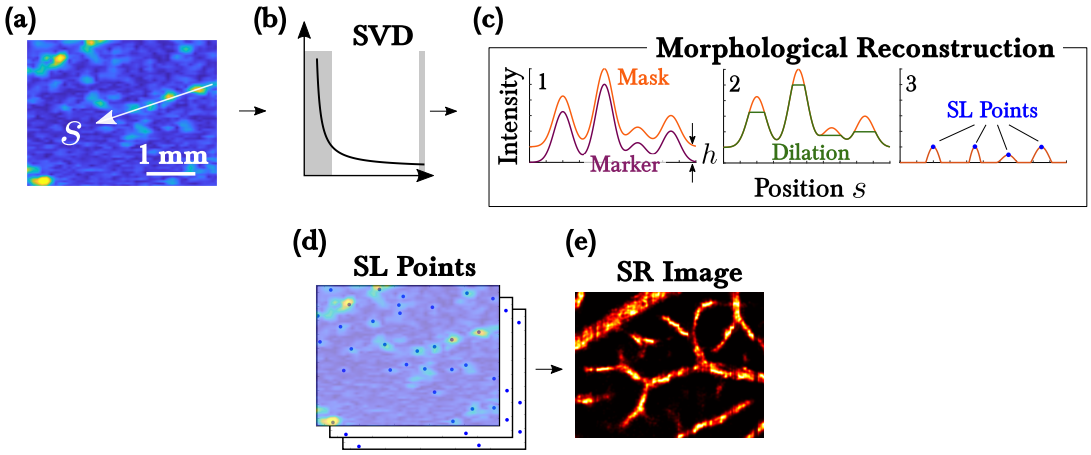

FIGURE 5.6: Super-resolution ultrasound with morphological reconstruction **(a)** Contrast-enhanced ultrasound (CEUS) were acquired with ultrafast plane wave imaging. **(b)** Singular value decomposition (SVD) filtering differentiates tissue from flowing contrast agents. **(c)** Morphological reconstruction with the intensity from the filtered frames scaled by $(1 - h)$ as the mask enables isolation of peak regions, and convolution with the PSF identifies super-localized (SL) points (blue dots). **(d)** Accumulation of SL point locations from all frames and **(e)** superimposed Gaussian profiles centered at these locations produces the super-resolution image.

5.2.1.4 Are Peaks Single Bubbles?

Typically, low bubble concentrations are used for super-resolution processes to ensure spatial separation of the scatterers and thus enable isolation of individual scatterers. However, simultaneous optical microscopy has suggested that there are many more microbubbles in the field of view than are detected by super-localization algorithms.[189] It is further possible that a small cloud (less than 10) bubbles, which is still smaller than the wavelength, will appear in the images as a point scatterer, and thus will be localized as a single bubble.

Figure 5.7 demonstrates the effect of the raw peak amplitudes and extents on the amplitudes and sizes of the peak regions obtained by the morphological reconstruction. A one-dimensional "image" which comprises superimposed Gaussian signals of constant standard deviation $\varsigma/2$, but with differing amplitudes is shown in blue in Fig. 5.7(b). The morphological reconstructions of the image with the indicated offsets are shown (shifted down for visibility). Figure 5.7(c) shows that, as the amplitude of the raw peak A is increased, the size of the peak region decreases slightly, but in all cases have size on the order of ς. Thus, if all peaks have the same standard deviation (i.e., have area the size of the PSF), the size of the peak regions in the reconstructed

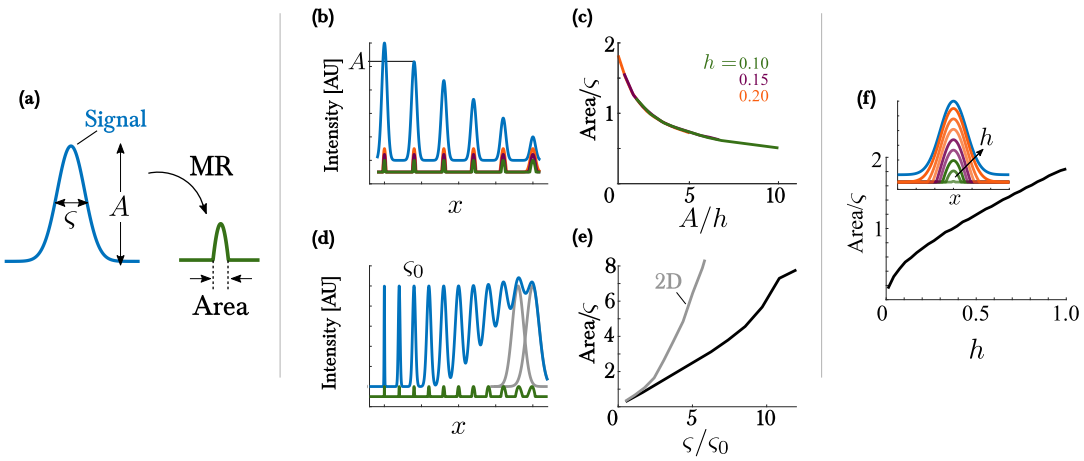

FIGURE 5.7: **(a)** Meaning of variables for the signal (blue) and its reconstruction (green). **(b)** Raw intensity distribution (blue) and its morphological reconstruction for the indicated offsets. **(c)** Normalized area of each peak region in (a) as a function of the raw peak amplitude. **(d)** Distribution comprising equal-amplitude Gaussians with increasing standard deviations (blue) and its reconstruction with offset h=0.1. **(e)** Normalized area of the peak regions as a function of the width ς of the peak in the raw image in one (black line) and two (gray line) dimensions. **(f)** Normalized area of the peak region as a function of the offset h.

image will be similar, regardless of the amplitude in the raw image. In Fig. 5.7(d), the amplitudes of the Gaussian peaks are now held constant and the standard deviation is varied. Figure 5.7(e) shows that for larger standard deviations, the size of the peak region in the reconstructed image becomes significantly larger. This effect is exacerbated in 2 dimensions, where the normalized area of the peak regions grows as ς^2 [gray line in Fig. 5.7(e)]. Thus, peak regions with sizes much larger than the reference size (here ς; in the case of the bubble images, this is the size of the PSF) correspond to signals in the raw image that are larger than the reference size. The size of the peak regions in the reconstructed image might then discriminate between signal due point scatterers that due to larger structures. Finally, Fig. 5.7(f) confirms that the size of the intensity peak dominates the size of the peak region in the MR. As the offset h is increased, the size of the resulting peak region grows modestly, but for all offsets has similar order to the size of the original peak (i.e., ς). Thus while the size of the peak regions obtained with MR will give good evidence that the size of the scatterer is at most a wavelength, further evidence was also sought from comparison with other imaging modalities. For the case of the *ex ovo* embryo data (see Sec. 5.3.3), optical micrsocopy data of the same vasculature was available. In this case, the final SR images were registered to the optical data, and a binary mask created from the op-

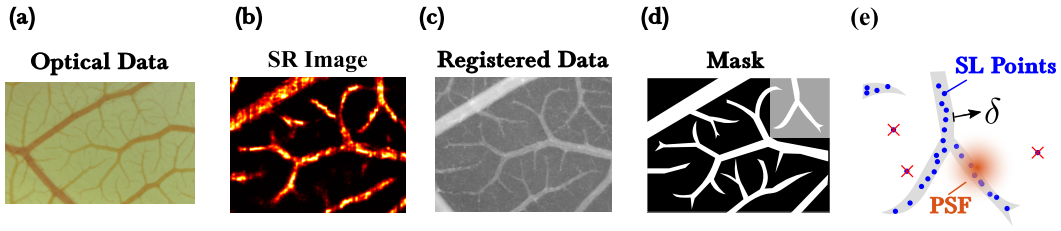

FIGURE 5.8: Optical Data Registration **(a)** Optical microscopy images were registered with **(b)** the super-resolution image created from the super-localized points. **(c)** The Registered data were then thresholded **(d)** to create a binary mask. **(e)** The SL points may be considered successful (if within some tolerance δ of the vessel) or spurious (if they are outside, red x's).

tical data (Fig. 5.8). Then, the super-localized points could be compared to this mask, and the fraction of points that were localized within the identified vessels could be determined. Optical data were registered using MATLAB's image processing tools: First, `imadjust` was applied to even the image contrast, and `imregister` to find the optimal translation, rotation, and scaling for alignment. Finally, a threshold binarization (`imbinarize`) was performed, and small regions identified as noise removed through morphological closure (`imclose`) with an empirically determined neighborhood. As the registration was imperfect, a small (tens of microns) tolerance δ was defined, such that SL that were outside the mask, but within δ of the mask, were counted as true bubble localizations. Comparison of the number of true (i.e., within the vessel) and spurious localizations will give indication of whether the localizations are indeed bubbles—or at least some subwavelength scatterer within the vasculature.

5.2.2 Vessel Quantification

The repeated localization of sources yields a point cloud that will resemble the vessel's shape and thickness. Conventionally, a Gaussian intensity distributions (with variances on the order of the point spread function) are summed to form a composite SR image, from which, e.g., vessel diameters may extracted with image processing techniques. However, the distribution of points themselves may also provide analytical information about the vessel size and structure, and thus potentially diagnostically relevant information. In this section, a local projection and segmentation technique is proposed for the automatic quantification of the vasculature.

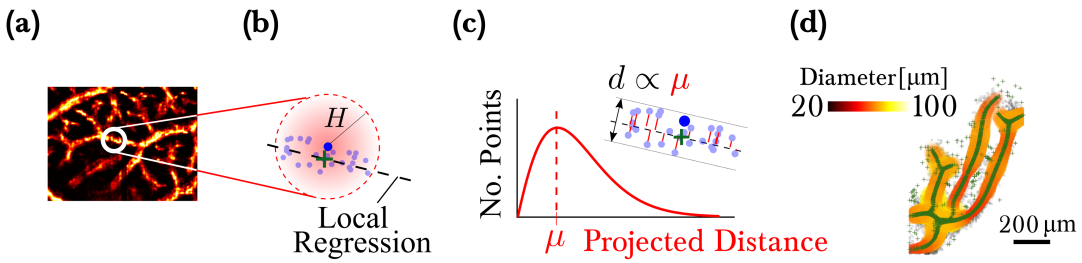

FIGURE 5.9: Process for vessel characterization from the super-localized points. **(a)** Once the points for the super-resolved image have been found (as in Fig. 5.6), **(b)** a weighted local regression is calculated from the points within distance H of each point. **(c)** The distribution of the distances from this regression is taken to be proportional to the vessel diameter. **(d)** In this way, a point-wise diameter estimation is obtained directly from the super-localized points.

5.2.2.1 Local Projection

First, local projection was used to identify the vessel center. For each super-resolved point, a local linear regression is computed from all points within distance H with Gaussian-weighting. Once the local regression was computed, the super-resolved peaks may be projected onto this best fit line; see Fig. 5.9(a–b). This process may be iterated to further collapse the points onto a single line, an estimation of the vessel's center. In three dimensions, points may be projected onto the principal direction (i.e., a line parallel to the eigenvector associated with the largest singular value) with no weighting, as general solution of the weighted regression is not available.[190]

In cases closely spaced vessels (on the order of the vessel diameter), it is necessary to include in the regression calculation only points which are associated with the same vessel. Otherwise, points from nearby vessels will be included in the local regression and subsequently projected into the region between vessels (Fig. 5.10 left column). If however, as suggested by Lee,[191] a Euclidean minimum spanning tree (EMST) may provide an estimate the connectivity of the point cloud.[192,193] The EMST is the graph connecting a set of points such that all points are connected, and the total length of the edges, defined as the Euclidean distance between points, is minimized. Since the edges of this In this way, separate vessels are segmented by removing any edge whose length exceeds a threshold number of standard deviations from the mean edge length of the EMST. With knowledge of this segmentation, only connected points, i.e., those within the same vessel, are included in the projection (Fig. 5.10 right column).

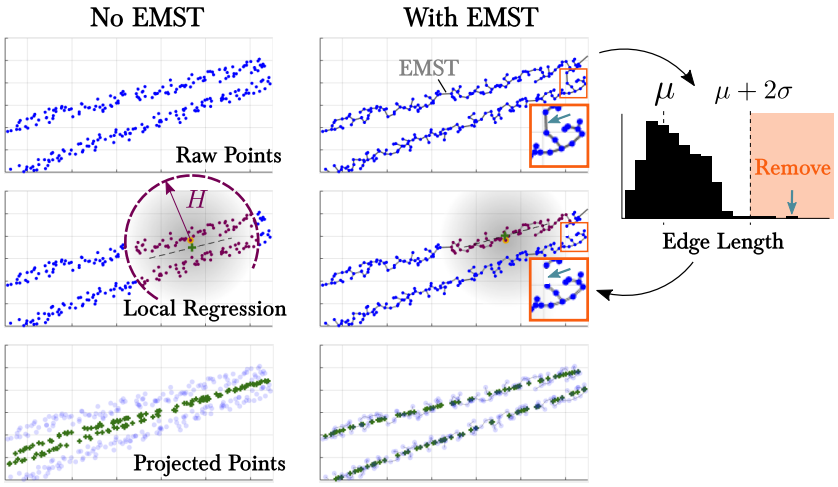

FIGURE 5.10: Local projection of super-localized points without (left column) and with (right column) use of the EMST. For closely spaced vessels (top row) the local regression may inclide points from adjacent vessels (middle row). Segmentation by deleteing the longest edges of the EMST alleviates this problem.

5.2.2.2 Minimum Spanning Tree

While the details of the EMST calculation are not of central interest, an outline of its calculation in this context merits some consideration. First, each of the N super-localized points is treated as a graph vertex, edges are drawn between each, and the distance between nodes is set as the weight of that edge. the complete graph (i.e., edges connect each vertex to every other vertex) will have $N(N-1)/2$ edges. To reduce the number of edges that must be checked, common implementations fist find the Delaunay triangulation of the points [Fig. 5.11(b)]. Since this triangulation is guaranteed to contain the nearest-neighbor graph (i.e., the set of edges that connects each vertex along its lowest-weighted edge), this smaller subset graph may be searched.

Prim's algorithm[192] then performs the following steps to find the EMST:

1. Initialize EMST at an arbitrary starting vertex $T = \{V_0\}$ [Fig. 5.11(c.i)].
2. Find the lowest weight edge $E_{\min}$ connected to any vertex in E.
3. Add the new vertex $V_{\min}$ connected to $E_{\min}$ to T [Fig. 5.11(c.ii)].
4. Repeat steps 2 and 3 until the tree T has $N-1$ edges [Fig. 5.11(c.iii–iv)].

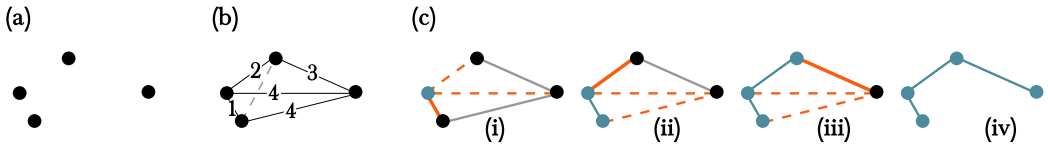

Figure 5.11: Illustration of Prim's algorithm. **(a)** The set of is super-localized points. **(b)** The Delaunay triangulation is used to find the starting graph (note the gray dashed line, which is part of the complete graph, is excluded). **(c)** The EMST is initialized and shortest possible edge added each time.

5.2.2.3 Velocity Estimation

To estimate the velocity of the individual peaks as a proxy for the blood flow, a simple pairing algorithm was employed. For each super-localized peak in frame N, the peak with its nearest-neighbor in the subsequent frame $N+1$ was determined with a simple nearest-neighbor search.[194] In cases where two peaks were associated with a single peak in another frame, the shortest path was retained. The velocity was then defined as

$$\boldsymbol{v}(\boldsymbol{r}_i) = \frac{\boldsymbol{r}_i^{n+1} - \boldsymbol{r}_i^{n}}{\Delta t}, \tag{5.2.4}$$

where $\boldsymbol{r}_i^n$ is the position of the super-localized point i in frame N, and $\Delta t = 2\,\mathrm{ms}$ was the time between frames.

5.3 Simulations and Experiments

This section describes the experimental data obtained with both passive and active acoustic imaging modalities, and simulated data for passive imaging to verify the efficacy of the morphological reconstruction and local projection algorithms.

5.3.1 PAM Experiments

A vessel-mimicking bifurcation was prepared by joining two polyethylene tubes with inner diameter 280 µm and separating them to form a bifurcation. Optison microbubbles (GE Healthcare, Chicago, IL, USA) were diluted to approximately 200 bubbles/µL in a stirred beaker, and continuously drawn through the phantom with a syringe pump during the experiments. A 256-element linear array transducer (GE L3-12D) was positioned in the plane of the vessel phantom (parallel to the bifurcation). The array was connected to a research ultrasound system (Verasonics, Kirkland, WA, USA) pro-

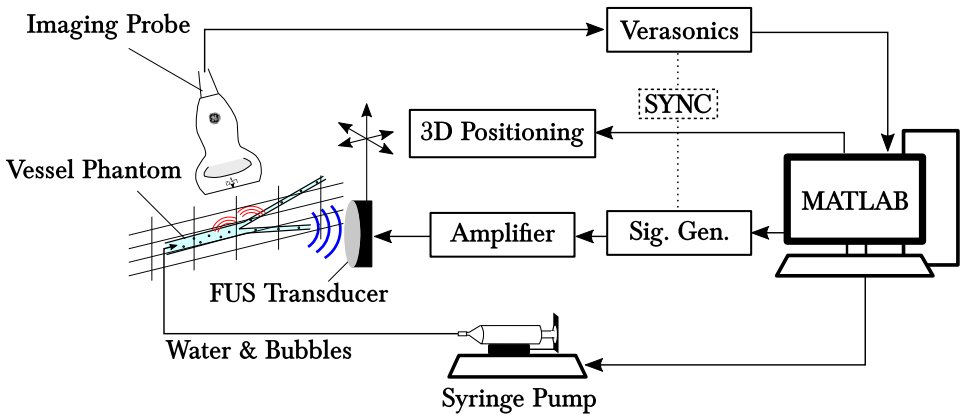

Figure 5.12: Setup for PAM super-resolution experiments. A central workstation scanned the focal position of the transducer over a 2D grid containing the vessel phantom, through which bubbles were flowed by the syringe pump. The signal generator triggered the Verasonics system, which recorded the bubble emissions through the imaging probe and saved the data for post-processing.

grammed to operate in passive mode (center 128 channels) to record microbubble emissions. The setup is shown in Fig. 5.12.

To ensure that the nonlinear emissions from the bubbles were free of nonlinear artifacts originating from the excitation pulse, we employed a focused ultrasound (FUS) transducer (custom built, center frequency 1.662 MHz; curvature 30 mm and diameter 40 mm). The transducer was focused on an air-filled tube submerged in a water tank by maximizing the echo recorded by a pulser-receiver (Olympus, Waltham, MA, USA), and then scanned in a plane parallel to the plane of the vessel phantom with a 3D positioning system (Velmex, Bloomfield, NY. The FUS excitation signal (sinusoidal, center frequency 1.662 MHz; pulse duration 30 µs; focal amplitude 450 kPa) was coded on an arbitrary waveform generator and amplified by a 43 dB (Mini-Circuits, Brooklyn, NY, USA) amplifier connected to the FUS transducer. Pulse repetition frequencies up to 20 Hz were used (except when the transducer was re-positioned), and the microbubble emissions were recorded during the excitation pulse. All hardware was synchronized and controlled with MATLAB, and the focal pressure was determined via measurement with a calibrated a hydrophone (Onda, Sunnyvale, CA, USA) with a reported uncertainty of 10 % in the frequency range of the excitation.

5.3.2 PAM Simulations

Acoustic simulations were performed in MATLAB using k-Wave[23] including linear acoustic propagation effects. First, a binary map was created from a trace the B-mode image of the vessel phantom used for the experiment, or of a shape designed to test the effects of the algorithm. Source locations were then defined randomly within the binary region, with a minimum separation of 4 mm to ensure spatial separation in the PAMs—i.e., that their resulting point spread functions did not overlap. At each source location, the pressure was specified to be the time series pressure radiated by a bubble with radial time series $R(t)$[130]

$$p_{\mathrm{rad}} = \frac{\rho_0}{r}\left(R\ddot{R} + 2R^2\right), \tag{5.3.1}$$

where dots denote time derivatives (i.e., $\dot{R} = \mathrm{d}R/\mathrm{d}t$). For the simulation, the p_{rad} was evaluated at $r = 100\,\mu\mathrm{m}$, corresponding to the discretized spatial step in the simulation.

Each bubble's radial time series $R(t)$ was computed from the large-amplitude bubble model due to Marmottant et al.[126] This model augments Rayleigh–Plesset type models that bubble shell effects[195,196] by specifying a radially-dependent surface tension to capture the buckling of the bubble shell. Specifically, $R(t)$ was found by solving

$$\rho_0\left(R\ddot{R} + \frac{3}{2}R^2\right) = \left[p_0 + \frac{2\sigma(R_0)}{R_0}\right]\left(\frac{R}{R_0}\right)^{-3\kappa}\left(1 - \frac{3\kappa}{c_0}\dot{R}\right) - p_0 - 2\frac{\sigma(R)}{R} - 4\frac{\mu_0\dot{R}}{R} - 4\frac{\kappa_s\dot{R}}{R^2} - p_{\mathrm{inc}}\,. \tag{5.3.2}$$

In Eq. (5.3.2), c_0, ρ_0, p_0, and μ_0 are the sound speed, density, ambient pressure, and viscosity of the surrounding fluid (water) respectively. The radius-dependent surface tension σ is given by an ad hoc law of the form

$$\sigma = \begin{cases} 0 & R < R_b \\ \chi\left[(R/R_b)^2 - 1\right] & R \in [R_b, R_r] \\ \sigma_0 & R > R_{\mathrm{r}}\,, \end{cases} \tag{5.3.3}$$

where R_b is the radius below which the shell will buckle, and R_r is the radius above which the shell will rupture (i.e., there will be contact between the gas core and surrounding liquid. The parameters used are listed in Table 5.1 Bubble properties were estimated for Optison bubbles based on data measured for Definity[197] and

Table 5.1: Parameters used in Eqs. (5.3.2) and (5.3.3).

Symbol	Parameter	Value
R_0	Equilibrium Bubble Radius	2.8 µm
κ_s	Surface Dilatational Viscosity	15×10^{-9} N
χ	Linear Elastic Modulus	0.55 N/m
R_b	Buckling Radius	R_0
R_r	Rupturing Radius	$1.01R_0$
p_0	Equilibrium Pressure	1.01×10^5 Pa
c_0	Liquid Speed of Sound	1500 m/s
ρ_0	Liquid Density	1000 kg/m^3
μ_0	Liquid Viscosity	1 mPa s
σ_0	Reference Surface Tension	7.28 mN/m
$\|p_{\text{inc}}\|$	Applied Pressure Amplitude	450 kPa

Sonovue.[126] The applied pressure field was taken to be a 20-cycle windowed sine pulse at 1.662 MHz (as used in the experiments). The simulated resulting pressure field was then recorded at locations corresponding to the position and dimensions of the ultrasound array used during the experiment.

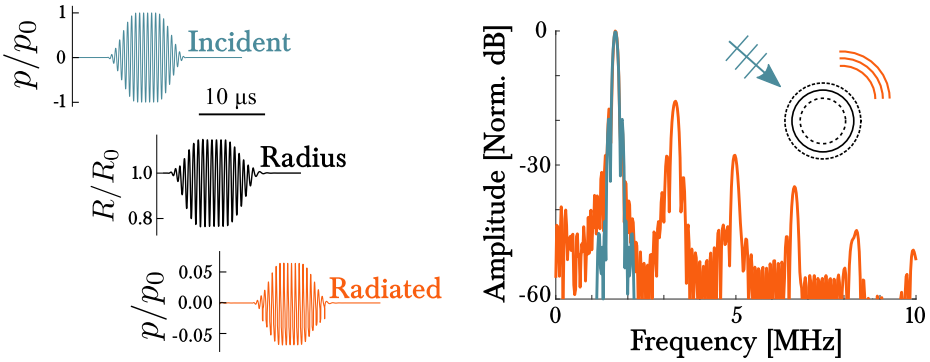

Figure 5.13: At left are time series of the applied pressure resulting normalized bubble radius from Eq. (5.3.2), and radiated pressure from the bubble, relative to the applied pressure magnitude from Eq. (5.3.1). At right are the spectra of the incident and radiated pressures, showing the harmonic generation due to the nonlinearity of the oscillations.

For the three-dimensional simulations, a 64-by-64 element virtual 2D array with 500 µm pitch was defined to record the simulated pressure field. Point sources at 1 MHz were randomly simulated within a vessel phantom and helix shape. The lower frequencies and larger dimensions were used to enable use of a coarser simulation grid, and reduction of the required computational resources.

5.3.3 *Ex ovo* Embryo Model

To test the performance of the SR algorithm with realistic vasculature, CEUS images were collected of vasculature in the chorioallantoic membrane (CAM) of chicken embryos. Additionally, data were taken from renal cell carcinoma xenograft models that were grown in the CAM of chicken embryos. Full details of the model preparation can be found in Refs. 198 and 199. This model is attractive due to the long microbubble recirculation times, small bulk tissue motions, the availability of healthy and aberrant tumor vasculature, and the ability to directly compare the US images with high resolution optical microscopy images of the vasculature. A bolus injection of microbubbles (Lumason, Bracco Diagnostics Inc., Monroe Township, NJ) at 1.8×10^9 microbubbles per milliliter, and imaging acquisitions were performed at the microbubble concentration plateau after the injection.

Contrast enhanced ultrasound (CEUS) images were obtained with a research ultrasound system (Verasonics) with a 25 MHz linear array transducer (L35-16vX, Verasonics). Ultrafast plane wave imaging (15 angles, –7° to 7°) was performed at 500 frames per second at a frame rate with 5 V transmit excitation. At each location, 5 successive acquisitions of 720 frames each (total acquisition length 3600 frames over 7.2 seconds). The IQ data were stored and post-processed with custom MATLAB (MathWorks, Natick, MA, USA) scripts on a standard desktop computer (4 cores at 2.8 GHz, 16 GB of memory).

For the chicken embryo model, optical microscopy of the healthy vasculature was also available. Thus in this case to determine the accuracy and quality of the peaks found via MR, the final SR image (i.e., the intensity field due to the summed Gaussian distributions at each SR peak location) was registered with an optical microscopy image of the vasculature (via MATLAB's `imregister`). From the registered optical data, a binary mask was created as a reference standard, such that SR points in the acoustic image within the mask are considered true positives, i.e., they fall within the vasculature and may be considered microbubble localizations. As the registration is imperfect, a tolerance distance δ was defined such that if the SL points were less than δ from the vessel mask, they were considered successful localizations. Finally, knowledge of the mask area and size of the imaging wavelength were used to estimate the upper bound on the number of bubbles that could be localized (i.e., the area of the vessel mask divided by the size of a square wavelength).

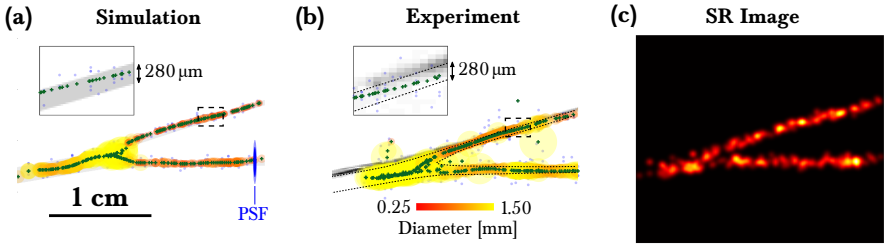

FIGURE 5.14: Simulation verification of super-resolution with PAM. **(a)** Super-localized points (gray points) and locally-projected points (green crosses) compared with the region in which sources were located in the simulation (gray region). Inset shows enlarged region indicated by dashed box, and colorscale indicates estimation from width algorithm. Plotted in blue is the point spread function of the system. **(b)** Super-localized points and locally-projected points (green crosses) from the experiment, overayed with the B-mode image of the vessel phantom (grayscale). **(c)** Conventional super-resolution image formed from the super-localized points in (a).

5.4 Results

5.4.1 Passive Acoustic Mapping

First evaluated were images of acoustic cavitation formed via PAM. The homogeneous ASA [i.e., Eq. (4.2.5)] was used to form the maps, as the experiments and simulations were in a uniform water environment.

5.4.1.1 Experimental Verification

Figure 5.14 shows the result of a validation experiment shown in Fig. 5.12 compared to the simulation. In Fig. 5.14(a), the vessel characteristics were recovered from the localizations computed from the simulated emissions of 326 bubbles. The diameter estimation tracked well with the true values well left and right of the bifurcation (1 mm to the left and 280 μm to the right), though the estimation was less accurate nearest the bifurcation. Notably, the projected points fell within the vessel region (inset), significantly below the point spread function of the system (300 μm, blue). For the experiment, 559 bubbles were isolated within the PAMs. In both the simulation and experiment, the vessel phantom centerline was reasonably well identified. As there were few, high-amplitude peaks in each image, relatively large morphological offsets were used: $h = 0.2$ for the simulation case [Fig. 5.14(a)], and $h = 0.6$ for the experimental case [Fig. 5.14(b)]. These results indicate that vessel morphology is recoverable from relatively small numbers of points for which the conventionally formed SR im-

age, (i.e., a Gaussian distribution with standard deviation $\lambda/4$ was centered at each SL peak) shown in Fig. 5.14(c), provides a comparable level of qualitative detail. The high CNR (89 dB) of the SR image is expected to persist for more realistic tissue environments, as the harmonic radiation of the bubbles from which the PAMs are formed is not subject to linear scattering of the excitation pulse. As the simulations are now validated, the performance of the algorithm on other vessel geometries was next investigated.

5.4.1.2 2D Simulations

To assess the performance of the algorithm on a vessel of continuously variable diameter—e.g., as in the case of an aneurysms[200]—a "bulb" shaped region was defined, and sources were randomly distributed therein. Figure 5.15 demonstrates the

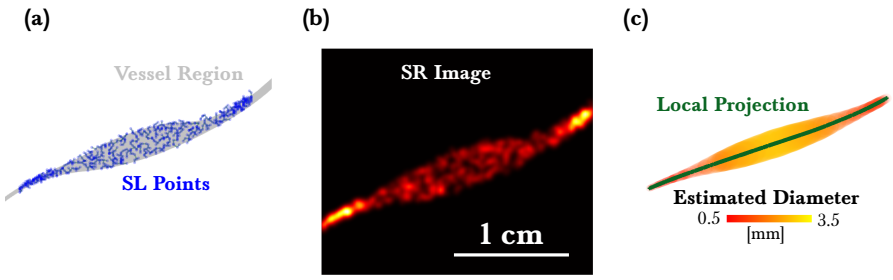

FIGURE 5.15: **(a)** From the received (simulated) bubble signals, MR identified the cloud of super-localized peaks (blue) compared with the vessel region (gray). **(b)** Local projection of the super-localized points identifies the centerline (green), as well as recovers the vessel diameter (colorscale). **(c)** Conventioally formed super-resolution image from the super-lolalized points in (a).

ability of the MR to isolate sources within a vessel and to define its shape, a vessel region was defined [gray region in Fig. 5.15(a)], and 806 bubbles were simulated within the it. Using MR with an offset of $h = 0.2$, these sources (up to 4 per frame) were super-localized. Compared to the true region, all sources were successfully localized to within tens of microns. To assess the ability of the local projection algorithm to recover the vascular structure and dimension, following beamforming and super-localization, a local projection was performed with a fixed neighborhood of $H = 5\,\mathrm{mm}$ [Fig. 5.15(b)]. Finally, Fig. 5.15(c) shows the SR images for bulb shape. While the individual localizations are still apparent in the composite images, these were formed with just a few hundred localizations, compared with the tens of thousands used in typical SR images,[15] and the contrast was very high (196 dB for the bulb).

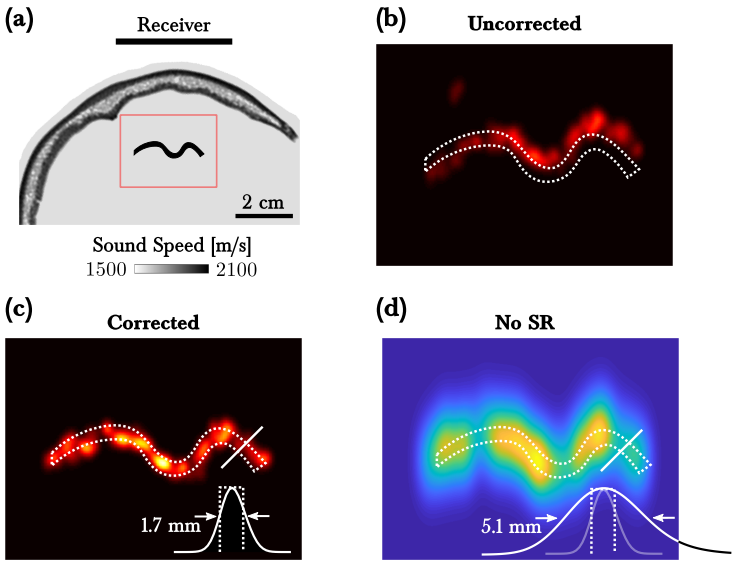

FIGURE 5.16: Super-resolved PAM for trans-skull propagation. **(a)** Position of vessel region in simulations; enlarged area in (b–c) indicated by red rectangle. **(b)** Super-resolution image of the vessel without the correction. **(c)** Super-resolution image of the vessel with the HASA correction. **(d)** Composite PAM without super-resolution.

To demonstrate the relevance to trans-skull applications, data from the vessel simulations described in Sec. 4.3.1 were compiled as in standard super-resolution imaging. Figure 5.16 demonstrates the importance of both super-resolution and the improvement in localization accuracy quantified in Chap. 4. For the transcranial vessel in which 150 sources at 1.2 MHz were simulated in a vessel region [Fig. 5.16(a)], lack of correction yields an intensity distribution [Figure 5.16(b)] that is distorted and different from the true vessel shape (dashed white line). When the correction is applied [Fig. 5.16(c)], the vessel shape and size is recovered; the size of the vessel from the indicated intensity profile was estimated at 1.7 mm, compared with the true width of 1.5 mm, and a width estimateion from the local projection algorithm (with $H = 2\,\mathrm{mm}$) of 2.1 mm. In the composite PAM [i.e., summation of each individual PAM from all 150 simulations Fig. 5.16(d)], the intensity profile at the same location had with of over 5 mm, indicating an effective improvement in resolution of 60 %. It should be emphasized here that these results were obtained with only 150 localizations, a small fraction of those used in typical demonstrations of microvessel mapping.[166]

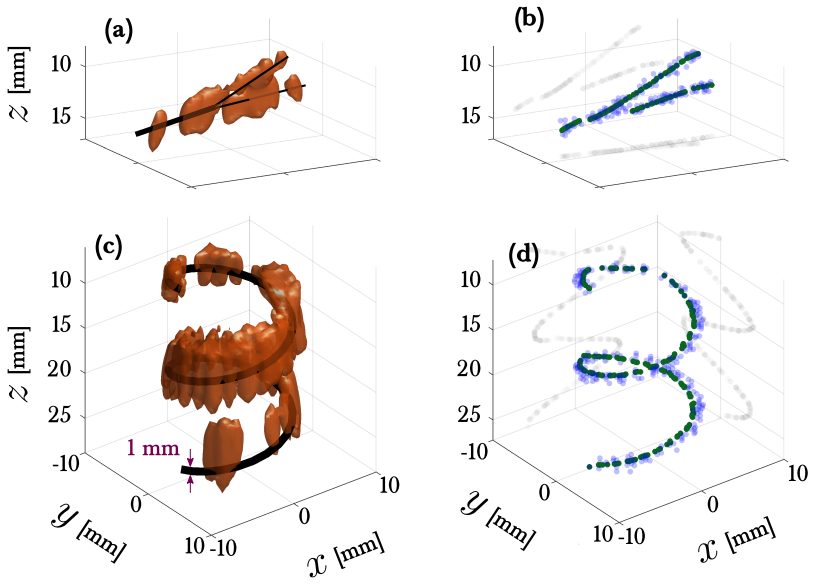

FIGURE 5.17: 3D PAM Super-resolution results. **(a)** 3 dB–volume of the simulated bifurcation phantom compared with its true location. **(b)** Super-resolved (blue) and locally projected (green) points. **(c)** 3 dB–volume of 3D PAMs for a simulated 1 mm diameter spiral. **(d)** Super-resolved (blue) and locally projected (green) points.

5.4.1.3 3D Simulations

Figure 5.17 shows the improvement imparted by the MR peak finding and subsequent local projection of passively-localized point sources from the 3D simulations. Figure 5.17(a) and (c) show the 3 dB volume obtained from a composite map formed from all localizations for the vessel bifurcation and helix-shaped region, respectively. While the general shapes of these components is somewhat recognizable, the blur of the PSF is on the order of a centimeter, rendering the resolution quite poor. However, the the super-localized peaks are projected onto their local regressions, the morphology of the shape is readily apparent. Collectively, the experimentally-validated simulation results presented in this section demonstrate that the morphological reconstruction technique for peak identification, augmented by the local projection algorithm and HASA correction, enable identification of vascular structure through the skull and below the conventional diffraction limit.

5.4.2 *Ex Ovo* Data

To examine the ability of the SR methods with smaller and denser vasculature of typical interest in active imaging methods, data from the *ex ovo* embryo model were next considered.

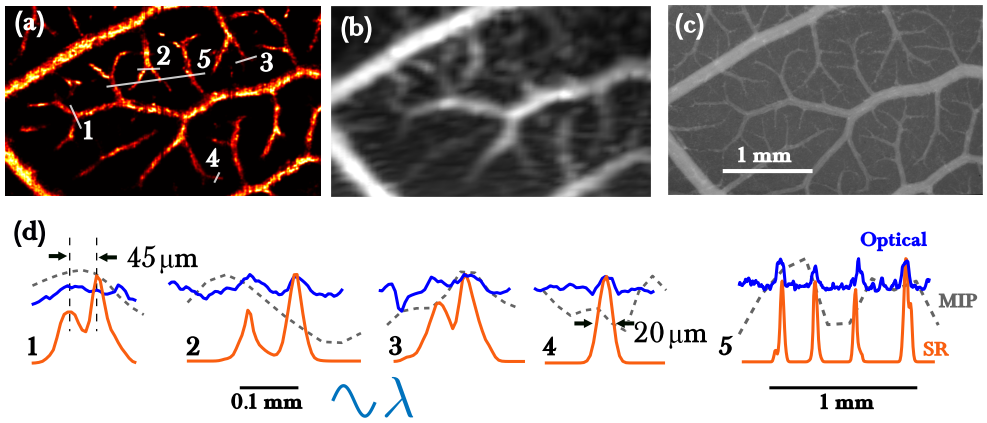

FIGURE 5.18: Comparison of imaging methods **(a)** Super-resolution image from super-localized points. **(b)** Maximum intensity projection (MIP) of the CEUS image stack **(c)** Registered optical microscopy image **(d)** Image intensity profiles for the indicated profiles in (a).

5.4.2.1 Image Quality

Figure 5.18 demonstrates the relative image quality of the SR image generated with the points localized with MR. In Fig. 5.18(a) is the SR image built from the peaks obtained via MR with h= 0.050. The image resolution is significantly better than that obtained from a maximum intensity projection of the CEUS stack [Fig. Fig. 5.18(b)] and is comparable to that of the optical image [Fig. 5.18(c)]. The intensity profiles shown in Fig. 5.18(d) for the indicated lines in Fig. 5.18(a) show that bifurcations with separations as small as 45 μm may be imaged (profile 1), and sub-vessel detail for vessels as small as 20 μm are identifiable (profile 4). These details, which are not visible in the CEUS image [gray lines in Fig. 5.18(d)], are resolved with high contrast in the SR image. Thus, the peaks identified with MR may generate SR images with resolution significantly better than that of the raw CEUS images and comparable to that of optical microscopy.

To ensure that the additional peaks detected were not spurious localizations, the contrast in the resulting SR images was evaluated (Fig. 5.19). For the smallest offset ($h = 0.025$), the CNR was lower than the contrast in the non-MR images (i.e., the image formed with only thresholded peaks), likely due to some spurious localizations contributing to background noise. However, for larger offsets ($h = 0.050$), the CNR was quite high and exceeded that of the non-MR images. This is because the MR was able to identify many more peaks in the smaller vessels, resulting in stronger signal as compared to the same positions in the non-MR images [Fig. 5.19(e)].

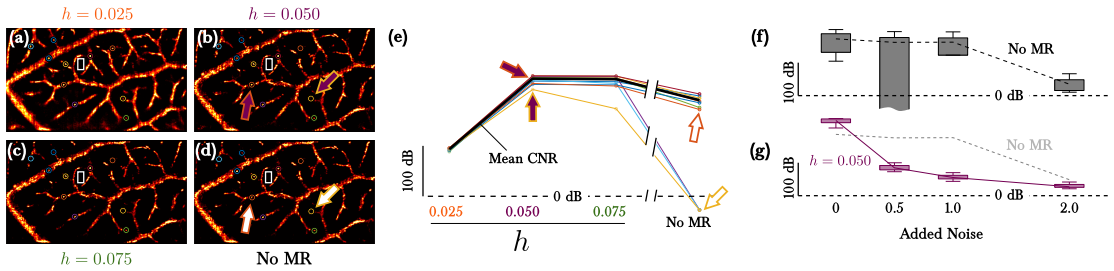

FIGURE 5.19: Super-resolution images from super-localized points with **(a)** $h = 0.025$, **(b)** $h = 0.050$, **(c)** $h = 0.075$, and **(d)** without MR (i.e., thresholded peaks) **(e)** CNRs for the for the given offset at the points (colored circles) and background region (white boxes) indicated in (a–d), compared with mean over all points (black line). CNRs of the images at the same locations formed with noise added to CEUS images prior to peak finding **(f)** Without MR, and **(g)** with $h = 0.50$.

To demonstrate the robustness of the resultant images to measurement noise, the CNR for images formed with $h = 0.05$, over the same vessel and background locations. Figure 5.19(f–g) demonstrate that while the addition of noise (resulting in a mean CNR in the maximum intensity projection of the raw image stack if 3.6±10.0 dB over the same locations) to the CEUS frames decreases the CNR of the output SR image, the contrast between vessels is consistent across all locations and remains positive [Fig. 5.19(f)]. However, without MR, some smaller vessels have poor contrast [Figure 5.19(e)], which give vanishing CNRs and subsequently wide variability in the image contrast between different size vessels.

5.4.2.2 Accuracy and Sensitivity

After demonstrating that MR can be used for peak detection in SR-US imaging framework, the robustness and accuracy of the super-localized peaks were evaluated. First, the co-registered optical microscopy mask was taken as a ground truth, and compared the super-localized peak locations obtained from the MR process. Peaks whose super-localized position lay within the vessel region (i.e., at pixels where the mask had value 1) were labeled as within the vessel (i.e. true peaks), and those with positions outside the vessel otherwise (i.e. false peaks). Figure 5.20 shows the relative positions of the super-localized points from all datasets with $h = 0.025$, compared with registered mask derived from the optical data. While the points fall largely within the vessel (as in panel 3), in locations such as panel 2 the shape created by the super-localized point cloud resembles the nearby vessel, but with a small shift in position due to imperfect registration. However, some other peaks, especially at higher sensitivities, resembled

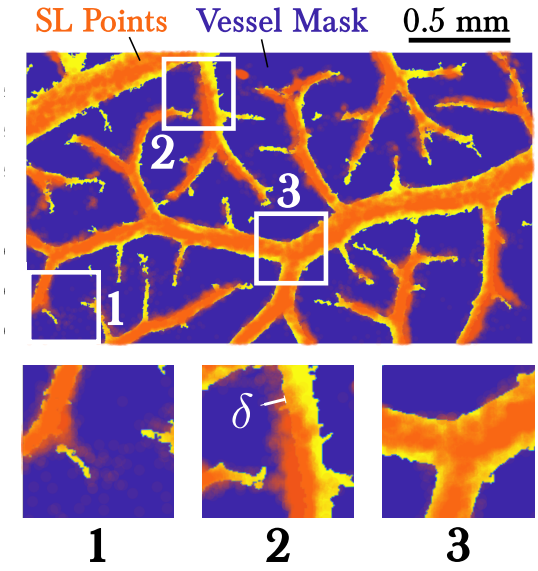

Figure 5.20: Relative position of the optically derived vascular mask, and the super-localized points with $h = 0.025$. Inset 1 shows spurious localizations outside the vasculature that likely represent noise. Inset 2 illustrates the tolerance (here $\delta = 50\,\mu\text{m}$) due to imperfect registration. Inset 3 higlights a region of good registration between the optical and SR images.

noise (as in panel 1).

To account for the imperfect registration, a tolerance δ was defined as the perpendicular distance to the vessel map, as in Fig. 5.20. Figure 5.21 demonstrates that without MR, 20.5 ± 3.4 peaks were detected in each frame, with 89.6 % located within the vessel mask. With a tolerance of $20\,\mu\text{m}$, this increases to 95.7 % were within the vessel, and if a $50\,\mu\text{m}$ tolerance is allowed, then 98.6 % were labeled as within the vessel. Thus peaks found per frame via MR were approximately two to three times as many as the case when no MR was used (i.e., simple thresholding): for an offset $h = 0.075$, 38.8 ± 4.6, for $h = 0.050$, 49.1 ± 4.8, and for $h = 0.025$, 66.2 ± 5.3.

The larger number of peaks detected due to the increased sensitivity ($h = 0.025$) came at the cost of slightly lower accuracy than the non-MR case; for instance, the $h = 0.025$ had a lower bound ($\delta = 0\,\mu\text{m}$) of 69.7 % localized within the vessel. However, given the imperfect registration, for even a small tolerance of $20\,\mu\text{m}$ labeled 86 % of these localizations is within the vessel.

The higher sensitivity offered by MR compared to thresholding is especially important in the smallest vessels—where super-resolution methods are of the greatest interest . Figure 5.22 shows the number of peaks localized from the first 720 frames (1.2 s) of data for several vessels and with different offsets h. In the smallest vessels

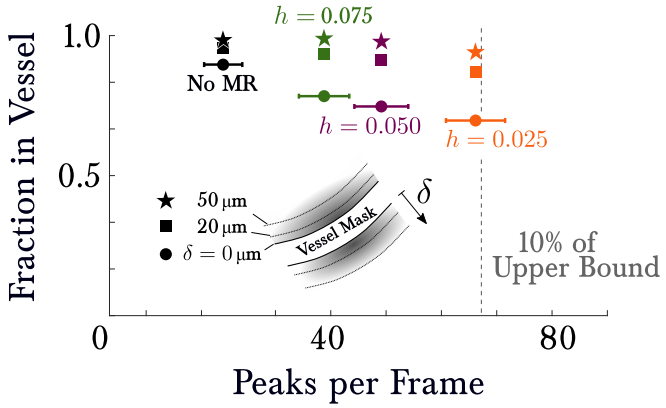

FIGURE 5.21: Mean (dot) and standard deviation (bars) of the number of peaks found per frame for the indicated offset (or without MR in black) and the corresponding accuracy (i.e., percent within the vessel mask defined from the optical data). Marker type indicates tolerance δ used to determine accuracy.

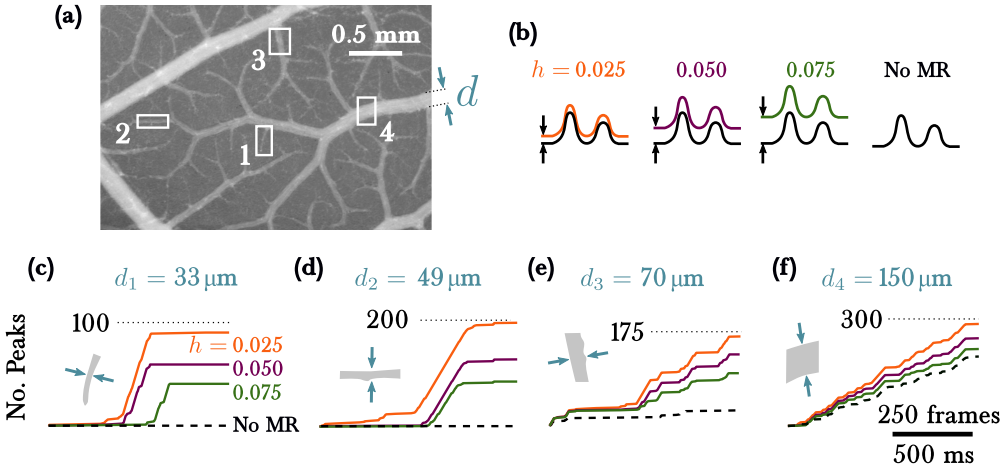

FIGURE 5.22: Peaks detected over time. **(a)** Optical microscopy image of CAM vasculature. **(b)** Illustration of morphological offsets used (not to scale), compared with the simple thresholded case. **(c)** Peaks detected as a function of time/frame number for the 33 µm diameter vessel [shape shown in gray, region 1 in (a)] and the indicated offset h. **(d)** Peaks detected for region 2, **(e)** region 3, and **(f)** region 4.

[d_1 = 33 µm, Fig. 5.22(c) and d_2 = 49 µm, Fig. 5.22(d)], no peaks were detected via thresholding (i.e., without MR). However, tens to hundreds of peaks were identified via MR, with more peaks isolated for lower offsets (higher sensitivity). For larger vessels, thresholding identified more bubbles, though still the number of localizations was significantly fewer than the number identified with MR.

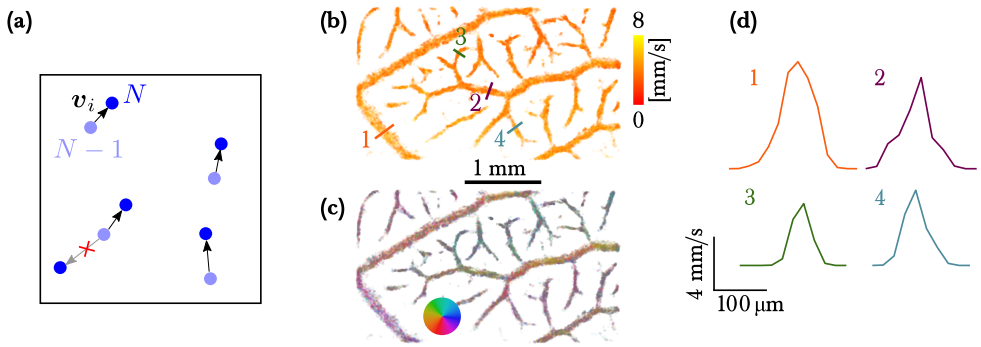

FIGURE 5.23: Velocity calculations with MR points. **(a)** Each peak in frame N is paired with the closest peak in frame $N+1$ (with the only the closest pair retained in the case of uneven numbers). **(b)** The resulting velocity magnitudes and **(c)** direction indicate recovery of reasonable values. **(d)** Flow profiles from the indicated positions in (b) demonstrate an maximum flow near the center with peak flow that trends with vessel diameter.

Velocity Estimation While estimation of flow from the super-localized points is a rich topic itself,[177,201,202] of interest here is validation that the super-localized peaks found from MR are indeed bubbles, or at least, flowing sub-wavelength scatterers[†] Figure 5.23 shows the velocity recovered from the points found via MR with the simple frame-to-frame pairing algorithm [Eq. (5.2.4)]. While ground truth is not available in the way that location data were, the magnitude of the computed velocities, around 1 cm/s, is consistent with those found via Doppler imaging and more sophisticated tracking algorithms. Additionally, the overall direction of the calculated flow [Fig. 5.23(c)] and profile across the vessels [Fig. 5.23(d)] jibe with expectations of the vessel morphology. Together, these velocity findings support that the super-localized peaks are indeed sub-wavelength acoustic scatterers that may be used to infer the shape and perfusion within the vasculature.

5.4.3 Computational Efficiency

The computation time required per frame of the MR peak finding algorithm will depend largely on the frame size, interplation, morphological offset, and specific dataset. As a test case the computation time per frame as a function of the interpolation, for a 1 mm by 1 mm region from the CAM dataset is shown in Fig. 5.24(a) (times do not include SVD filtering, which required 6.6 s for each 720 frame stack). Smaller offset cases required slightly longer processing times (e.g., 18.9 ± 4.0 ms vs 16.6 ± 2.8 ms

[†]Without, e.g., concurrent optical imaging,[189] it may only be established that the super-localized points represent scatterers smaller than the PSF. That is, the diffraction limit for a single image is undefeated.

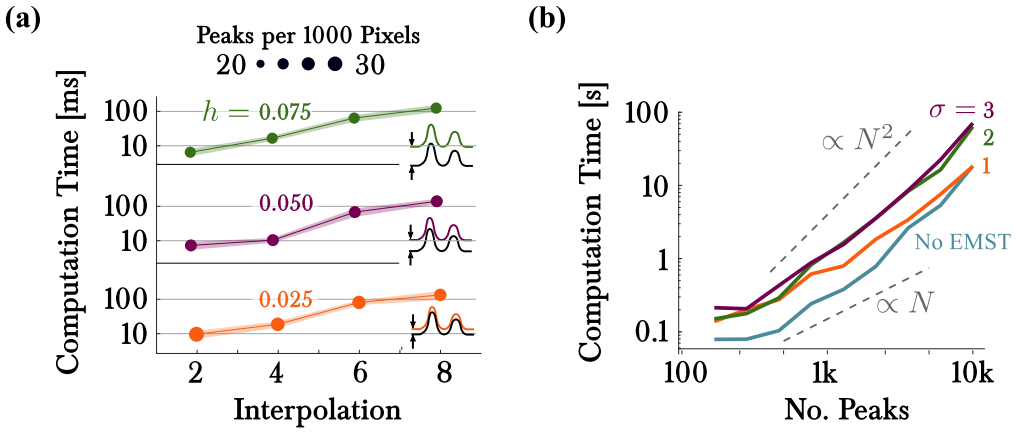

Figure 5.24: Computational Efficiency **(a)** Computation time required per frame as a function of the image interpolation for a subset of the CAM dataset for morphological offsets of $h = 0.025$, 0.050, and 0.075. The size of the markers indicates the mean number of peaks isoalted within each frame. **(b)** Computation time required for the local projection algorithm for the indicated number of randomly-generated peaks. For the blue line, no EMST was used, while for the remaining lines, the EMST with the indicated tolerance σ was used.

frame at 4× interpolation for $h = 0.025$ and $h = 0.075$, respectively) due to the larger number of points found in each frame, which increases number of correlations. Peak finding without MR required slightly less time (10.4 ± 4.0 ms per frame), but identified only 5.2 peaks per 1000 pixels over the same region, compared to 20 in the MR case. Thus, MR enables a roughly two-fold improvement in the temporal resolution (defined as the total acquisition and processing time to generate the SR image) for these data.

For the local projection algorithm, the computational time will be highly dependent on the number of peaks and their distribution. Figure 5.24(b) shows the computational time required for the indicated number of randomly distributed peaks in the naive case (i.e., without the EMST for automated segmentation) as well as cases where EMST edges longer than the indicated number of standard deviations σ were deleted. While this process proved somewhat intensive for large numbers of points (computational time grew faster than proportional to the number of points), the computational burden increased more slowly than N^2. Thus both the MR and local projection algorithms represent computationally efficient methods to supplement and improve the super-resolution imaging workflow.

5.5 Summary of Contributions

In this chapter, two novel applications of algorithms have been proposed and evaluated to improve the effective resolution of acoustic images. The first employs morphological image reconstruction, and was demonstrated to improve the peak finding sensitivity and thus enable better imaging of the smallest vessels. In PAM experiments and simulations, the resolution was improved approximately tenfold over the free-field diffraction-limited case. In conjunction with the HASA, three-fold improvement in resolution was obtained in trans-skull experiments, underscoring the utility of the method. In the case of active imaging experiments, the sensitivity was increased twofold over thresholding methods. Through velocity measurements and comparison with registered optical microscopy data, the super-localized points were confirmed to be sub-wavelength scatterers and thus useful markers for super-resolution techniques. The second method, based on a local projection of the super-localized point cloud provides automated characterization and segmentation of the musculature with reasonable computational efficiency.

Chapter 6
Nonlinear Ultrasound in the Brain

6.1 Introduction

6.1.1 Nonlinear Biomedical Ultrasound

For the first several decades of its use in biomedical applications, it was assumed that ultrasonic acoustic propagation largely obeyed linear acoustic principles.[203,204] However by the 1980s, the importance of nonlinear acoustic effects at clinically relevant pressures and frequencies became apparent.[99,205] Higher order effects absent in the linear regime include the generation of harmonics of the primary frequency,[206,207] a net force on the fluid particles (radiation pressure),[208–210] induction of fluid currents (acoustic streaming),[211,212] and generation of gas pockets within the fluid (acoustic cavitation[†]).[213,214]

Of particular interest herein is the nonlinear interaction of two sound beams with frequencies ω_1 and ω_2. Termed "scattering of sound by sound", an implication of finite amplitude propagation is the existence of sum and difference frequencies $\omega_\pm = \omega_1 \pm \omega_2$.[215,216] Applications for coincident sound beams with slightly different frequencies—termed *parametric arrays*—were soon postulated and demonstrated for highly directional transmitting and receiving arrays, both in water[217–220] and air.[221,222] Use of these parametric array effects for biomedical applications have largely been in the interest in elastography, wherein the low-frequency acoustic emissions are used to infer tissue stiffness.[223–225]

FUS offers an attractive methodology for the localization of mechanical forces, though typically at megahertz frequency ranges, at which the underlying mechanisms of neural response are not well understood.[226,227] However, through use of the parametric array effect, it is postulated that low frequency energy may be localized at scales below its wavelength. This effect has been demonstrated with highly directional loud-

[†]Though the term is conventional in both contexts, use of "cavitation" here is distinct from the phenomena of encapsulated microbubble oscillations discussed previously.

speakers, wherein high amplitude airborne ultrasound (ca. 50 kHz) is modulated such that its difference frequency is the audible range,[228–231] and with phased arrays to create subwavelength "sound-spots".[232] Indeed, the pressure at the difference frequency is often written[218,228] in terms of the modulating envelope $E(t)$[†]

$$p_- \propto \beta\, p_0^2\, \frac{\mathrm{d}^2 E^2}{\mathrm{d}t^2}\,, \tag{6.1.1}$$

indicating that the difference frequency amplitude grows as the square of the primary signal amplitude p_0. Analogous creation of highly-localized energy at biologically relevant frequencies (a few kilohertz) with ultrasound may have significant implications for new types of therapy and imaging.

6.1.2 Inducing Nonlinear Effects

Both because nonlinear effects require large amplitudes, and because highly localized regions are of interest, focusing of the acoustic energy is essential. As discussed in Chap. 3 transcranial focusing is has been of interest for many decades,[49,50] but more recent developments have enabled corrections by applying appropriately phased time delays,[54,82] but determining these delays is fraught: it requires either invasive measurement,[55,89–91] or potentially dangerous induced cavitation.[84–87] Alternatively, these delays may be computed via modeling, though such approaches are often quite intensive computationally.[7,60,62,92,93] As shown in Chaps. 2 and 3, the HASA correction derived and evaluated in offers an efficient way to calculate these focal delays and create areas of high amplitude in which the desired nonlinear effects might become important.

In this chapter, the theory of nonlinear sound beams will be briefly reviewed, for which straightforward analytical methods for highly focused sources in complex media are elusive. Then, through experimentally validated experiments, the spatial distribution of the field at the difference frequency from focused sources is investigated. Finally, use of is applied to the transcranial problem and the resulting focal fields discussed.

[†]Note that $\cos\omega_1 t + \cos\omega_2 t = 2\cos(\omega_- t/2)\cos(\omega_+ t/2)$. Thus the summation of two harmonic signals may be thought of as a signal at the average frequency $\omega_+/2$, modulated by an envelope $E(t) = 2\cos\omega_- t/2$ at *half* the difference frequency. Then, squaring $E(t)$ in Eq. (6.1.1) yields the difference frequency component, as $2\cos^2\omega_- t/2 = 1 + \cos\omega_- t$. While Eq. (6.1.1) is valid for a piston source, the proportionality to the squared rate of change of the envelope is expected to hold for the case of a focused ultrasound transducer.

6.2 Theory and Methods

6.2.1 Nonlinear Acoustic Propagation

The standard methods of deriving the linear wave equation involve first writing the pressure, particle velocity and density of the fluid as a sum of a constant value and some perturbation, i.e.,

$$p_{\text{tot}} = p_0 + p\,, \quad \boldsymbol{u}_{\text{tot}} = \boldsymbol{u}_0 + \boldsymbol{u}\,, \text{ and } \quad \rho_{\text{tot}} = \rho_0 + \rho\,, \tag{6.2.1}$$

Then, it is assumed that these perturbations are small: $p/p_0 \ll 1$, $\rho/\rho_0 \ll 1$, and that $\boldsymbol{u}_0 = 0$ and $u/c_0 \ll 1$ (where $u = |\boldsymbol{u}|$). When these expansions are substituted into the constitutive equations, products of the small values—i.e., "second order" quantities—will occur (see Sec. B.1). In most acoustic applications, these products are safely neglected; however, as the amplitude of the field variables becomes large, retaining these second order quantities becomes necessary to describing the resulting behavior.[233]

If these terms are retained, then it can be shown that the resulting second-order wave equation is (see Sec. B.2)

$$\underbrace{\nabla^2 p - \frac{1}{c_0^2}\frac{\partial^2 p}{\partial t^2}}_{\text{Linear Terms}} = \underbrace{-\overbrace{\frac{\delta}{c_0^4}\frac{\partial^3 p}{\partial t^3}}^{\text{Loss}} - \overbrace{\frac{\beta}{\rho_0 c_0^4}\frac{\partial^2 p^2}{\partial t^2}}^{\text{Nonlinearity}}}_{\text{Second Order Terms}}, \tag{6.2.2}$$

where δ is the sound diffusivity, and β is the parameter of nonlinearity. Equation (6.2.2) is often termed the "Westervelt equation", and is widely used model for nonlinear propagation and accounts for for thermoviscous and finite amplitude effects. The right hand side of Eq. (6.2.2) may be viewed as a source term for the linear propagation. Typically, solutions to Eq. (6.2.2) are difficult to obtain, so most analytical approaches employ approximation techniques.

6.2.1.1 Parametric Array

The publication[217] in which his eponymous equation [Eq. (6.2.2)] was derived, Westervelt principally considered the resulting field when two collimated, coaxial[†] plane

[†]While the existence of the difference frequency within a sound beam is well-established, the case of the interaction between two sound beams proved far more controversial.[234]

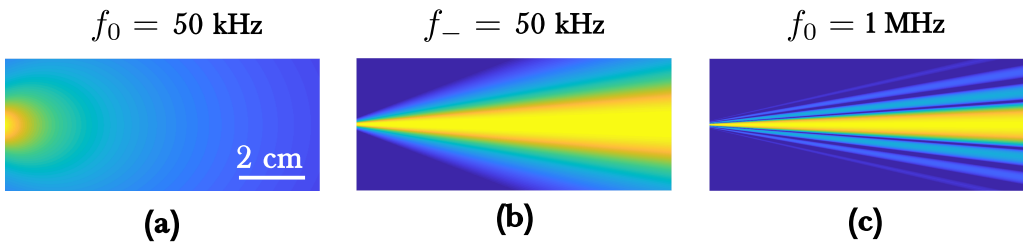

FIGURE 6.1: Field distribution for a collimated plane wave source in water with $f_0 = 1\,\mathrm{MHz}$, $f_- = 50\,\mathrm{kHz}$ and characteristic beam size $a = 12.5\,\mathrm{mm}$. **(a)** Radiating at 50 kHz, a source of this size is nearly omnidirectional. **(b)** If the frequency is achieved as a difference frequency via modulation of the 1 MHz primary, the directionality is much higher. **(c)** Directionality of the 1 MHz primary is highest, but incurs side lobes. Computed from Eq. (2) of Ref. 235.

waves traveling in the x-direction with high amplitudes and similar frequencies were generated, i.e., the incident pressure is

$$p_i = p_0 \left[e^{i(k_1 x - \omega_1 t)} + e^{i(k_2 x - \omega_2 t)} \right] e^{-\alpha x} \,. \tag{6.2.3}$$

With this as the source term, he then showed that the far field pressure at the difference frequency ω_- is

$$p_- = p_0^2 \frac{e^{ik_- r}}{r} \frac{\beta (k_- a)^2}{8 \rho_0 c_0^2} \left(\frac{1}{i\alpha_- + k_- \sin^2 \theta/2} \right) , \tag{6.2.4}$$

where α_- is the attenuation at the difference frequency. Thus the pressure radiated at ω_- due to the nonlinear interaction appears like modified spherical wave at the difference frequency: the amplitude depends on the nonlinearity of the medium β, as well as the size of the aperture relative to the difference wavelength $k_- a$. The final term in parentheses in Eq. (6.2.4) imparts a directivity that depends both on the difference frequency ω_-, as well as the attenuation in the medium.

It is important to note that the source of the difference frequency is not the radiating source, but rather the sound waves themselves—hence the term "scattering of sound by sound". The interaction of the waves gives rise to second-order content at linear combinations of the harmonics in the source signal. The term "parametric array" is somewhat misleading; the initial conception involved a linear array radiating parallel to the line ($\theta = 90°$, or "end-fire"). For the purposes of this chapter, the source comprises a single, focused transducer or phased array radiating in the perpendicu-

lar (z) direction as before; the "array" in this case is the interaction region, i.e., the near-field of the collimated beams.

6.2.1.2 Focused Parametric Sources

Analysis of the difference frequency field when source pressures are nonplanar (e.g., when the field is shaded or focused) is significantly more involved than in the case of planar waves. As in many applications of mathematical physics, insight us usually gained through special cases and approximations. Reference 236 derives an expression for on-axis and radial fields near the focal plane for $ka \gg 1$ (where k is the wavenumber of the primary frequency and a is the characteristic source dimension) and $F\#$ greater than 1.4. Using the paraxial approximation for a focused source with focal distance z_0, they show that the on axis field may be written

$$q_-(z) = -\frac{\beta k_1 k_2 u_0^2}{2c_0} \int_0^z \int_0^a \int_0^a \frac{xy}{zz'} J_0\left(\frac{k_1 k_2 xy}{k_-}\left[\frac{1}{z'} - \frac{1}{z}\right]\right) \times e^{ik_1 x^2 \bar{z}/2}\, e^{ik_2 y^2 \bar{z}/2} \exp\left[\frac{-ik_1 k_2 (x^2+y^2)}{2k_-}\left(\frac{1}{z'} - \frac{1}{z}\right)\right] \mathrm{d}x\, \mathrm{d}y\, \mathrm{d}z', \quad (6.2.5)$$

where $\bar{z} = (z^{-1} - z_0^{-1})$. The pressure field is recovered from the velocity potential, $\phi(z) = q_-(z)e^{ik_- z}$. Then, noting that the field is symmetric about $r = 0$, a the field near the focal plane ($z/z_0 \approx 1$) may be approximated

$$q(z,r) \simeq q(z,0) + \frac{r^2}{2}\frac{\partial^2 q}{\partial r^2}\bigg|_{r=0} + \ldots, \quad (6.2.6)$$

allowing an estimation of the beamwidth.

Figure 6.2 plots the predicted fields at several difference frequencies f_-, for a primary frequency of $f_0 = 1\,\mathrm{MHz}$. Plotted for reference are the expected axial fields from the same transducer for primary radiation at $f_0 = 1\,\mathrm{MHz}$ and $f_0 = 200\,\mathrm{kHz}$. As expected, the energy is significantly more spatially consolidated at the difference frequeny. For instance, the beamwidth for primary radiation at 200 kHz is on the order of 5 cm, whereas if the 200 kHz field is generated by a combination of $f_1 = 1.1\,\mathrm{MHz}$ and $f_2 = 0.9\,\mathrm{MHz}$, then the beamwidth at the focus is on the oder of 8 mm.

Thus, while theoretical developments have addressed the problem of parametric excitation (i.e., the generation of low frequency fields with much higher primary frequencies) for weakly focused sources in homogeneous media, the problem of clinical relevance involves the highly heterogeneous acoustic domain presented by the skull, as

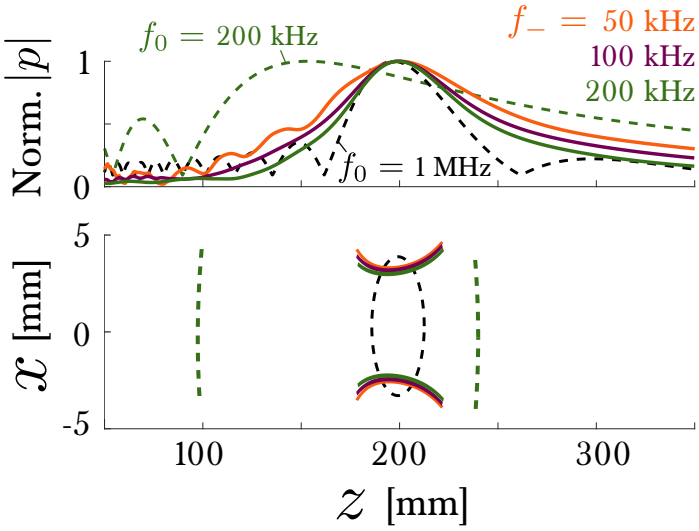

Figure 6.2: Top: Comparison of theoretical normalized axial fields for a circular focused transducer with center frequency $f_0 = 1\,\mathrm{MHz}$ at the indicated difference frequency. Computed from Eq. (6.2.5). Transducer size was $a = 5\,\mathrm{cm}$ with focal distance 20 cm. Bottom: 3 dB widths for the difference frequency, compared with approximate focal spot sizes in the linear case.

well as $F\#$on the order of unity. To address more completely the problem of nonlinear effects in the brain, simulation and experimental studies are a necessity.

6.2.2 Experimental Setup

To verify that nonlinear effects could be achieved, mapped, focused ultrasound transducers were used: one custom-built, center frequency 1.73 MHz, $F\#4/3$, focal distance 4 cm; one Olympus (Waltham, MA, USA), 1 MHz, $F\#10/9$. These transducers were connected to an arbitrary waveform generator (Keysight, Santa Rosa, CA, USA) and windowed pulses comprising a single or two superimposed frequencies were applied. The signals were amplified by a 50 dB amplifier (Electronics & Innovation, Rochester, NY, USA).

Signals from the transducers were measured by a needle hydrophone (Onda, Sunnyvale, CA, USA) whose output was read recorded by a digital oscilloscope (Pico Technologies, St Neots, UK). Strictly, the difference frequencies of interest fell outside the hydrophone bandwidth (1–20 MHz). However, the expected spectral content was apparent in the measured waveforms (and at theoretically expected levels), and thus it was estimated that the sensitivity at these frequencies was within several decibels of the stated bandwidth (–272 dB re 1 V/µPa). The hydrophone was attached to a 3D positioning system (Velmex, Bloomfield, NY USA) to enable scanning of the

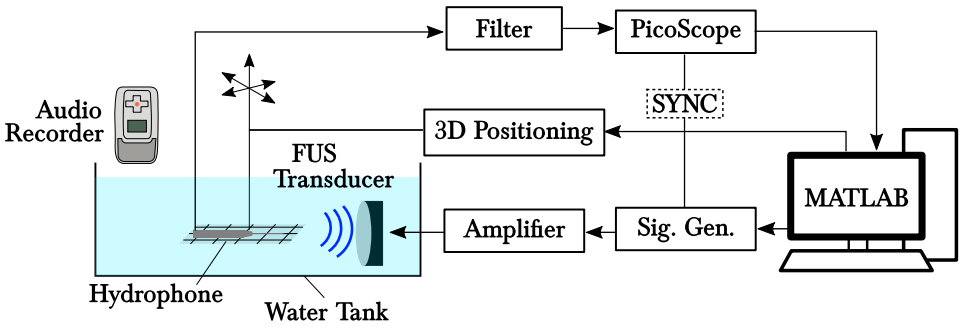

FIGURE 6.3: Experimental setup for measurement of the level and distribution of primary and difference frequency fields.

field and submerged in a tank of degassed water. Because the difference frequencies of interest were expected to have levels tens of decibels below those of the primary frequencies, the hydrophone signal was passed through a programmable analog filter (Krohn-Hite, Brockton, MA, USA) with 40 dB amplification. To record any audible generation of sonic difference frequencies, a digital audio recorder (Zoom, Tokyo, Japan) was positioned above the water surface, approximately above the hydrophone. The experimental setup is shown in Fig. 6.3.

6.2.3 Nonlinear Simulations

Evaluation of the proposed fast focal aberration technique and its ability to induce parametric array effects in trans-skull contexts is most flexible with simulations, as the geometry, material parameters, amplitudes, and frequencies may be varied arbitrarily. However, inclusion of these higher-order effects incurs additional computational expense that is often significant; indeed much of the analytical work in the field is toward simplifying aspects of the numerical implementation.[204]

Many applications of interest are concerned with sound beams (such as those considered in Sec. 6.2.1.2), such that consideration may be restricted to the near-axis field (i.e., paraxial approximation). In such cases, simplifications enable the governing equation to be rewritten in a more tractable form; perhaps the most widely used is

the KZK† equation[238,239]

$$\frac{\partial^2 p}{\partial z \partial \tau} = \frac{c_0}{2}\nabla_\perp^2 p + \frac{\delta}{2c_0^2}\frac{\partial^3 p}{\partial \tau^3} + \frac{\partial^2 p^2}{\partial \tau^2} \tag{6.2.7}$$

where $\nabla_\perp^2 = \partial^2/\partial x^2 + \partial^2/\partial y^2$ and $\tau = t - z/c_0$. Equation (6.2.7) accounts for diffraction and absorption for large amplitude sound beams, and time-domain,[240,241] frequency-domain,[24,242] and combined[243,244] approaches have been proposed for its evaluation. However, the built-in assumptions (e.g., the high directionality of the waves and the assumption of a uniform medium) necessitate more general—if more computationally expensive—methods.[204]

More general finite difference time domain (FDTD) implementations of Eq. (6.2.2) offer full accounting of propagation,[245] though as discussed previously, this is at the cost of high computational expense. Very efficient forward frequency-domain methods[36,246] are of considerable interest for modeling propagation in tissue, however such techniques do not account for reflections and require relatively weak heterogeneity. Pseudo-spectral (or "k-space") methods,[23] which were employed in previous chapters for linear acoustic propagation may be extended to account for acoustic nonlinearity. The inclusion of nonlinear effects and heterogeneity into the discrete equations is relatively straightforward, e.g., the lossless discrete pressure-density relation is[101]

$$p^{n+1} = c_0^2 \left[\rho^{n+1} + \frac{B}{2A}\frac{1}{\rho_0}\left(\rho^{n+1}\right)^2 \right] \tag{6.2.8}$$

where $\rho^n = \rho(\boldsymbol{r}, n\Delta t)$, and thus Eq. (6.2.2) may be solved with the same techniques as were used for heterogeneous media. Additionally, the fractional Laplacian operator $(\nabla^2)^{y/2}$, which is used to model power law absorption, benefits from the exceptionally convenient generalization[247] of the derivative theorem (see p. 102)

$$\mathcal{F}_k \left[(-\nabla^2)^{y/2} \rho \right] = k^y \mathcal{F}_k \left[\rho \right] . \tag{6.2.9}$$

The simulation framework has demonstrated good agreement with more specialized approaches, as well as with analytical results[101] and experimental measurements.[248] This method of calculation enables efficient (2D simulations on the order of a few minutes) prediction of finite amplitude acoustic fields through the skull. Material properties were assigned in the simulations as described in previous chapters (see Sec. 3.2.3),

†Named for its credited originators Khokhlov & Zabolotskaya, Kuznetsov. As noted in Ref. 237, the history of this form is as rich as perhaps any named equation, but by convention this name is used herein.

however a nonlinearity parameter must also be specified for each position. A thresholding was used to segment the environment into tissue types, and the nonlinearity parameter β was defined[†] for each according to[249]

$$\beta(\boldsymbol{r}) = \begin{cases} 3.55 & c(\boldsymbol{r}) \leq 1540\,\mathrm{m/s} \\ 4.45 & c(\boldsymbol{r}) \in (1540, 1700]\ \mathrm{m/s} \\ 0 & c(\boldsymbol{r}) > 1700\,\mathrm{m/s} \end{cases} . \tag{6.2.10}$$

While acoustic nonlinearity is not well-characterized for bone, the requirement of distance for the generation of nonlinear effects, as well as the high attenuation of skull bone, suggests that neglecting the nonlinearity within the skull itself is a reasonable approximation.[250] Finally, while results presented will be normalized, the source pressure in the simulations was set to be 500 kPa unless otherwise noted.

For the trans-skull focusing discussed in Chap. 3, the delays were computed for a single frequency (the center frequency of the pulse) via Eq. (3.2.5). In the case of a bi-frequency excitation (from which the difference frequency will be generated) these delays must be calculated for each component. Thus the excitation time series $s_i(t)$ for the i^{th} transducer element is

$$s_i(t) = \frac{1}{2} w(t) \left[A_{1,i} \cos \omega_1 (t - \tau_{1,i}) + A_{2,i} \cos \omega_2 (t - \tau_{2,i}) \right] \tag{6.2.11}$$

where $w(t)$ is a window function (in this case a Hamming function with width equal to 100 periods at the fundamental frequency and 10 % taper). The delays $\tau_{n,i}$ and amplitudes $A_{n,i}$ are computed from the HASA field computed at the transducer face for a delta function at the desired focus n^{th} frequency. Note that this computation now must be done twice: once for each component frequency. In the uncorrected case, the conventional geometric delays $\tau = \mathscr{L}_i / c_0$ were used.

Finally, since the field levels at relevant frequencies was of interest, the full pressure time series needed to be recorded as a function of space. Given comparatively long pulses needed, especially for larger downshift ratios (f_0/f_-) the simulated time series pressure was saved over a 30 mm-by-30 mm grid with 1 mm spacing. The level at a particular frequency was then defined as the amplitude of the spectrum of the time series at that point at that frequency.

[†]In k-Wave, B/A must be specified, thus this field was assigned as $B/A = 2(\beta - 1)$.

Trade-off of Scales One final compromise merits mentioning here, one that is practical (rather than a physical) and that affects both experimental simulated results in distinct but related ways. The downshift ratio (f_0/f_-) characterizes the difference in scale of the primary emitted frequencies, and the expected difference frequency generated by the nonlinear interactions. Nominally, very low relative frequencies are desired (i.e., $f_0/f_- \gg 1$) such that the high spatial specificity of the primary can be exploited. In the experimental case, this necessitates very long pulse lengths, as N cycles at f_- requires $N(f_0/f_-)$ cycles at the primary frequency. To avoid damage to the PZT transducer crystal due to heating, duty cycles (that is the ratio of on-time to off-time during pulsed excitations) are usually kept to around 1 %. Thus, experiments with long pulses require correspondingly small pulse repetition frequencies, and thus experimental times are lengthened substantially.

In the case of simulations, the grid must be chosen to support the shortest wavelengths due to f_1 and f_2, and potentially harmonics thereof. However, very large downshift ratios require the simulation to run for times long enough to capture the low-frequency energy. Thus the simulations require significantly more time to run; for instance, a single difference frequency simulation of the type whose trends are reported in Sec. 6.3.3 required approximately 2 hours, even with a relatively high performance workstation (14 cores at 2.2 GHz, 64 GB memory). Thus the simulations and experiments reported in this chapter were designed to balance the interest in low frequency generation and the required durations.

6.3 Results

6.3.1 Experimental Generation of Nonlinear Effects

Figure 6.4 illustrates the measured difference frequency levels and characteristics for various excitation amplitudes for a downshift ratio of 10. The amplitude increased as the applied voltage increased, but not in a linear fashion—as the unamplified signal generator voltage was increased from 150 mV to 200 mV [green and blue traces in Fig. 6.4(a), respectively], the peak to peak pressure increased by only 200 kPa, compared with nearly 500 kPa for the increases from 50 mV to 100 mV (orange and purple, respectively). This is likely due to generation of harmonics, as the distortion in the waveforms [Fig. 6.4(b)] is evident as the excitation amplitude becomes larger.

This change in the waveform shape may be correlated with spectra at the focal point, shown for each applied voltage in Fig. 6.4(c). While the primary frequency components f_1 and f_2 are prominent at all levels, the difference frequency, as well

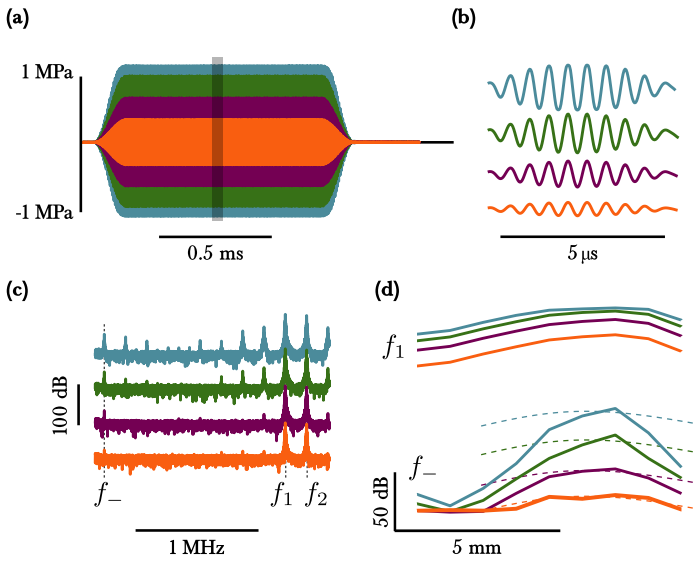

FIGURE 6.4: Waveforms measured with center frequency 1.73 MHz and downshift ratio of 10. **(a)** Time series waveforms measured at the focal point for various input excitations (50, 100, 150, and 200 mV peak-to-peak). **(b)** Enlarged shaded section from (a) for each excitation level. **(c)** Spectra for each excitation level. **(d)** Axial profiles of the level at the primary (f_1) and difference (f_-) frequencies. Colored dashed lines represent the theoretical normalized profile computed as described in Sec. 6.2.1.2.

as harmonics and other combinations of overtones, become more prevalent at higher amplitudes. The conversion of energy into these other frequencies alters the shape of the times series waveform. Considering the level of the difference frequency compared with the primary, Fig. 6.4(d) indicates that higher levels are achieved at the difference frequency for higher amplitudes at the primary. Interestingly, the focal spots are more confined than predicted by the methods described in Sec. 6.2.1.2 (dashed lines) although they are of lower level (–80 dB re primary vs –60 dB). This may be partly due to the reduced sensitivity of the hydrophone element at these lower frequencies (sensitivity only reported down to 1 MHz), and also due to the fact that the $F\#$of the transducer was smaller than the theory strictly allows.

Further confirmation of nonlinear acoustic effect generation was given by analysis of audio recorder measurements taken as in Fig. 6.3. Figure 6.5 shows the recorded audio spectra measured above the tank. The difference frequency was varied between 5 kHz and 20 kHz, as well as with varying pulse repetition frequencies to ensure that the audio was indeed due to the nonlinear interaction and not other audible sounds in

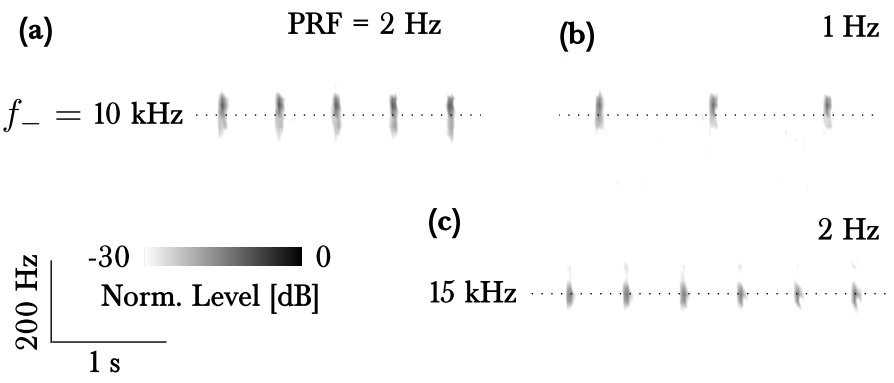

FIGURE 6.5: Spectrograms measured by the digital recorder shown in Fig. 6.3, with $f_0 = 1\,\mathrm{MHz}$. **(a)** Normalized spectrogram for $f_- = 10\,\mathrm{kHz}$ with 2 Hz pulse repetition frequency. **(b)** Normalized spectrogram for $f_- = 10\,\mathrm{kHz}$ with PRF 1 Hz. **(c)** Normalized spectrogram for $f_- = 15\,\mathrm{kHz}$ with PRF 2 Hz.

the lab space.[†] Indeed, the recorded spectrogram confirms that the generated audio frequencies are due to radiation with the 1 MHz transducer. An order of magnitude estimation of the audible level (15 dB) suggests the pressure amplitude in the air was $p_0 = 20\,\mu\mathrm{Pa} \cdot 10^{L/20} \sim 110\,\mathrm{mPa}$. The water-air interface has a normal incidence plane wave transmission coefficient $T \approx 5 \times 10^{-4}$, thus the level of this component in the water was on the order of $L \approx 20 \log_{10}(p_0/T)/1\,\mu\mathrm{Pa} \sim 165\,\mathrm{dB\,re\,1\,\mu Pa}$. The level in the tank at the difference frequency is thus substantial, even well outside the focal region.

6.3.2 Experimental Verification

To ensure that conclusions reached through the simulation study were reasonable, experimental measurement of the difference frequency field was made for downshift ratios of 10 and 20 and compared with k-Wave simulations of the same setup. Figure 6.6 shows the simulated and measured magnitude of the difference frequency field. It was noted that the phase of the received signal was highly variable, and thus the amplitude of the averaged signals were smaller (likely due to residual vibration of the positioning system following the small translations between positions). This is exacerbated by the fact that the transducer element had size (4 mm) on the same order as the acoustic wavelength (1.5 mm at 1 MHz) To address this, both the signal and magnitude of

[†]The audio recorder was a later addition after the sound was noticed to coincide with the signal generator trigger.

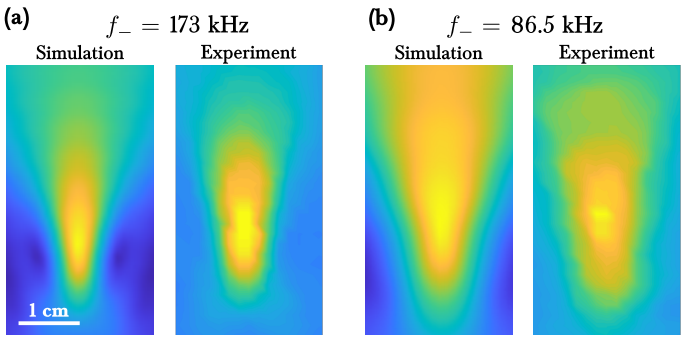

FIGURE 6.6: Normalized simulated and measured difference frequency field distributions for **(a)** $f_- = 173\,\mathrm{kHz}$ and **(b)** $f_- = 86.5\,\mathrm{kHz}$. Center frequency was that of the transducer $f_0 = 1.73\,\mathrm{MHz}$. Dynamic range is 18 dB in all cases.

its FFT were averaged 16 times at each point. Additionally, inclusion of a strong (40 dB) low-pass filter with the programmable analog device enabled improved spatial resolution of the difference frequency field.

The averaged magnitude at the difference frequency is plotted in Fig. 6.6. The agreement between the simulated and measured data suggest that the simulations capture the relevant physics in the free-field case and give confidence that characterization of the resulting fields may be made via a systematic, *in silico* study.

6.3.3 Focal Field Characteristics

Figure 6.7 demonstrates the difference between the fields achieved with a highly focused source when radiating at a high frequency to generate a field at the difference frequency, and the field that would be obtained if the transducer were to radiate at the difference frequency directly (i.e., the linear case). As the the difference frequency approaches the primary frequency (as $f_0/f_- \to 1$), the fields begin to coincide. Just as in the linear case, the trade-off between frequency and spatial extent endures: the confinement of the difference frequency energy is improved at smaller downshift ratios and at higher fundamental frequencies. The nonlinearly-generated distributions (i.e., left plots of each column in Fig. 6.7 demonstrate two deviations from expected linear behavior. First, the low frequency is generated mostly near the focal spot by the higher pressures of the focused beam, whereas in the linear case, the level of this low frequency would fall uniformly as distance from the source increases (the smaller ka results in low directivity, and thus relatively omnidirectional behavior). Second, there is a noticeable lack of sidelobes in the nonlinear case (see especially results to

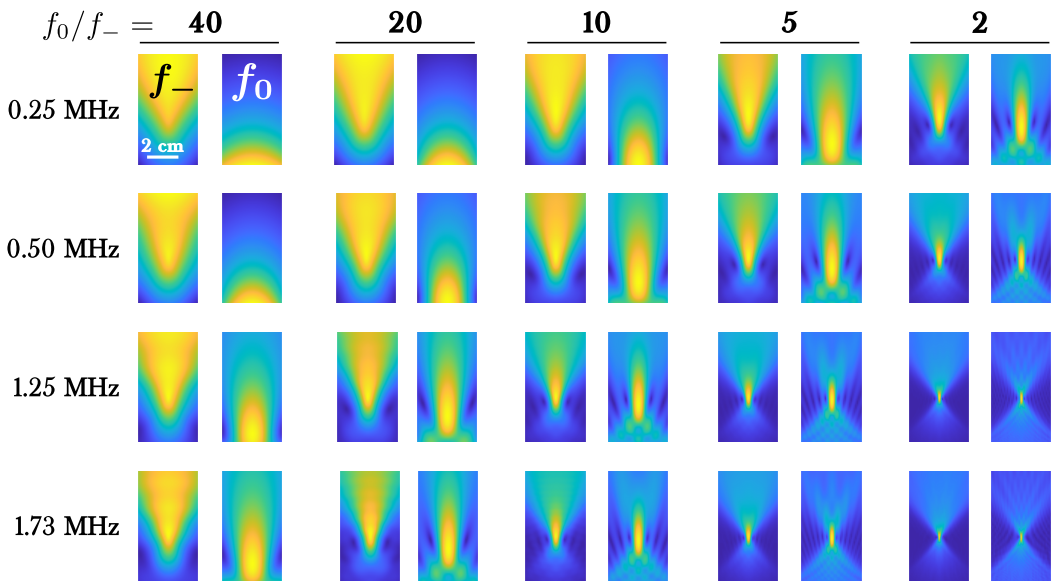

FIGURE 6.7: Simulated focal fields with $F\#0.71$ transducer, for the indicated center frequencies (rows) and downshift ratios (columns). The f_- of each column indicates the field radiated at the difference frequency for generated with the center frequency of that row; the f_0 column is the distribution expected for the transducer of the same size radiating at difference frequency.

top right of grid), a result that is consistent with the unforcused parametric beam case.[204,221] To quantify the spatial characteristics of the field, the beam width and focal area were considered next. Figure 6.8(a) shows simulated results for the difference frequency field beam widths for various primary frequencies as a function of the difference frequency f_-. The insets show comparison with the field that results from the same transducer radiating with f_- as the primary (dashed lines). Just as in the linear case, smaller downshift ratios (i.e., larger difference frequencies) give rise to narrower beams. While the beams were indeed narrowest at larger difference frequencies (i.e., smaller downshift ratios), the *relative* reduction in beam width is more pronounced for lower difference frequencies [see, e.g., 500 kHz inset for $f_-/f_0 = 0.1$ in Fig. 6.8(a)].

Similar effects were seen for the resultant focal areas (i.e., region in which the level the difference frequency was within 3 dB of the peak level) as well; see Fig. 6.8(b). Smaller focal areas were observed at smaller downshift ratios (i.e., higher difference frequencies). As was seen in Fig. 6.7, the confinement at lower difference frequencies (higher downshift ratios) was less (note that for downshift ratios of 10 and 20 for the 500 kHz case and 20 for the 1.25 MHz case were not closed over the measurement domain), but had maxima shifted away from the transducer.

The absolute width of the beam at the difference frequency is decreases with fre-

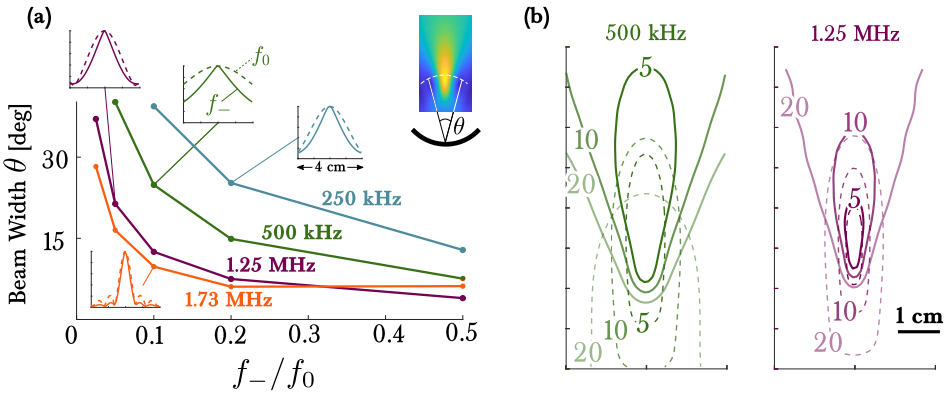

Figure 6.8: **(a)** Beam width (as measured relative to transducer face, see upper right) of simulated focal fields with $F\#0.71$ transducer, for the indicated center frequencies and downshift ratios. Insets show comparison between the difference frequency transverse profile (solid lines) and transverse profiles for the same transducer radiating at the primary frequency f_0. **(b)** Focal areas (3 dB contours) for the difference frequency with the indicated primary frequency and downshift ratio. Dashed contours indicate contours for the linear case.

quency. However, the improvement with respect to the linear case is largest at lower difference frequencies.

The $F\#$of the transducer was also seen to affect the beam width in a way comparable to the linear case, and again with marked improvement over the expected result if the tranducer were to radiate at the difference frequency directly. Figure 6.10 shows the resulting beam profiles and width for the XX MHz transducer with varying $F\#$. A fully round transducer ($F\#$= 1/2) gave the narrowest beam width 32°, which increased to approximately 44° for $F\#$= 1 [Fig. 6.10(b)]. However, the relative improvement was much more pronounced for smaller apertures [Fig. 6.10(a)].

6.3.4 Trans-skull Focal Fields

Figure 6.11 shows the simulation geometry as well as representative focal fields at the difference frequencies for a downshift ratio of 10, with a 75 mm aperture. In the corrected case, the element-specific amplitudes and delays were computed with the HASA correction at each component frequency (i.e., at $f_0 \pm f_-/2$), while in the uncorrected case, uniform amplitude and geometric delays were applied (as in Chap. 3). Quantitatively, the area of peak pressure at the difference frequency was closer to the intended focus across all positions and frequencies: 0.99 ± 0.50 mm compared to 1.24 ± 0.61 mm in the uncorrected case. The energy density at the focus (i.e., the av-

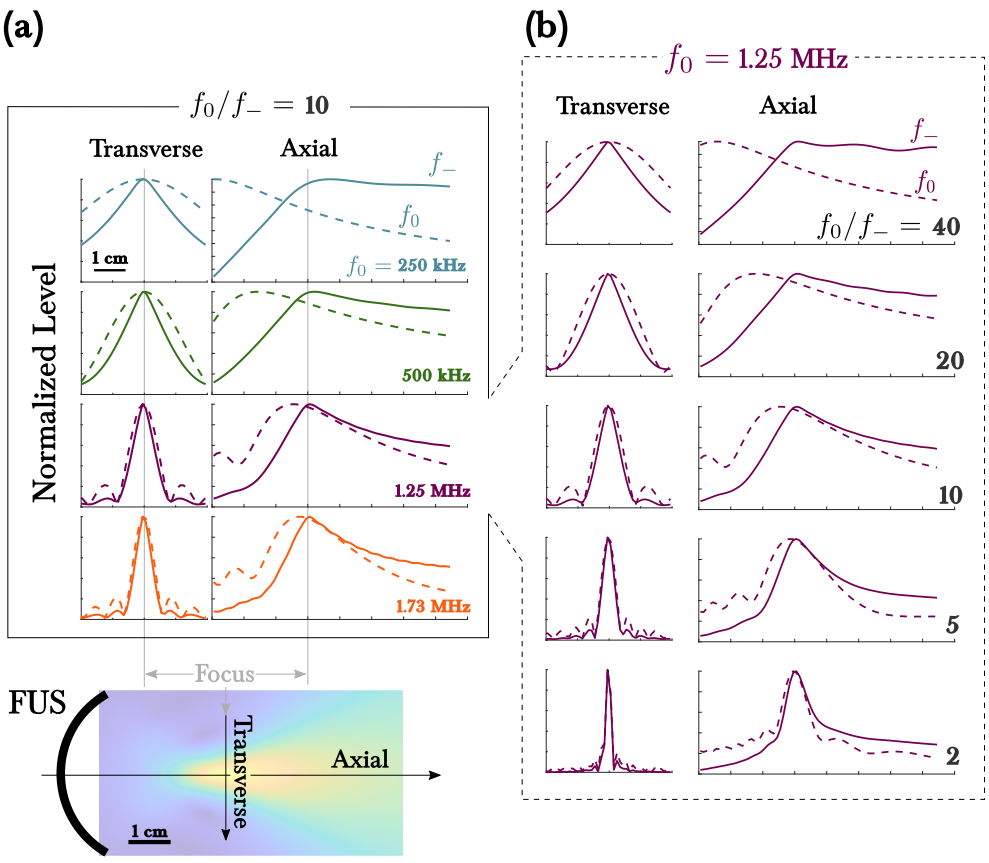

Figure 6.9: **(a)** Transverse and axial profiles of the difference frequency field for downshift ratio $f_0/f_- = 10$ for the indicated primary frequency. Dashed lines indicate the field for the same transducer radiating at the difference frequency. Gray lines indicate array focal position. **(b)** Transverse and axial profiles for the indicated downshift ration for primary frequency f_0 of 1.25 MHz.

erage level over a 1 dB region around the peak level) was 4.9 % lower in the corrected case, as well as the peak level being smaller compared to the primary frequency f_1 (–69 ± 2 dB in the corrected case vs –62 ± 3 dB in the uncorrected case). However, this partly due to the amplitude shading and choice of scaling in the corrected case (as was seen in Chap. 3).

Qualitatively, the improvement enabled the HASA was more evident. The fields in the left columns of Fig. 6.11(b) and (b) vary more uniformly and do not incur sidelobes. Additionally, the focal areas are more elongated, but more regular than the

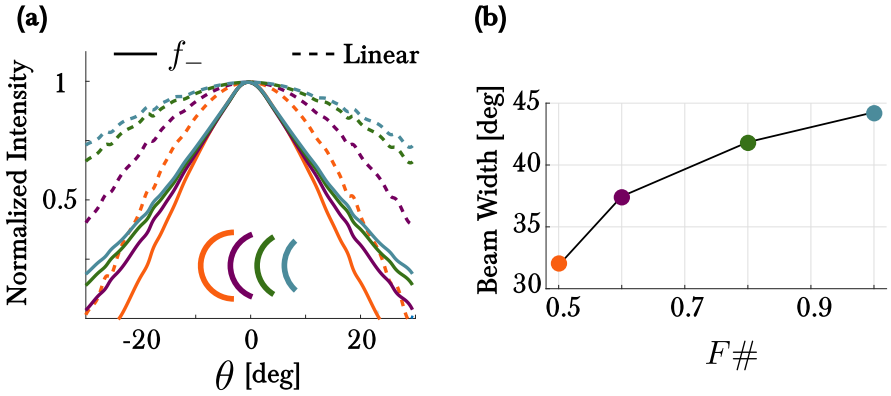

FIGURE 6.10: **(a)** Beam widths from the simulated fields with the indicated $F\#$at with the difference frequency (solid lines) compared to the same transducer radiating at the difference frequency. **(b)** Beam width as a function of the $F\#$.

uncorrected areas (eccentricity[†] 0.96±0.02 compared with 0.91±0.02 for the uncorrected case).

The level of the difference frequency was about 60 to 70 dB below that of the primary, in good agreement with analytical theory.[203] While a significantly lower, low duty cycles could ensure small enough total power delivery via thermal absorption to allow this technique to be viable.

6.4 Summary of Contributions

This chapter describes initial findings to establish the potential exploitation of nonlinear ultrasonic phenomena for applications in the brain. First, through experimentally-verified numerical simulations, the difference frequency intensity for a highly focused transducer was investigated to establish the effects of primary frequency, downshift ratio, and $F\#$. Additionally, audible sound was generated with primary frequencies above 200 kHz for the first time to the author's knowledge. Finally, the trans-skull focusing technique developed and validated in Chap. 3 was demonstrated within the simulations to improve coherence and thus facilitate the controlled, localized generation of sonic frequencies within the brain.

[†]Defined to be the ratio of the distance between the foci of the fitted ellipse to the 1 dB region to the major axis of that ellipse. Thus a circular area would have eccentricity 0, while eccentricity 1 is the asymptotic limit of a line.

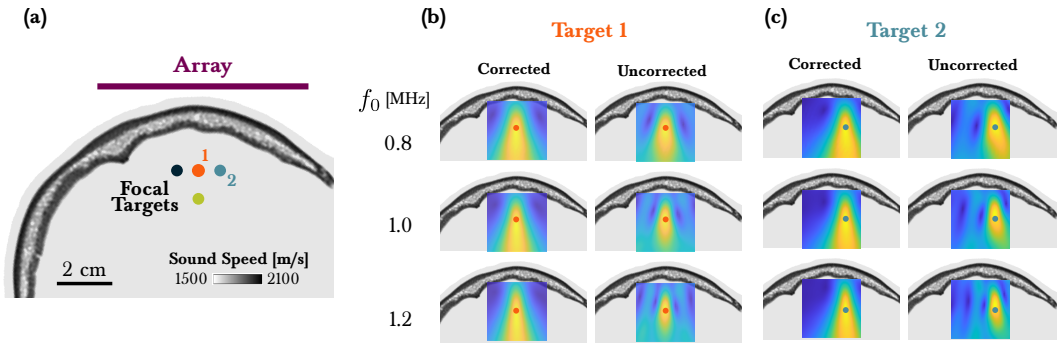

Figure 6.11: Difference frequency trans-skull fields for downshift ratio of 10. **(a)** Simulation geometry. **(b)** Normalized difference frequency fields at focal target 1 [see (a)] with (left) and without (right) the HASA correction at the indicated frequency. **(c)** Normalized difference frequency fields at focal target 1 [see (a)] with (left) and without (right) the HASA correction at the indicated frequency.

Chapter 7
Summary & Conclusion

7.1 Review of Findings

Collectively, the work described herein described an extension of the fast, frequency-domain angular spectrum approach to account for heterogeneity of the medium, and its relevance to problems in transcranial imaging and therapy. Chapter 2 derived the HASA method and discussed limits on its validity and concerns (including on a special case of a stratified medium) regarding its practical implementation. Chapter 3 described the difficulty in predicting the acoustic field on time scales relevant to clinical use, and verified that the HASA may be used to improve transcranial focusing over a range of low megahertz frequencies and focal targets centimeters beyond the skull. Further, these corrections were seen to require only a few hundred milliseconds to compute—without specialized computing hardware or techniques.

Next, HASA was applied to passive acoustic mapping through the skull in Chap. 4, which is of interest for guiding therapy, especially for cavitation activity not directly visible by MRI. Errors in source localization were reduced by more than 60 % over a range of relevant frequencies (i.e., harmonics of the frequencies of clinically-adopted FUS systems, to represent microbubble scattering) and positions. While the resolution of the images was poor compared to active imaging (both a practical and fundamental physical result), super-resolution methods based on morphological reconstruction were developed in Chap. 5. These methods were validated experimentally and through simulations, and through the latter were seen to enable a improvement in trans-skull PAM accuracy and resolution (identified features down to sub-millimeter level for a system PSF of half a centimeter). With high-frequency, active imaging data, these methods were demonstrated to enable improved sensitivity in detection of microbubble echoes (up to 10 % of the theoretical maximum), with little degradation in accuracy.

Finally, the use of HASA for trans-cranial generation of nonlinear acoustic effects in the brain was considered. Through validated simulations, the distribution of the

difference frequency from highly focused ($F\#$less than 1) was characterized as a function of frequency, downshift ratio, and $F\#$. Then, trans-skull corrections were applied and the distribution of energy in the brain at the difference frequency was mapped.

7.2 Implications & Future Directions

7.2.1 Heterogeneous ASA

While the utility of the HASA is substantial (see especially Chaps. 3 and 4) its derivation follows from the linear wave equation, which neglects nonlinearity, mode conversion, and losses. Some work addressing these effects to the forward simulation problem has been advanced,[36,251,252] however, the challenge of reflections is still extant and non-trivial. Similarly, especially in the case of trans-skull focusing, generation of elastic waves, and their subsequent radiation into the brain tissue, may offer novel techniques for trans-skull transmission. Finally, analysis here has been for harmonic signals, as the Fourier transform yields convenient mathematics to allow solutions to be found. However, given that active imaging employs wide bandwidth pulses, transformation of the wave equation to a basis better suited for such pulses may reveal analytical efficiencies that may be exploited.

7.2.2 Trans-skull Focusing

The improvement in trans-skull focusing demonstrated in Chap. 3 were for a relatively small aperture (~50 mm) linear array. All in-human transcranial FUS performed to date[7,9] has employed large (~10 cm radius) hemispherical arrays—principally to avoid skull heating due to absorption. While linear array focusing through heterogeneous for imaging, e.g., for B-mode, may have some practical applications, therapeutic levels of through-skull ultrasound will likely necessitate these larger arrays. The HASA may still be used in this case (albeit slightly less intuitively) by computing P for a delta function over the 3D space containing all transmitters, and then evaluating its magnitude and phase at each transmitter location. Future work should validate this focusing technique for irregular arrays.

7.2.3 Passive Acoustic Mapping

While the simulation studies in Chap. 4 give compelling evidence of the techniques' utility, unequivocal demonstration will require *in vitro* and *in vivo* demonstration. While effects of aperture, pitch, and measurement noise are nominally addressed

in the simulations, the efficacy is only conclusive in practical usage. Additionally, the stratified medium used in the biomedical context is somewhat academic, as such idealized media are at best approximations. While it may see applications for atmospheric[253–255] or underwater acoustics,[256–259] wherein source localization in such stratified environments are of interest.[34] Additionally, similar

Finally, despite its inherent efficiency, few sophisiticated computational techniques were employed. For instance, parallelization of ASA calculation for each frequency bin could reduce computation time. Further, the highest spatial sampling was used for all reconstructions; depending on the desired resolution, these data could be downsampled [provided the Nyquist criterion Eq. (2.6.1) is still met]. Finally, given recent advances in GPU technology and their demonstrated use in similar applications, it stands to reason that comparable gains might be achieved for the HASA.

7.2.4 Super-resolution Imaging

Chapter 5 established and validated methods for identification of individual subwavelength scatterers and methods for characterizing the vascualture therefrom. While preliminary velocity estimations were obtained, future work with more sophisticated tracking algorithms[177,202] would extend the utility of this method. Additionally, the local projection technique enables an analytical description of the vessel center (e.g., via a spline interpolation of the projected points). This description may enable distinction between healthy and aberrant vasculature in a way that tortuosity[180] and vascular density[199] recently have been. Together with the HASA, volumetric trans-skull superresolution images may be generated, with more general correction than afforded by current methods.[19,260]

7.2.5 Nonlinear Effects

The generation of sonic frequencies with spatial specificity in the brain would have significant implications for transcranial therapy. Chapter 6 established that phased arrays may generate low frequencies in the brain with better confinement than would be possible with linear focusing. Just as in the linear case, larger apertures will further reduce this spot size, and thus investigation of larger, hemispherical arrays (as discussed in Sec. 7.2.2) is merited. Perhaps notably, stratified media also simplify the mathematics for treatments of the nonlinear problem with the KZK equation,[261] and an approach similar to the stratified ASA correction may provide efficient or adaptive focusing in that context.

The ability of ultrasound to penetrate tissue to mediate forces and convey information noninvasively makes it among the most promising known medical technologies. While the brain exists in one of the least advantageous acoustical environments, progress in the last two decades alone has been swift, and imaging and therapy of central nervous system has become a reality. It is hoped that the methods described herein will contribute to their further development and utility.

Appendices

Appendix A
Derivation of Heterogeneous ASA Results

In this Appendix, the governing equation for the heterogeneous ASA is derived from the wave equation with a spatially-varying speed of sound. Then, the Green's function for the wave equation is obtained and used to find solutions to the governing equation for cases of general heterogeneity, and that of a stratified medium.

A.1 Governing Equation

Provided the medium is weakly heterogeneous (see Appendix B.1), propagation may be described by

$$\nabla^2 p - \frac{1}{c^2(\boldsymbol{r})}\frac{\partial^2 p}{\partial t^2} = 0\,. \tag{A.1.1}$$

The sound speed may be written as the sum of a reference sound speed c_0 and a spatially-varying part $c'(\boldsymbol{r})$[33]

$$c(\boldsymbol{r}) = c_0 + c'(\boldsymbol{r}). \tag{A.1.2}$$

Because Eq. (A.1.1) is most valid for small values of c',[37] the mean value of $c(\boldsymbol{r})$ is the natural choice for the reference sound speed c_0. Defining $\mu(\boldsymbol{r}) = c_0^2/c^2(\boldsymbol{r})$ and taking the temporal Fourier transform of Eq. (B.1.1) gives

$$\left(\nabla^2 + k_0^2\right)\tilde{p} = k_0^2\,(1-\mu)\,\tilde{p}\,, \tag{A.1.3}$$

where $k_0 = \omega/c_0$. Note that for a uniform medium, then $\mu = 1$, and Eq. (A.1.3) reduces to the homogeneous Helmholtz equation as expected. Now defining an auxiliary

function $\lambda(\boldsymbol{r}) \equiv k_0^2\,(1-\mu)$, Eq. (A.1.3) may be written

$$\left(\nabla^2 + k_0^2\right)\tilde{p} = \mathcal{F}_k^{-1}\left[\Lambda * P\right], \tag{A.1.4}$$

where the convolution theorem has been used, and $\Lambda(k_x, k_y, z) = \mathcal{F}_k[\lambda(x, y, z)]$. Then, since[†]

$$\mathcal{F}_k\left[\nabla^2\tilde{p}\,\right] = \left(-k_x^2 - k_y^2 + \frac{\partial^2}{\partial z^2}\right)P, \tag{A.1.5}$$

the left hand side of Eq. (A.1.3) becomes

$$\begin{aligned}\left(\nabla^2 + k_0^2\right)\tilde{p} &= \nabla^2\tilde{p} + k_0^2\tilde{p} \\ &= \mathcal{F}_k^{-1}\left[\left(-k_x^2 - k_y^2 + \frac{\partial^2}{\partial z^2}\right)P + k_0^2 P\right] \\ &= \mathcal{F}_k^{-1}\left[\left(\underbrace{k_0^2 - k_x^2 - k_y^2}_{=k_z^2} + \frac{\partial^2}{\partial z^2}\right)P\right].\end{aligned} \tag{A.1.6}$$

Then Eqs. (A.1.4) and (A.1.6) yield Equation (2.3.1)

$$\begin{aligned}\mathcal{F}_k^{-1}\left[\frac{\partial^2 P}{\partial z^2} + k_z^2 P\right] &= \mathcal{F}_k^{-1}\left[\Lambda * P\right] \\ \implies \frac{\mathrm{d}^2 P}{\mathrm{d}z^2} + k_z^2 P &= \Lambda * P,\end{aligned} \tag{A.1.7}$$

where the derivative has become total since $\partial k_x/\partial z = \partial k_y/\partial z = 0$. Equation (A.1.7) is the governing equation to be solved for the angular spectrum P—from which the acoustic field $\tilde{p}$ may be recovered—based on the medium heterogeneity and the initial condition P_0.

[†]This is demonstrated analogously to the time differentiation theorem (see p. 4): First write $\tilde{p}(\boldsymbol{r})$ as the inverse transform of its transform $\tilde{p} = \mathcal{F}_k^{-1}[P]$. As P is not a function of x or y, only derivatives of the exponential term is required with respect to these variables; the full z derivative of the integrand will need to be taken

$$\begin{aligned}\nabla^2\tilde{p} &= \frac{1}{4\pi^2}\iint_{-\infty}^{\infty}\left(\frac{\partial^2}{\partial x^2} + \frac{\partial^2}{\partial y^2} + \frac{\partial^2}{\partial z^2}\right)\underbrace{P\,e^{i(k_x x + k_y y)}}_{\zeta}\,\mathrm{d}k_x\,\mathrm{d}k_y \\ &= \frac{1}{4\pi^2}\iint_{-\infty}^{\infty}\left[\left(i^2 k_x^2\right)\zeta + \left(i^2 k_y^2\right)\zeta + \frac{\partial^2\zeta}{\partial z^2}\right]\mathrm{d}k_x\,\mathrm{d}k_y = \frac{1}{4\pi^2}\iint_{-\infty}^{\infty}\left(-k_x^2 - k_y^2 + \frac{\partial^2}{\partial z^2}\right)\zeta\,\mathrm{d}k_x\,\mathrm{d}k_y\,.\end{aligned}$$

Taking the forward transform establishes the identity Eq. (A.1.5).

A.2 Green's Function

To begin, take $z' = 0$ for convenience. Following Watanabe,[31] the Green's function for the wave equation must satisfy by definition

$$\frac{\partial^2 g}{\partial z^2} + k_0^2 g = -\delta(z)\,. \tag{A.2.1}$$

Taking the Fourier transform of both sides gives

$$\begin{aligned} \mathcal{F}_k\left[\frac{\partial^2 g}{\partial z^2}\right] + k_0^2 G &= -1 \\ -k_z^2 G + k_0^2 G &= -1 \\ \implies G &= \frac{1}{k_z^2 - k_0^2}\,. \end{aligned} \tag{A.2.2}$$

The Green's function is then given by the inverse transform:

$$g = \mathcal{F}_k^{-1}[G] = \frac{1}{2\pi}\int_{-\infty}^{\infty} \frac{1}{k_z^2 - k_0^2}\, e^{ik_z z}\,\mathrm{d}k_z\,. \tag{A.2.3}$$

To handle the pole at $k_z = k_0 = \omega/c_0$, allow the frequency to have a small imaginary component

$$\omega = \varpi + i\epsilon\,, \quad (\epsilon \in \mathbb{R}_{>0}) \tag{A.2.4}$$

which means that the integral must now be taken over a curve $C \in \mathbb{C}$ which contains the k_z-axis:

$$g = \frac{1}{2\pi}\int_{C} \frac{1}{k_z^2 - k_0^2}\, e^{ik_z z}\,\mathrm{d}k_z\,. \tag{A.2.5}$$

Breaking the integral up into terms with positive (C^+) and negative (C^-) imaginary parts gives

$$g = \frac{1}{2\pi}\int_{C^+} \frac{1}{k_z^2 - k_0^2}\, e^{ik_z z}\,\mathrm{d}k_z + \frac{1}{2\pi}\int_{C^-} \frac{1}{k_z^2 - k_0^2}\, e^{ik_z z}\,\mathrm{d}k_z\,. \tag{A.2.6}$$

As the radius of the semicircular paths go to infinity, it must be ensured that the function vanishes so that the contribution to the integral lies only along the real axis. Then, C^+ corresponds to positive z (since $e^{ik_z z} \to 0$ is needed, and $\operatorname{Im} k_z > 0$), and

conversely C^- corresponds to negative z, see Fig. A.1.

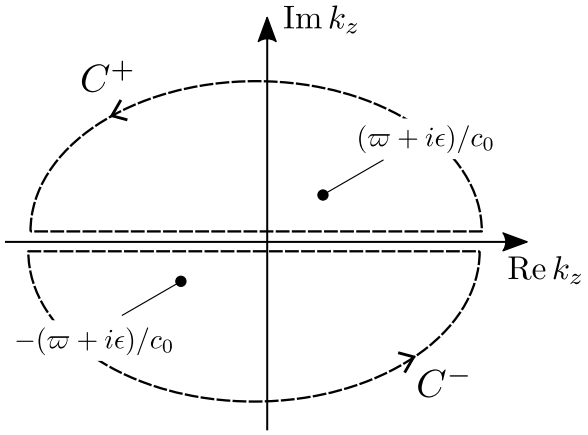

Figure A.1: Integration contours for evaluation of Eq. (A.2.6).

Conveniently, the curves each contain only a single pole and may be integrated with the Cauchy integral formula.[32] The first term in Eq. (A.2.6) may be evaluated

$$\begin{aligned}\frac{1}{2\pi}\int_{C^+}\frac{1}{k_z^2-k_0^2}\,e^{ik_z z}\,\mathrm{d}k_z &= \int_{C^+}\frac{e^{ik_z z}/(k_z+k_0)}{(k_z-k_0)}\,\mathrm{d}k_z \\ &= \frac{1}{2\pi}\,2\pi i\left[\frac{e^{ik_z z}}{(k_z+k_0)}\bigg|_{k_z=k_0}\right] \\ &= i\,\frac{e^{ik_0 z}}{2k_0} \quad (z>0)\,. \end{aligned} \tag{A.2.7}$$

The same process for the lower loop C^+ wherein $z > 0$ gives

$$\frac{1}{2\pi}\int_{C^-}\frac{4\pi}{k_z^2-k_0^2}\,e^{ik_z z}\,\mathrm{d}k_z = i\,\frac{e^{-ik_z z}}{2k_0}\,. \quad (z<0)\,. \tag{A.2.8}$$

The choice of a positive imaginary frequency was arbitrary, thus a small *negative* imaginary increment of the frequency ($\omega = \varpi - i\epsilon$) should be considered as well. The procedure follows as before, except that now convergence requires the negative loop C^- for positive z and C^+ for negative z. Then,

$$\frac{1}{2\pi}\int_{C^-}\frac{e^{ik_z z}}{k_z^2-k_0^2}\,\mathrm{d}k_z\,. = -i\,\frac{e^{-ik_z z}}{2k_0} \quad (z>0) \tag{A.2.9}$$

and

$$\frac{1}{2\pi}\int_{C^+}\frac{e^{ik_z z}}{k_z^2-k_0^2}\,\mathrm{d}k_z\,.=-i\,\frac{e^{ik_z z}}{2k_0}\,.\quad(z<0)\,. \tag{A.2.10}$$

From Eqs. (A.2.7) to (A.2.10)

$$g=\begin{cases}-\frac{e^{ik_0|z|}}{2ik_0} & \mathrm{Im}\,\omega>0\\ +\frac{e^{-ik_0|z|}}{2ik_0} & \mathrm{Im}\,\omega<0\end{cases} \tag{A.2.11}$$

(note the signs have changed, as the imaginary unit was moved to the denominator). For finite, nonzero z', terms from both imaginary frequency regimes must be included. Consideration of the time convention ($\propto -i\omega t$) dictates the terms to be chosen such that corresponds to outgoing wave propagation (rather than arriving from infinity) is specified.[31] Finally then, the Green's function for positive z is[32]

$$g=\frac{1}{2ik_z}\left(e^{ik_z|z-z'|}-e^{ik_z|z+z'|}\right)\,. \tag{A.2.12}$$

A.3 Solutions

A.3.1 General Heterogeneity: Numerical Scheme

The Green's function derived in Sec. A.2 may be used to approach Eq. (A.1.7) in a general way by treating the right hand side as a source term.[30] The homogeneous solution is

$$P_h=Ae^{ik_z z}+Be^{-ik_z z}\,, \tag{A.3.1}$$

and the appropriate Green's function $g(z\,|\,z')$ is given by Eq. (A.2.12).[31,32] Then the full solution is then given by

$$P=P_h+\int_0^\infty g(z\,|\,z')\times\Lambda * P\,\mathrm{d}z'\,. \tag{A.3.2}$$

Define the shorthand

$$\zeta\equiv\Lambda * P\,, \tag{A.3.3}$$

where the z argument of Λ and P is taken to be the integration variable z' when appearing inside the integration. To address the integration out to infinity, break up the integrals in Eq. (A.3.2) so that

$$\begin{aligned}
\int_0^\infty g(z\,|\,z') \times \Lambda * P \,\mathrm{d}z' &= \int_0^z g(z\,|\,z')\,\zeta \,\mathrm{d}z' + \int_z^\infty g(z\,|\,z')\,\zeta \,\mathrm{d}z' \\
&= \frac{1}{2ik_z} \int_0^z \left(e^{ik_z(z-z')} - e^{ik_z(z+z')} \right) \zeta \,\mathrm{d}z' \\
&\quad + \frac{1}{2ik_z} \int_z^\infty \left(e^{-ik_z(z-z')} - e^{ik_z(z+z')} \right) \zeta \,\mathrm{d}z' \\
2ik_z \int_0^\infty g(z\,|\,z') \times \Lambda * P \,\mathrm{d}z' &= \int_0^z \left(e^{ik_z(z-z')} - e^{ik_z(z+z')} \right) \zeta \,\mathrm{d}z' \\
&\quad - \int_0^z \left(e^{-ik_z(z-z')} - e^{ik_z(z+z')} \right) \zeta \,\mathrm{d}z' \\
&\quad + \int_0^\infty \left(e^{-ik_z(z-z')} - e^{ik_z(z+z')} \right) \zeta \,\mathrm{d}z' \qquad \text{(A.3.4)}
\end{aligned}$$

Note that the signs of the exponents have been adjusted to remove the absolute values. Further manipulation of Eq. (A.3.4) gives[†]

$$\begin{aligned}
2ik_z \int_0^\infty g(z\,|\,z') \times \Lambda * P \,\mathrm{d}z' &= \int_0^z \left(e^{ik_z(z-z')} - e^{-ik_z(z-z')} \right) \zeta \,\mathrm{d}z' \\
&\quad + \int_0^\infty \left(e^{-ik_z(z-z')} - e^{ik_z(z+z')} \right) \zeta \,\mathrm{d}z' \\
&= e^{ik_z z} \int_0^z e^{-ik_z z'} \zeta \,\mathrm{d}z' - e^{-ik_z z} \int_0^z e^{ik_z z'} \zeta \,\mathrm{d}z' \\
&\quad + e^{-ik_z z} \int_0^\infty e^{ik_z z'} \zeta \,\mathrm{d}z' - e^{ik_z z} \int_0^\infty e^{ik_z z'} \zeta \,\mathrm{d}z' \qquad \text{(A.3.5)}
\end{aligned}$$

Notice that the last two integrals are constant with respect to z, and thus their multiplication by $e^{\pm ik_z z}$ can be folded into the constants A and B in the homogeneous

[†]There appears to be a sign error after the third equals sign in Eq. (A2) of Ref. 30. I believe the first integral term should read (with the notation of that paper)

$$\int_0^z \left(e^{iK(z-z')} - e^{-iK(z-z')} \right) F(P(z')) \,\mathrm{d}z' \,.$$

As written (i.e., without the negative sign in the second exponent) the integral would vanish. This is apparently just an isolated typo, as subsequent results are consistent.

solution Eq. (A.3.1). Thus the solution will look like

$$P = Ae^{ik_z z} + Be^{-ik_z z} + \frac{1}{2ik_z}\left[e^{ik_z z}\int_0^z e^{-ik_z z'}\zeta\,\mathrm{d}z' - e^{-ik_z z}\int_0^z e^{ik_z z'}\zeta\,\mathrm{d}z'\right] \tag{A.3.6}$$

If it is assumed that there are no backward travelling waves, then $B = 0$, and from the boundary condition $P|_{z=0} = P_0$ at the source plane, the implicit solution is found [Eq. (2.3.2), repeated here]:

$$P = P_0 e^{ik_z z} + \frac{e^{ik_z z}}{2ik_z}\int_0^z e^{-ik_z z'}\,(\Lambda * P)\,\mathrm{d}z'\,. \tag{A.3.7}$$

The approximate marching scheme suggested by Jing et al.[251] defines the angular spectrum at some discrete axial position z_n to be

$$P^n = P(k_x, k_y, z_n)\,, \tag{A.3.8}$$

and

$$P^{n+1} = P(k_x, k_y, z_n + \Delta z). \tag{A.3.9}$$

Then, with knowledge of the initial condition $P^0 = P_0$, and approximation of the integral,

$$P^1 \simeq P^0 e^{ik_z z_1} + \frac{e^{ik_z z_1}}{2ik_z}\left[e^{-ik_z z_0}\,(\Lambda * P)\,\Delta z\right] + \mathcal{O}\left[(\Delta z)^2\right]\,. \tag{A.3.10}$$

The field may thus be approximated at arbitrary z via[262]

$$P^{n+1} \approx P^n e^{ik_z \Delta z} + \frac{e^{ik_z \Delta z}}{2ik_z}\,(P^n * \Lambda) \times \Delta z\,. \tag{A.3.11}$$

Truncation Error To ensure that higher order terms are negligible in Eq. (A.3.10), note first that

$$\int_z^{z+\Delta z} f(z')\,\mathrm{d}z' = f(z)\,\Delta z + \frac{1}{2}\frac{\partial f}{\partial z}\,(\Delta z)^2 + \ldots\,. \tag{A.3.12}$$

Thus the constant of proportionality for $(\Delta z)^2$ for the left Riemann sum is $\frac{1}{2}\partial f/\partial z$. In this case, the integrand is $f(z) = (\Lambda * P)\exp -ik_z z$, so that

$$\frac{\partial}{\partial z}\left[e^{-ik_z z}\left(\Lambda * P\right)\right] = -ik_z e^{-ik_z z}\left(\Lambda * P\right) + e^{-ik_z z}\frac{\partial}{\partial z}\left(\Lambda * P\right) . \tag{A.3.13}$$

Now differentiation of the convolution follows an analogous chain rule, since

$$\begin{aligned}\frac{\partial}{\partial z}\left(\Lambda * P\right) &= \frac{\partial}{\partial z}\left[\iint_{-\infty}^{\infty}\Lambda(k_x - k_x',\, k_y - k_y',\, z)\, P(k_x, k_y, z)\,\mathrm{d}k_x'\,\mathrm{d}k_y'\right] \\ &= \iint_{-\infty}^{\infty}\left\{\Lambda(k_x - k_x',\, k_y - k_y',\, z)\frac{\partial P}{\partial z} + P\frac{\partial}{\partial z}\left[\Lambda(k_x - k_x',\, k_y - k_y',\, z)\right]\right\}\mathrm{d}k_x'\,\mathrm{d}k_y' \\ &= \Lambda * \frac{\partial P}{\partial z} + P * \frac{\partial \Lambda}{\partial z} .\end{aligned} \tag{A.3.14}$$

Thus the largest neglected terms have magnitude bounded by

$$\begin{aligned}\frac{(\Delta z)^2}{2}\left|\frac{e^{ik_z z}}{2ik_z}\left(-ik_z e^{-ik_z z} + \Lambda * \frac{\partial P}{\partial z} + P * \frac{\partial \Lambda}{\partial z}\right)\right| &\le \frac{(\Delta z)^2}{2}\left[\frac{1}{2} + \left|\frac{e^{ik_z z}}{2ik_z}\left(\Lambda * \frac{\partial P}{\partial z} + P * \frac{\partial \Lambda}{\partial z}\right)\right|\right] \\ &\le \frac{(\Delta z)^2}{2}\left[\frac{1}{2} + \left|\frac{e^{ik_z z}}{2ik_z}\right|\left(|\Lambda| \cdot \left|\frac{\partial P}{\partial z}\right| + |P| \cdot \left|\frac{\partial \Lambda}{\partial z}\right|\right)\right] \\ &\le \frac{(\Delta z)^2}{2}\left[\frac{1}{2} + \frac{1}{2k_0}\left(|\Lambda| \cdot \left|\frac{\partial P}{\partial z}\right| + |P| \cdot \left|\frac{\partial \Lambda}{\partial z}\right|\right)\right] ,\end{aligned} \tag{A.3.15}$$

as $|e^{ik_z z}| = 1$ and $|k_z| \le |k_0|$. The first term in Eq. (A.3.15) is smaller than the first term by a factor of $\Delta z/2$, ensuring the error from this term may be made arbitrarily small with an appropriate choice of step size. The second terms are scaled by factors

$$\frac{|\partial P/\partial z|}{2|P|}\Delta z \quad \text{and} \quad \frac{|\partial \Lambda/\partial z|}{2|\Lambda|}\Delta z , \tag{A.3.16}$$

relative to the first term in the expansion, respectively. That the first term is small requires that the pressure field does not change quickly with respect to the step size. The required step Δz is the known from *a priori* knowledge of the frequency and medium (and thus wavelength). The second term describes the relative change in the medium over the step is small. Since it was already required that the scale of the sound speed change is long compared to the wavelength, then this criterion is automatically met. Thus the truncation is valid as long as $\omega\Delta z/c_{\max} \ll 1$.

A.3.2 Stratified Case: First Order Analytical Result

For stratified media, a first-order analytical solution may be obtained. If the sound speed is stratified along the axial direction z, then $\mu = \mu(z)$ and

$$\lambda(z) = k_0^2 (1 - \mu) \, . \tag{A.3.17}$$

In this case the angular spectrum of λ is $\Lambda = \lambda \, \delta(k_x) \, \delta(k_y)$, such that Eq. (2.3.1) becomes

$$\frac{\mathrm{d}^2 P}{\mathrm{d}z^2} + k_z^2 P = \lambda \, P \, . \tag{A.3.18}$$

Assume a WKB–type solution[35] of the form

$$P = A(k_x, k_y, z) \, e^{ik_z z} \, , \tag{A.3.19}$$

where A is a complex amplitude. Substitution of Eq. (A.3.19) into Eq. (A.3.18) and evaluation of the derivatives yields

$$\frac{\mathrm{d}^2 A}{\mathrm{d}z^2} + 2ik_z \frac{\mathrm{d}A}{\mathrm{d}z} - \lambda A = 0 \, . \tag{A.3.20}$$

To first order, the first term in Eq. (A.3.20) can be neglected to obtain a first-degree ODE for A, which may be integrated directly to give

$$A = A_0 \exp\left(\frac{1}{2ik_z} \int_0^z \lambda(z) \, \mathrm{d}z' \right) . \tag{A.3.21}$$

Application of the boundary condition at $z = 0$ gives

$$A = P_0 \exp\left(\frac{1}{2ik_z} \int_0^z \lambda(z') \, \mathrm{d}z' \right) , \tag{A.3.22}$$

and the angular spectrum at arbitrary z is then

$$\begin{aligned} P &= \left[P_0 \exp\left(\frac{1}{2ik_z} \int_0^z \lambda(z') \, \mathrm{d}z' \right) \right] e^{ik_z z} \\ &= P_0 \exp\left[i \left(k_z z - \frac{k_0^2}{2k_z} \int_0^z 1 - \mu(z') \, \mathrm{d}z' \right) \right] . \end{aligned} \tag{A.3.23}$$

Equation (A.3.23) represents an additional phase delay ϕ to the homogeneous medium case given by

$$\phi = \frac{k_0^2}{2k_z} \int_0^z 1 - \mu(z')\,\mathrm{d}z' \,. \tag{A.3.24}$$

Note that for a homogeneous medium, then $\mu = 1$, and the homogeneous medium case is recovered. Equation (A.3.24) may be thought of as accumulation of phase shifts incurred as the wave travels through an infinitesimal width $\mathrm{d}z$, i.e.,

$$\phi = \int \mathrm{d}\phi \quad \Longrightarrow \quad \mathrm{d}\phi = \frac{k_0^2}{2k_z}\,(1-\mu)\,\mathrm{d}z \,. \tag{A.3.25}$$

Since it was required that c'/c_0 is small, $\mu(z) \equiv (1 + c'/c_0)^{-2}$ can be expanded so that Eq. (A.3.25) becomes

$$\begin{aligned} \mathrm{d}\phi &\simeq \frac{k_0^2}{2k_z}\left[1 - \left(1 - 2\frac{c'}{c_0}\right)\right]\mathrm{d}z \\ &\simeq \frac{k_0^2}{2k_z}\left(2\frac{c'}{c_0}\right)\mathrm{d}z = \left(\frac{c'}{c_0}k_0\right)\left(\frac{k_0}{k_z}\,\mathrm{d}z\right) \,. \end{aligned} \tag{A.3.26}$$

The term $(c'/c_0)k_0$ has the form of an effective wavenumber, accounting for the dilation of contraction of the wavelength due to the difference in sound speed from c_0. The second term $(k_0/k_z)\,\mathrm{d}z$ is the distance between the two infinitesimally separated planes for a plane wave traveling with propagating wavenumber k_z. The extra phase then has a the familiar form $\phi \sim k_{\mathrm{eff}} d$.

Neglecting the first term in Eq. (A.3.20) requires that $|\mathrm{d}^2A/\mathrm{d}z^2|$ is small compared to both $|(\mathrm{d}A/\mathrm{d}z)/k_z|$ and $|\lambda|$. Evaluation of the derivatives of the found solution gives the condition as

$$\left|\frac{\mathrm{d}^2A}{\mathrm{d}z^2}\right| \sim \left|\frac{\mathrm{d}\lambda/\mathrm{d}z}{2ik_z} - \frac{\lambda^2}{4k_z^2}\right| \implies \left|\frac{\mathrm{d}\lambda/\mathrm{d}z}{2ik_z\lambda} - \frac{\lambda}{4k_z^2}\right| \le \left|\frac{\mathrm{d}\lambda/\mathrm{d}z}{2ik_z\lambda}\right| + \left|\frac{\lambda}{4k_z^2}\right| \ll 1 \,. \tag{A.3.27}$$

Now the second term that dictates $|(k_0^2/k_z^2)(1-\mu)|$ is negligible, so for $k_0 \sim k_z$ (paraxial approximation), this requirement is that $\mu \simeq 1 - c'/2c_0 \sim 1$, i.e., that the relative magnitude of the sound speed changes should be small. From the definition $\lambda =$

$k_0^2(1-\mu)$. Thus the first term then requires that

$$\begin{aligned}\left|\frac{\mathrm{d}\lambda/\mathrm{d}z}{2ik_z\lambda}\right| &= \left|\frac{k_0^2c_0^2\left[\left(1/c^3\right)\mathrm{d}c/\mathrm{d}z\right]}{2k_zk_0^2(1-\mu)}\right| \\ &= \left|\frac{1}{2k_z}\,\frac{\mathrm{d}c/\mathrm{d}z}{c}\,\frac{\mu}{(1-\mu)}\right| \\ &\leq \left|\frac{\mathrm{d}c/\mathrm{d}z}{\omega c}\,\frac{\mu}{2(1-\mu)}\right| . \end{aligned} \tag{A.3.28}$$

However, $\mu \sim 1$ is required for the second term in Eq. (A.3.27) to be satisfied. Thus to fulfill Eq. (A.3.28), it must be true that $\mathrm{d}c/\mathrm{d}z/\omega$, i.e., the sound speed change over a wavelength is a further order of magnitude smaller than $(c^2/c_0^2-1)^{-1}$. Therefore, the high frequency requirement is significantly more important than the condition that the relative changes in the sound speed are small.

Appendix B
Wave Equation Derivations

B.1 Weakly Heterogeneous Wave Equation

Derivation of the heterogeneous ASA follows from the assumption that linear acoustic propagation in a heterogeneous medium obeys[†]

$$\nabla^2 p - \frac{1}{c_0^2(\boldsymbol{r})} \frac{\partial^2 p}{\partial t^2} = 0\,, \tag{B.1.1}$$

i.e., that the constant small-signal sound speed c_0 in the homogeneous medium wave equation may be made spatially dependent. Following Ref. 263, a first-order wave equation for a heterogeneous, quiescent fluid is derived herein from the constituitive relations, and bounds on the validity of Eq. (B.1.1) are established.

B.1.1 Governing Equations

First, conservation of mass requires that the total density ϱ obeys

$$\frac{\partial \varrho}{\partial t} + \nabla \cdot (\varrho \boldsymbol{u}) = 0\,. \tag{B.1.2}$$

If the acoustic density ρ is small compared to the ambient density ρ_0, we have from Eq. (B.1.2)

$$\begin{aligned} \frac{\partial}{\partial t}(\rho_0 + \rho) + \nabla \cdot [(\rho_0 + \rho)\,\boldsymbol{u}] &= 0 \\ \frac{\partial \rho}{\partial t} + \nabla \cdot (\rho_0 \boldsymbol{u}) + \nabla \cdot (\underline{\rho \boldsymbol{u}}) &= 0\,. \end{aligned} \tag{B.1.3}$$

[†]Note that in this section c_0 is spatially varying property of the medium, as are ρ_0 and p_0. It should not be confused with its use as a constant reference sound speed.

Neglecting the second-order (underlined) term in Eq. (B.1.3) leaves

$$\frac{\partial \rho}{\partial t} + \rho_0 \nabla \cdot \boldsymbol{u} + \nabla \rho_0 \cdot \boldsymbol{u} = 0 \tag{B.1.4}$$

(note the term proportional to $\nabla \rho_0$ must be retained, since the density may vary with position). Similarly, the momentum conservation equation is

$$\varrho \frac{\mathrm{D}\boldsymbol{u}}{\mathrm{D}t} + \nabla p_{\mathrm{tot}} = \mathbf{f}, \tag{B.1.5}$$

where $\mathbf{f}$ is the total static body force per unit volume acting on the fluid and $\mathrm{D}/\mathrm{D}t$ is the material derivative. For the unforced case of interest, $\mathbf{f}$ is uniformly 0. Writing the total density $\varrho = \rho_0 + \rho$ and total pressure $p_{\mathrm{tot}} = p_0 + p$ as small perturbations of the ambient values, from Eq. (B.1.5),

$$\begin{aligned}
(\rho_0 + \rho)\left(\frac{\partial}{\partial t} + \boldsymbol{u} \cdot \nabla\right)\boldsymbol{u} + \nabla(p_0 + p) &= 0 \\
(\rho_0 + \rho)\left[\frac{\partial \boldsymbol{u}}{\partial t} + (\boldsymbol{u} \cdot \nabla)\boldsymbol{u}\right] + \nabla p_0 + \nabla p &= 0 \\
\rho_0 \frac{\partial \boldsymbol{u}}{\partial t} + \underline{\rho_0(\boldsymbol{u} \cdot \nabla)\boldsymbol{u}} + \underline{\rho \frac{\partial \boldsymbol{u}}{\partial t}} + \underline{\rho\,(\boldsymbol{u} \cdot \nabla)\boldsymbol{u}} + \nabla p_0 + \nabla p &= 0\,.
\end{aligned} \tag{B.1.6}$$

Again discarding the higher-order (underlined) terms in Eq. (B.1.6) and noting that $\nabla p_0 = -\mathbf{f} = 0$ gives

$$\rho_0 \frac{\partial \boldsymbol{u}}{\partial t} + \nabla p = 0\,. \tag{B.1.7}$$

Finally, to obtain an equation of state, assume that the *local* entropy s is unchanged by the passing sound wave (i.e., the compression is adiabatic and lossless), but that the entropy may vary over the propagation distance. Since the total pressure is a function of density and entropy,

$$\frac{\mathrm{D}P}{\mathrm{D}t} = \frac{\mathrm{D}}{\mathrm{D}t}\Big[P(\rho, s)\Big] = \left(\frac{\partial P}{\partial \rho}\right)_s \frac{\mathrm{D}\varrho}{\mathrm{D}t} + \left(\frac{\partial P}{\partial s}\right)_\varrho \frac{\mathrm{D}s}{\mathrm{D}t}\,. \tag{B.1.8}$$

Note that constant (local) entropy means that $\mathrm{D}s/\mathrm{D}t = 0$, and define $c_0^2 \equiv \partial p/\partial \rho$ as usual (although it may now vary in space). Then Eq. (B.1.8) becomes

$$\frac{\mathrm{D}P}{\mathrm{D}t} = c_0^2 \frac{\mathrm{D}\varrho}{\mathrm{D}t}\,. \tag{B.1.9}$$

Finally, writing the pressure and density as perturbations and discarding second-order terms gives

$$\frac{\mathrm{D}}{\mathrm{D}t}(p_0 + p) = c_0^2 \frac{\mathrm{D}}{\mathrm{D}t}(\rho_0 + \rho)$$
$$\left[\frac{\partial}{\partial t} + (\boldsymbol{u} \cdot \nabla)\right](p_0 + p) = c_0^2 \left[\frac{\partial}{\partial t} + (\boldsymbol{u} \cdot \nabla)\right](\rho_0 + \rho)$$
$$\underline{\underline{\frac{\partial p_0}{\partial t}}} + \boldsymbol{u} \cdot \nabla p_0 + \frac{\partial p}{\partial t} + \underline{\boldsymbol{u} \cdot \nabla p} =$$
$$c_0^2 \left[\underline{\underline{\frac{\partial \rho_0}{\partial t}}} + \boldsymbol{u} \cdot \nabla \rho_0 + \frac{\partial \rho}{\partial t} + \underline{\boldsymbol{u} \cdot \nabla \rho}\right] . \tag{B.1.10}$$

Twice underlined terms are 0 (since the medium properties are constant in time) and the terms underlined once are of second order. Then, since $\nabla p_0 = 0$ in the unforced case, we are left then with just

$$\frac{\partial p}{\partial t} = c_0^2 \left(\boldsymbol{u} \cdot \nabla \rho_0 + \frac{\partial \rho}{\partial t}\right) . \tag{B.1.11}$$

B.1.2 Wave Equation

To obtain a wave equation, first rearrange Eq. (B.1.4) to solve for $\partial\rho/\partial t$:

$$\frac{\partial \rho}{\partial t} = -\rho_0 \nabla \cdot \boldsymbol{u} - \nabla \rho_0 \cdot \boldsymbol{u} , \tag{B.1.12}$$

and substitute into Eq. (B.1.11)

$$\begin{aligned} \frac{\partial p}{\partial t} &= c_0^2 \Big[\boldsymbol{u} \cdot \nabla \rho_0 - (\rho_0 \nabla \cdot \boldsymbol{u} + \nabla \rho_0 \cdot \boldsymbol{u})\Big] \\ &= -\rho_0 c^2 \nabla \cdot \boldsymbol{u} . \end{aligned} \tag{B.1.13}$$

Taking the divergence of Eq. (B.1.7) gives

$$\rho_0 \nabla \cdot \frac{\partial \boldsymbol{u}}{\partial t} + \nabla^2 p = 0 , \tag{B.1.14}$$

and the time derivative of Eq. (B.1.13) is

$$\frac{\partial^2 p}{\partial t^2} = -\rho_0 c^2 \, \nabla \cdot \frac{\partial \boldsymbol{u}}{\partial t} \tag{B.1.15}$$

since $\partial p_0/\partial t = 0$. Taking the divergence of Eq. (B.1.13) becomes

$$\frac{\partial}{\partial t}\nabla p = -\nabla\left(\rho_0 c_0^2 \nabla\cdot\boldsymbol{u}\right). \tag{B.1.16}$$

Now, substitution of Eq. (B.1.12) into the time derivative of Eq. (B.1.7) gives

$$\rho_0\frac{\partial^2\boldsymbol{u}}{\partial t^2} + \frac{\partial}{\partial t}\nabla p = 0\,. \tag{B.1.17}$$

Subtracting Eq. (B.1.16) from Eq. (B.1.17),

$$\rho_0\frac{\partial^2\boldsymbol{u}}{\partial t^2} = \nabla\left(\rho_0 c_0^2\nabla\cdot\boldsymbol{u}\right). \tag{B.1.18}$$

Expanding the last term on the right of Eq. (B.1.18) gives

$$\begin{aligned}
\nabla\left(\rho_0 c_0^2\nabla\cdot\boldsymbol{u}\right) &= \rho_0 c_0^2\nabla^2\boldsymbol{u} + \nabla\left(\rho_0 c_0^2\right)\cdot(\nabla\cdot\boldsymbol{u}) \\
&= \rho_0 c_0^2\nabla^2\boldsymbol{u} + \left[c_0^2\nabla\rho_0 + 2\rho_0 c_0\nabla c_0\right]\cdot(\nabla\cdot\boldsymbol{u}) \\
&= \rho_0 c_0^2\left[\nabla\boldsymbol{u} + \left(\frac{1}{\rho_0}\nabla\rho_0 + \frac{2}{c_0}\nabla c_0\right)\right]\cdot(\nabla\cdot\boldsymbol{u}) \\
&= \rho_0 c_0^2\left[\nabla^2\boldsymbol{u} + \nabla(\ln\rho_0 c_0^2)\cdot(\nabla\cdot\boldsymbol{u})\right],
\end{aligned} \tag{B.1.19}$$

where $\nabla^2\boldsymbol{u}$ indicates the Laplacian of each component of $\boldsymbol{u}$. Substituting Eq. (B.1.19) into Eq. (B.1.18) gives

$$\begin{aligned}
\rho_0\frac{\partial^2\boldsymbol{u}}{\partial t^2} &= \rho_0 c_0^2\left[\nabla^2\boldsymbol{u} + \nabla(\ln\rho_0 c_0^2)\cdot(\nabla\cdot\boldsymbol{u})\right] \\
\implies \nabla^2\boldsymbol{u} - \frac{1}{c_0^2}\frac{\partial^2\boldsymbol{u}}{\partial t^2} &= \nabla(\ln\rho_0 c_0^2)\cdot(\nabla\cdot\boldsymbol{u})\,.
\end{aligned} \tag{B.1.20}$$

Thus in the absence of external forcing, and since the two terms on the left of Eq. (B.1.20) are of the same order, we can say that Eq. (B.1.1) is valid when

$$\left|\nabla(\ln\rho_0 c_0^2)\right| = \left|\frac{\nabla\rho_0}{\rho_0} + \frac{2\nabla c_0}{c_0}\right| \ll \ell^{-1}, \tag{B.1.21}$$

where ℓ is the characteristic length, i.e., the wavelength. Thus density and sound speed must each change over scales that are large compared to the wavelength.[37] Finally, from momentum equation Eq. (B.1.7) it is seen that for harmonic fields, Eq. (B.1.20) is valid for p under the same conditions.

B.2 Nonlinear Wave Equations

While the Westervelt equation [Eq. (6.2.2), repeated here]

$$\nabla^2 p - \frac{1}{c_0^2}\frac{\partial^2 p}{\partial t^2} = -\frac{\delta}{c_0^4}\frac{\partial^3 p}{\partial t^3} - \frac{\beta}{\rho_0 c_0^4}\frac{\partial^2 p^2}{\partial t^2}\,, \tag{B.2.1}$$

captures several phenomena. A sketch of its derivation (after Ref. 204) is presented here to highlight its underpinning assumptions and inform its use in this context; see that reference for a more rigorous presentation.

B.2.1 Governing Equations

As for the linear wave equation, the Westervelt equation is derived from constitutive equations

Mass Conservation:

$$\frac{\mathrm{D}\varrho}{\mathrm{D}t} + \varrho\nabla\cdot\boldsymbol{u} = 0 \tag{B.2.2}$$

Momentum Conservation:

$$\varrho\frac{\mathrm{D}\boldsymbol{u}}{\mathrm{D}t} + \nabla p_{\mathrm{tot}} = \mu\nabla^2\boldsymbol{u} + \left(\mu_B + \frac{1}{3}\mu\right)\nabla\left(\nabla\cdot\boldsymbol{u}\right) \tag{B.2.3}$$

Entropy Equation:

$$\varrho T\frac{\mathrm{D}s}{\mathrm{D}t} = \kappa^2\nabla^2 T + \mu_B\left(\nabla\cdot\boldsymbol{u}\right)^2 + \frac{1}{2}\mu\left(\frac{\partial u_j}{\partial x_k} + \frac{\partial u_k}{\partial x_j} - \frac{2}{3}\delta_{jk}\frac{\partial u_k}{\partial x_k}\right)^2 \tag{B.2.4}$$

Equation of State:

$$p_{\mathrm{tot}} = p_{\mathrm{tot}}(\varrho, s)\,, \tag{B.2.5}$$

where $c_0^2 \equiv (\partial P/\partial\rho)_s$ is the small signal sound speed, s is the entropy, T is the termperature, μ is the viscosity, and μ_B is the bulk viscosity. In Eq. (B.2.4), $u_j = \boldsymbol{u}\cdot\boldsymbol{e}_j$, $x_j = \boldsymbol{r}\cdot\boldsymbol{e}_j$, and δ_{jk} is the Kronecker delta.

B.2.2 Second Order Approximations

Introduce two ordering parameters: the Mach number $\epsilon \equiv |\boldsymbol{u}|/c_0$ and the viscosity parameter $\eta \equiv \mu\omega/\rho_0 c_0^2$. These numbers describe relative importance of large amplitude effects and viscosity relative to pressure, respectively. Then expansions of the pressure ($p_{\mathrm{tot}} = p_0 + p$), density ($\varrho = \rho_0 + \rho$), temperature ($T_{\mathrm{tot}} = T_0 + T$), and entropy

($s_{\text{tot}} = s_0 + s$) and expansion of the material derivative allow Eq. (B.2.2) to be written

$$\frac{\partial \rho}{\partial t} + \rho_0 \nabla \cdot \boldsymbol{u} + \underbrace{\rho \nabla \cdot \boldsymbol{u} + \boldsymbol{u} \cdot \nabla \rho}_{\text{Second Order Terms}} . = 0 \tag{B.2.6}$$

Since there are no third order terms, Eq. (B.2.2) remains exactly true. The same substitutions for and retention of terms of second order[†] in Eq. (B.2.3) gives

$$\rho_0 \frac{\partial \boldsymbol{u}}{\partial t} + \nabla p = \mu \nabla^2 \boldsymbol{u} + \left(\mu_B + \frac{1}{3}\mu\right) \nabla^2 \boldsymbol{u} - \frac{1}{2}\rho_0 \nabla u^2 - \rho \frac{\partial \boldsymbol{u}}{\partial t} . \tag{B.2.7}$$

In arriving at Eq. (B.2.7) it is assumed that we are considering points sufficiently far from any boundaries. Here, "sufficiently far" specifically means that $e^{-x/\ell_v}/\eta \ll 1$, where ℓ_v is a characteristic length of the vorticity of the field.[‡] The assumption of sufficient distance from boundaries also implies that the dominant contribution to the temperature fluctuations are due to acoustic disturbances, and thus to second order Eq. (B.2.4)

$$\rho_0 T_0 \frac{\partial s}{\partial t} = \kappa \nabla^2 T . \tag{B.2.8}$$

Finally, expanding the generic equation of state Eq. (B.2.5)

$$\begin{aligned} p_{\text{tot}} - p_0 &= c_0^2 (\varrho - \rho_0) + \frac{c_0^2}{\rho_0} (\varrho - \rho_0)^2 + \left(\frac{\partial p_{\text{tot}}}{\partial s}\right)_{\rho_0} (s_{\text{tot}} - s_0) \\ \implies \quad p &= c_0^2 \rho + \frac{c_0^2}{\rho_0} \frac{B}{2A} \rho^2 + \left(\frac{\partial p_{\text{tot}}}{\partial s}\right)_{\rho_0} s , \end{aligned} \tag{B.2.9}$$

where $B/2A$ is called the parameter of nonlinearity. While entirely semantic, the distinction will be made between the parameter of nonlinearity ($B/2A$) and nonlinear parameter ($\beta = 1 + B/2A$).

[†]That is, terms of $\mathcal{O}(\epsilon^2)$, $\mathcal{O}(\epsilon^2)$, $\mathcal{O}(\epsilon\eta)$ are kept, but terms $\mathcal{O}(\epsilon^2\eta)$ or $\mathcal{O}(\epsilon^3)$ are discarded.

[‡]The specific requirements arise from expansions $\nabla(\nabla\cdot\boldsymbol{u}) = \nabla^2\boldsymbol{u} + \nabla\times\nabla\times\boldsymbol{u}$ and $(\boldsymbol{u}\cdot\nabla)\boldsymbol{u} = \frac{1}{2}\nabla u^2 - \boldsymbol{u}\times\nabla\times\boldsymbol{u}$. Then it is assumed that the vorticity is the primary contribution of to the total rotational particle velocity compared to acoustic or thermal motion, i.e., that $\nabla\times\boldsymbol{u} \simeq \nabla\times\boldsymbol{u}_v$. Comparing the magnitudes of the cross product terms to ∇u^2 leads to the stated condition (which is the stronger of two in fact: neglecting one of these terms requires only that $e^{-x/\ell_v}/\sqrt{\eta} \ll 1$).

B.2.2.1 First Order Substitutions

A benefit of the ordering scheme used is that first order relations may be used in the second order equations. For instance, consider the first term of Eq. (B.2.2), which is a second order term. Since $\rho = c_0^{-2} p + \mathcal{O}(\bar{\epsilon}^2)^{\dagger}$ and $\nabla \cdot \boldsymbol{u} = -\rho_0^{-1} \partial\rho/\partial t + \mathcal{O}(\bar{\epsilon}^2)$,

$$\begin{aligned}
-\rho \nabla \cdot \boldsymbol{u} &= -\left(\frac{p}{c_0^2} + \mathcal{O}(\bar{\epsilon}^2)\right)\left(-\frac{1}{\rho_0}\frac{\partial \rho}{\partial t} + \mathcal{O}(\bar{\epsilon}^2)\right) \\
&= \underbrace{\frac{p}{c_0^2} \cdot \frac{1}{\rho_0}\frac{\partial \rho}{\partial t}}_{\mathcal{O}(\bar{\epsilon}^2)} - \underbrace{\left[\frac{p}{c_0^2}\mathcal{O}(\bar{\epsilon}^2) - \frac{1}{\rho_0}\frac{\partial \rho}{\partial t}\mathcal{O}(\bar{\epsilon}^2)\right]}_{\mathcal{O}(\bar{\epsilon}^3)} + \mathcal{O}(\bar{\epsilon}^4) \\
&= \frac{p}{c_0^2} \cdot \frac{1}{\rho_0}\left[\frac{1}{c_0^2}\frac{\partial p}{\partial t} + \mathcal{O}(\bar{\epsilon}^2)\right] + \mathcal{O}(\bar{\epsilon}^3) \\
&= \frac{p}{\rho_0 c_0^4}\frac{\partial p}{\partial t} + \mathcal{O}(\bar{\epsilon}^3)\,. \qquad \text{(B.2.10)}
\end{aligned}$$

Thus, in all second-order terms, first order approximations for quantities may be substituted as is convenient while third-order accuracy is maintained. If the Lagrangian density is defined

$$\mathcal{L} \equiv \frac{1}{2}\rho_0 u^2 - \frac{p^2}{2\rho_0 c_0}\,, \qquad \text{(B.2.11)}$$

then it may be shown[242] that Eq. (B.2.6) may be written

$$\frac{\partial \rho}{\partial t} + \rho_0 \nabla \cdot \boldsymbol{u} = \frac{p}{\rho_0 c_0^4}\frac{\partial p^2}{\partial t} + \frac{1}{c_0^2}\frac{\partial \mathcal{L}}{\partial t}\,, \qquad \text{(B.2.12)}$$

and that Eq. (B.2.7) may be written

$$\rho_0 \frac{\partial \boldsymbol{u}}{\partial t} + \nabla p = -\frac{1}{\rho_0 c_0^4}\left(\mu_B + \frac{4}{3}\mu\right)\nabla \frac{\partial p}{\partial t} - \nabla \mathcal{L}\,. \qquad \text{(B.2.13)}$$

[†]Here, $\bar{\epsilon}$ is a generic ordering parameter that is defined similarly to and has magnitude of the same order as the Mach number ϵ and viscosity parameter η.

Finally, the entropy and state equations [Eq. (B.2.8) and Eq. (B.2.9), respectively] may be combined, and after using thermodynamic relations, yield

$$\rho = \frac{p}{c_0^2} - \frac{1}{\rho_0 c_0^4}\frac{B}{2A}p^2 - \frac{\kappa}{\rho_0 c_0^4}\left(\frac{1}{C_v} - \frac{1}{C_p}\right)\frac{\partial p}{\partial t}, \tag{B.2.14}$$

where C_p and C_v are the specific heats at constant pressure and volume, respectively.

B.2.2.2 Westervelt Equation

Manipulation of Eqs. (B.2.12) to (B.2.14), elimination of ρ, as well as a final first order substitution for $\nabla^2 p = c_0^{-2}\partial^2 p/\partial t^2$ gives

$$\nabla^2 p - \frac{1}{c_0^2}\frac{\partial^2 p}{\partial t^2} + \frac{\delta}{c_0^4}\frac{\partial^3 p}{\partial t^3} = -\frac{\beta}{\rho_0 c_0^4}\frac{\partial p^2}{\partial t} - \left(\nabla^2 + \frac{1}{c_0^2}\frac{\partial^2}{\partial t^2}\right)\mathcal{L}, \tag{B.2.15}$$

where δ is termed the sound diffusivity

$$\delta \equiv \frac{1}{\rho_0}\left(\frac{4}{3}\mu + \mu_B\right) + \frac{\kappa}{\rho_0}\left(\frac{1}{C_v} - \frac{1}{C_p}\right). \tag{B.2.16}$$

Comparing Eq. (B.2.15) with Eq. (B.2.1), the canonical Westervelt equation apparently omits the term containing the Lagrangian density. To understand why, note that $\mathcal{L}$ may be written in terms of the velocity potential[242]

$$\mathcal{L} = \frac{\rho_0}{4}\left(\nabla^2 - \frac{1}{c_0^2}\frac{\partial^2}{\partial t^2}\right)\phi^2. \tag{B.2.17}$$

Then, Eq. (B.2.15) can be written

$$\left(\nabla^2 - \frac{1}{c_0^2}\frac{\partial^2}{\partial t^2}\right)\left[p + \frac{\rho_0}{4}\left(\nabla^2 - \frac{1}{c_0^2}\frac{\partial^2}{\partial t^2}\right)\phi^2\right] + \frac{\delta}{c_0^4}\frac{\partial^3 p}{\partial t^3} = -\frac{\beta}{\rho_0 c_0^4}\frac{\partial p^2}{\partial t}. \tag{B.2.18}$$

Now if the bracketed term is introduced as an auxiliary variable $\bar{p}$, then

$$\frac{\partial \bar{p}^2}{\partial t} = \frac{\partial p^2}{\partial t} + \mathcal{O}(\bar{\epsilon}^3) \tag{B.2.19}$$

and

$$\frac{\partial^3 \bar{p}}{\partial t^3} = \frac{\partial^3 p}{\partial t^3} + \mathcal{O}(\bar{\epsilon}^3), \tag{B.2.20}$$

and so to second order,

$$\nabla^2\bar{p} - \frac{1}{c_0^2}\frac{\partial^2\bar{p}}{\partial t^2} + \frac{\delta}{c_0^4}\frac{\partial^3\bar{p}}{\partial t^3} = -\frac{\beta}{\rho_0 c_0^4}\frac{\partial\bar{p}^2}{\partial t}\,. \tag{B.2.21}$$

Thus the Westervelt equation is valid when $\bar{p} \simeq p$. This approximation turns out to be satisfied when the nonlinear effects that accumulate as the wave propagates dominate over nonlinear effects that occur locally due to the disturbance;[264] Neglecting these local effects is usually safe for locations more than a wavelength from the source,[204] which is the case for the nonlinear cases of interest here, and thus the Westervelt equation [Eq. (B.2.1)] can be taken to capture the relevant physics.

B.2.2.3 KZK Equation

The KZK equation is a simplification of the full nonlinear wave equation under the assumptions of high frequency sources that generate fields correspondingly high directionality (i.e., sound beams). In this case, if it is required that the effects of diffraction occur at second order (as are the contributions of absorption and nonlinearity), then it may be shown[†] the governing equation is Eq. (6.2.7), repeated here

$$\frac{\partial^2 p}{\partial z \partial \tau} = \frac{c_0}{2}\nabla_\perp^2 p + \frac{\delta}{2c_0^2}\frac{\partial^3 p}{\partial \tau^3} + \frac{\partial^2 p^2}{\partial \tau^2}\,, \tag{B.2.22}$$

where $\tau = t - z/c_0$, and $\nabla_\perp^2 = \partial^2/\partial x^2 + \partial^2/\partial y^2$.

[†]This is accomplished by requiring that the field changes are slow in the axial direction relative to the transverse. Then, scaling the spatial coordinates as $(x', y', z') = (\sqrt{\epsilon}x, \sqrt{\epsilon}y, z)$ and transforming the time as $\tau = t - z/c_0$ and evaluating the Laplacian, to show they are are of the same order. Discarding higher order terms and transforming back to the unprimed coordinates gives Eq. (B.2.22).

Appendix C
Singular Value Decomposition Filter

The use of the singular value decomposition (SVD) filter is a type of principal component analysis that has seen widespread in ultrasound imaging to separate pixel intensities that fluctuate rapidly in time (e.g., those due to stochastic reflections from microbubbles or changing due to perfusion) from more static scattering (e.g., from the surrounding tissue).[265] Its use for this purpose was proposed in Ref. 266, drawing on recent advances in computational techniques[267] to allow the large resultant matrices to be manipulated, and a brief review of its formulation a is provided herein.

C.1 Concept

Consider reshaping each frame of a series into a column vector, and forming a single matrix (termed the Casorati matrix, see Fig. C.1) by appending the column vectors from each frame. Now each row of the matrix represents a time series of a pixel's intensity throughout the acquisition. It turns out that any real valued matrix S (see

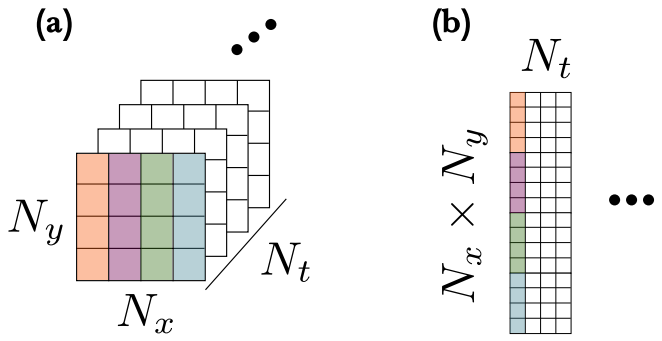

Figure C.1: **(a)** The stack of N_t ultrasound frames comprises many N_x-by-N_y–pixel frames. **(b)** The Casorati matrix reshapes these data to a 2D matrix.

Sec. C.2) may be written

$$S = U\Sigma V^{\mathsf{T}}, \tag{C.1.1}$$

where Σ is a diagonal matrix of the singular values of S. Reference 266 demonstrates that the columns of U and V represent the spatial and temporal singular vectors of S. Thus the spatiotemporal intensity of a pixel s is given by

$$s(x,y,t) = \sum_i \sigma_i \cdot I_i(x,y)\, V_i(t), \tag{C.1.2}$$

where V_i is the i^{th} column of the matrix V in Eq. (C.1.1), and I_i represent "basis" intensity distributions from the spatial singular vectors V_i. The largest singular vectors are those that correspond to slowly-changing signals (high spatial coherence between frames). Since σ_i is monotonically decreasing, setting the first few singular values, applying a high pass filter on i (that is, setting $\sigma_i = 0$ for i less than some threshold) will remove more stationary signal from the images.

C.2 Existence of Decomposition

A brief review of the underpinnings of the SVD and a formal statement of its definition are presented here; for full details see Ref. 268. The *singular values* σ_i of a matrix $S \in \mathbb{R}^{m\times m}$ are defined as the ordered square roots of the eigenvalues of the symmetric matrix $A = S^{\mathsf{T}}S$. A few facts are now stated:

Lemma C.2.1. *The eigenvectors of A are orthogonal.*

Proof. Let $\lambda_1 \neq \lambda_2$ be the distinct eigenvalues of A associated with eigenvectors $\boldsymbol{v}_1$ and $\boldsymbol{v}_2$. Then

$$\begin{aligned}\lambda_1 \boldsymbol{v}_1 \cdot \boldsymbol{v}_2 &= (\lambda_1 \boldsymbol{v}_1)^{\mathsf{T}} \boldsymbol{v}_2 = (A\boldsymbol{v}_1)^{\mathsf{T}} \boldsymbol{v}_2 \\ &= \left(\boldsymbol{v}_1^{\mathsf{T}} A^{\mathsf{T}}\right) \boldsymbol{v}_2 = \boldsymbol{v}_1^{\mathsf{T}} \left(A^{\mathsf{T}} \boldsymbol{v}_2\right) \\ &= \boldsymbol{v}_1^{\mathsf{T}} (A\boldsymbol{v}_2) = \boldsymbol{v}_1^{\mathsf{T}} (\lambda_2 \boldsymbol{v}_2) = \lambda_2 \boldsymbol{v}_1 \cdot \boldsymbol{v}_2 .\end{aligned}$$

Thus $\lambda_1 \boldsymbol{v}_1 \cdot \boldsymbol{v}_2 = \lambda_2 \boldsymbol{v}_1 \cdot \boldsymbol{v}_2$, and since $\lambda_1 \neq \lambda_2$, $\boldsymbol{v}_1 \cdot \boldsymbol{v}_2 = 0$. Thus all eigenvectors for unique eigenvalues of A are orthogonal. □

Lemma C.2.2. *The singular values of S are real and positive.*

Proof. Let λ_n be the distinct eigenvalues of $A = S^\mathsf{T} S$ associated with eigenvectors $\boldsymbol{v}_n$, which are orthogonal by Lemma C.2.1. Then

$$\begin{aligned}\|S\boldsymbol{v}_i\|^2 = (S\boldsymbol{v}_i)^\mathsf{T} S\boldsymbol{v}_i &= \left(\boldsymbol{v}_i^\mathsf{T} S^\mathsf{T}\right) S\boldsymbol{v}_i \\ &= \boldsymbol{v}_i^\mathsf{T}\left(S^\mathsf{T} S\right)\boldsymbol{v}_i = \boldsymbol{v}_i^\mathsf{T}\left(A\boldsymbol{v}_i\right) \\ &= \lambda\|\boldsymbol{v}_i\|^2 .\end{aligned}$$

Since $\|S\boldsymbol{v}_i\|^2$ and $\|\boldsymbol{v}_i\|^2$ are positive, it must be true that $\lambda_i > 0$. Thus $\sigma_i = \sqrt{\lambda_i} \in \mathbb{R}_{>0}$. □

Lemma C.2.3. *If S has r non-zero singular values, then $\{S\boldsymbol{v}_1, \ldots, S\boldsymbol{v}_r\}$ is an orthogonal basis for the column space of S, and S has rank r.*

Proof. Since the eigenvectors $\boldsymbol{v}_i$ of A are orthogonal and the associated eigenvalues λ_i are nonzero (Lemma C.2.2),

$$(S\boldsymbol{v}_i)^\mathsf{T} \cdot \left(S\boldsymbol{v}_j\right) = \left(\boldsymbol{v}_i^\mathsf{T} S^\mathsf{T}\right) \cdot \left(S\boldsymbol{v}_j\right) = \boldsymbol{v}_i^\mathsf{T}\left(S^\mathsf{T} S\right)\boldsymbol{v}_j = \boldsymbol{v}_i^\mathsf{T}\left(A\boldsymbol{v}_j\right) = \lambda_j \boldsymbol{v}_i \cdot \boldsymbol{v}_j = 0 .$$

Thus the elements of $\{S\boldsymbol{v}_1, \ldots, S\boldsymbol{v}_r\}$ are orthogonal. Now $\|S\boldsymbol{v}_i\| = \sigma_i > 0$ for $i < r$, so none of $S\boldsymbol{v}_i$ are 0 for $i < r$, and therefore $\{S\boldsymbol{v}_1, \ldots, S\boldsymbol{v}_r\}$ are linearly independent. Finally, since any vector in the column space of S is in the span of $\{S\boldsymbol{v}_1, \ldots, S\boldsymbol{v}_r\}$, we can say that its rank is the same as the dimension of its column space, namely r. □

With Lemmas C.2.1–C.2.3 established, it can now be shown that the singular value decomposition exists.

Theorem C.2.4. *The matrix may be written $S = U\Sigma V^\mathsf{T}$, where Σ contains the ordered singular values $\sigma_1, \ldots, \sigma_r$ along the diagonal.*

Proof. From Lemma C.2.3, $\{S\boldsymbol{v}_1, \ldots, S\boldsymbol{v}_r\}$ form an orthogonal basis for the column space of S. Each element can then be normalized giving an orthonormal basis

$$\boldsymbol{u}_i = \frac{1}{A\boldsymbol{v}_i} A\boldsymbol{v}_i = \frac{A\boldsymbol{v}_i}{\sigma_i}$$

Now if $r < m$, thenadditional unit vectors may be found such that $\{\boldsymbol{u}_1, \ldots, \boldsymbol{u}_1\}$ span $\mathbb{R}^m$. Now define the matrices

$$U \equiv \begin{pmatrix} | & | & & | \\ \boldsymbol{u}_1 & \boldsymbol{u}_2 & \ldots & \boldsymbol{u}_m \\ | & | & & | \end{pmatrix} \quad \text{and} \quad V \equiv \begin{pmatrix} | & | & & | \\ \boldsymbol{v}_1 & \boldsymbol{v}_2 & \ldots & \boldsymbol{v}_n \\ | & | & & | \end{pmatrix} .$$

Because $\{\boldsymbol{u}_i\}$ and $\{\boldsymbol{v}_i\}$ are orthogonal sets, U and V are orthogonal matrices. Now

$$SV = \begin{pmatrix} | & & | & | & & | \\ S\boldsymbol{v}_1 & \dots & S\boldsymbol{v}_r & 0 & \dots & 0 \\ | & & | & | & & | \end{pmatrix} = \begin{pmatrix} | & & | & | & & | \\ \sigma_1\boldsymbol{u}_1 & \dots & \sigma_r\boldsymbol{u}_r & 0 & \dots & 0 \\ | & & | & | & & | \end{pmatrix}.$$

If Σ is defined

$$\Sigma \equiv \left(\begin{array}{cccc|c} \sigma_1 & & & 0 & \\ & \sigma_2 & & & 0 \\ & & \ddots & & \\ 0 & & & \sigma_r & \\ \hline & & 0 & & 0 \end{array}\right)$$

Then,

$$U\Sigma = \begin{pmatrix} | & & | & | & & | \\ \sigma_1\boldsymbol{u}_1 & \dots & \sigma_r\boldsymbol{u}_r & 0 & \dots & 0 \\ | & & | & | & & | \end{pmatrix} = SV$$

so that

$$U\Sigma V^{\mathsf{T}} = (SV)V^{\mathsf{T}} = S$$

which establishes the decomposition. □

C.3 The SVD Filter

The SVD filtering process for super-resolution takes the entire stack of beamformed images, and reshapes it into a 2D matrix S ("Casorati matrix") with dimensions $N_xN_z\times N_t$; thus each row of the matrix can be thought of as the intensity value of each pixel in the a frame, and the time-varying intensity of the pixel given along the columns of that row. From theorem C.2.4, this matrix S may be written in terms of the decomposition

$$S = U\Sigma V^{\mathsf{T}}. \tag{C.3.1}$$

Equation (C.3.1) may be considered as the weighted sum of the component matrices[269]

$$S = \sum_{i=1}^{r} \sigma_i\, \boldsymbol{u}_i\boldsymbol{v}_i^{\mathsf{T}}, \tag{C.3.2}$$

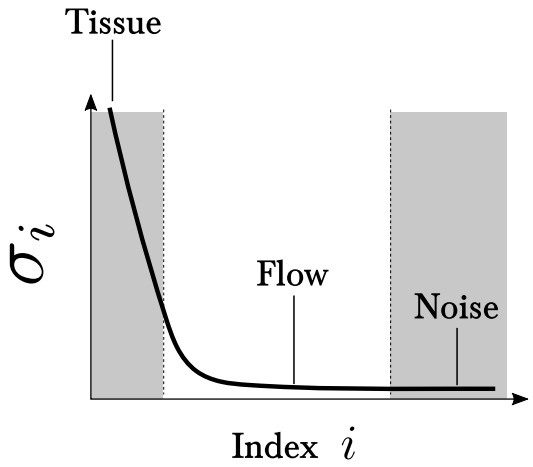

Figure C.2: The SVD filter removes the largest singular values σ_i (corresponding to tissue motion) and smallest (corresponding to noise) to enable decluttering and flow-specific imaging.

where $\boldsymbol{u}_i \in \mathbb{R}^{N_x \cdot N_z}$ is the i^{th} row of U and describes the spatial content, and $\boldsymbol{v}_i \in \mathbb{R}^{N_t}$ is the i^{th} column of V and describes the temporal content.

Qualitatively, the weight σ (i.e., the singular value) describes the spatiotemporal coherence of the pixel intensities.[266] Pixels nearby that have similar intensity throughout the acquisition (i.e., they do not change) are likely associated with tissue, wheres pixels that are not correlated in time (i.e., they change quickly and differently from other pixels) are likely due to the flow. However, the highest signular values (i.e., those that have very little spatiotemporal coherence) likely represent noise, and are also often removed from the raw data.

The SVD filter sets the few largest values of σ (those corresponding to tissue) and few smallest values of σ (those corresponding to random noise) to 0, and then reconstructs the data via Eq. (C.3.1). In this way, signal due to the tissue and noise is removed, while signal due to perfusion or flowing microbubbles is retained; see Fig. C.2 Determining the optimal cutoff values for σ is more subtle,[270] but relatively naive "brick wall" filters have demonstrated improvement over the unfiltered case.

Bibliography

[1] T. L. Szabo, *Diagnostic Ultrasound Imaging: Inside Out*, 2nd ed. Boston: Academic Press, Dec. 2013.

[2] D. L. Miller *et al.*, "Overview of Therapeutic Ultrasound Applications and Safety Considerations," *Journal of Ultrasound in Medicine*, vol. 31, no. 4, pp. 623–634, 2012.

[3] C. Chaussy *et al.*, "Extracorporeal shock-wave lithotripsy (ESWL) for treatment of urolithiasis," *Urology*, vol. 23, no. 5, Supplement, pp. 59–66, May 1984.

[4] A. Skolarikos, G. Alivizatos, and J. de la Rosette, "Extracorporeal Shock Wave Lithotripsy 25 Years Later: Complications and Their Prevention," *European Urology*, vol. 50, no. 5, pp. 981–990, Nov. 2006.

[5] M. W. Mann, M. D. Palm, and R. D. Sengelmann, "New advances in liposuction technology," *Seminars in Cutaneous Medicine and Surgery*, vol. 27, no. 1, pp. 72–82, Mar. 2008.

[6] Y. Meng, K. Hynynen, and N. Lipsman, "Applications of focused ultrasound in the brain: from thermoablation to drug delivery," *Nature Reviews Neurology*, pp. 1–16, Oct. 2020.

[7] N. McDannold *et al.*, "Transcranial Magnetic Resonance Imaging– Guided Focused Ultrasound Surgery of Brain TumorsInitial Findings in 3 Patients," *Neurosurgery*, vol. 66, no. 2, pp. 323–332, Feb. 2010.

[8] D. Jeanmonod *et al.*, "Transcranial magnetic resonance imaging–guided focused ultrasound: noninvasive central lateral thalamotomy for chronic neuropathic pain," *Neurosurgical Focus*, vol. 32, no. 1, pp. 1–11, Jan. 2012.

[9] W. J. Elias *et al.*, "A Pilot Study of Focused Ultrasound Thalamotomy for Essential Tremor," *New England Journal of Medicine*, vol. 369, no. 7, pp. 640–648, Aug. 2013.

[10] H. H. Jung *et al.*, "Bilateral thermal capsulotomy with MR-guided focused ultrasound for patients with treatment-refractory obsessive-compulsive disorder: a proof-of-concept study," *Molecular Psychiatry*, vol. 20, no. 10, pp. 1205–1211, Oct. 2015.

[11] A. Fasano *et al.*, "MRI-guided focused ultrasound thalamotomy in non-ET tremor syndromes," *Neurology*, vol. 89, no. 8, pp. 771–775, Aug. 2017.

[12] A. Carpentier *et al.*, "Clinical trial of blood-brain barrier disruption by pulsed ultrasound," *Science Translational Medicine*, vol. 8, no. 343, pp. 343re2–343re2, Jun. 2016.

[13] A. Abrahao *et al.*, "First-in-human trial of blood–brain barrier opening in amyotrophic lateral sclerosis using MR-guided focused ultrasound," *Nature Communications*, vol. 10, no. 1, pp. 1–9, Sep. 2019.

[14] N. Lipsman *et al.*, "Blood–brain barrier opening in Alzheimer's disease using MR-guided focused ultrasound," *Nature Communications*, vol. 9, no. 1, p. 2336, Jul. 2018.

[15] C. Errico *et al.*, "Ultrafast ultrasound localization microscopy for deep super-resolution vascular imaging," *Nature*, vol. 527, no. 7579, p. nature16066, Nov. 2015.

[16] J. Krejza *et al.*, "Suitability of Temporal Bone Acoustic Window: Conventional TCD Versus Transcranial Color-Coded Duplex Sonography," *Journal of Neuroimaging*, vol. 17, no. 4, pp. 311–314, 2007.

[17] E. Macé *et al.*, "Functional ultrasound imaging of the brain," *Nature Methods*, vol. 8, no. 8, pp. 662–664, Aug. 2011.

[18] C. Demene *et al.*, "Functional ultrasound imaging of brain activity in human newborns," *Science Translational Medicine*, vol. 9, no. 411, p. eaah6756, Oct. 2017.

[19] M. A. O'Reilly and K. Hynynen, "A super-resolution ultrasound method for brain vascular mapping," *Medical Physics*, vol. 40, no. 11, p. 110701, Nov. 2013.

[20] M. A. O'Reilly, R. M. Jones, and K. Hynynen, "Three-Dimensional Transcranial Ultrasound Imaging of Microbubble Clouds Using a Sparse Hemispherical Array," *IEEE transactions on bio-medical engineering*, vol. 61, no. 4, pp. 1285–1294, Apr. 2014.

[21] C. D. Arvanitis, G. T. Clement, and N. McDannold, "Transcranial Assessment and Visualization of Acoustic Cavitation: Modeling and Experimental Validation," *IEEE Transactions on Medical Imaging*, vol. 34, no. 6, pp. 1270–1281, Jun. 2015.

[22] G. F. Pinton, J. Dahl, S. Rosenzweig, and G. E. Trahey, "A heterogeneous nonlinear attenuating full- wave model of ultrasound," *IEEE Transactions on Ultrasonics, Ferroelectrics, and Frequency Control*, vol. 56, no. 3, pp. 474–488, Mar. 2009.

[23] B. E. Treeby and B. T. Cox, "k-Wave: MATLAB toolbox for the simulation and reconstruction of photoacoustic wave fields," *Journal of Biomedical Optics*, vol. 15, no. 2, p. 021314, Apr. 2010.

[24] R. J. McGough, T. V. Samulski, and J. F. Kelly, "An efficient grid sectoring method for calculations of the near-field pressure generated by a circular piston," *The Journal of the Acoustical Society of America*, vol. 115, no. 5, pp. 1942–1954, Apr. 2004.

[25] C. D. Arvanitis, C. Crake, N. McDannold, and G. T. Clement, "Passive Acoustic Mapping with the Angular Spectrum Method," *IEEE Transactions on Medical Imaging*, vol. 36, no. 4, pp. 983–993, Apr. 2017.

[26] J. W. Goodman, *Introduction to Fourier Optics*, 2nd ed. McGraw-Hill Book Company, 1996.

[27] H. Booker and P. Clemmow, "The concept of an angular spectrum of plane waves, and its relation to that of polar diagram and aperture distribution," *Proceedings of the IEE - Part III: Radio and Communication Engineering*, vol. 97, no. 45, pp. 11–17, Jan. 1950.

[28] J. W. Cooley and J. W. Tukey, "An Algorithm for the Machine Calculation of Complex Fourier Series," *Mathematics of Computation*, vol. 19, no. 90, pp. 297–301, 1965.

[29] D. Gabor and W. L. Bragg, "Microscopy by reconstructed wave-fronts," *Proceedings of the Royal Society of London. Series A. Mathematical and Physical Sciences*, vol. 197, no. 1051, pp. 454–487, Jul. 1949.

[30] Y. Jing, M. Tao, and G. T. Clement, "Evaluation of a wave-vector-frequency-domain method for nonlinear wave propagation," *The Journal of the Acoustical Society of America*, vol. 129, no. 1, pp. 32–46, Jan. 2011.

[31] K. Watanabe, *Integral Transform Techniques for Green's Function*, 2nd ed., ser. Lecture Notes in Applied and Computational Mechanics. Springer International Publishing, 2015.

[32] P. M. Morse, H. Feshbach, and G. P. Harnwell, *Methods of Theoretical Physics, Part I.* Boston, Mass: McGraw-Hill Book Company, Jun. 1953.

[33] G. P. Agrawal and C. L. Mehta, "Angular Spectrum Approach to Electromagnetic Wave propagation in Inhomogeneous Media," *Optics Communications*, vol. 14, no. 1, pp. 88–91, May 1975.

[34] S. Schoen Jr and C. D. Arvanitis, "Acoustic source localization with the angular spectrum approach in continuously stratified media," *The Journal of the Acoustical Society of America*, vol. 148, no. 4, pp. EL333–EL339, Oct. 2020.

[35] P. M. Morse and H. Feshbach, *Methods of Theoretical Physics, Part II*, 1st ed. Minneapolis, Minn: McGraw-Hill College, Jun. 1953.

[36] J. Gu and Y. Jing, "Numerical Modeling of Ultrasound Propagation in Weakly Heterogeneous Media Using a Mixed Domain Method," *IEEE Transactions on Ultrasonics, Ferroelectrics, and Frequency Control*, pp. 1–1, 2018.

[37] P. G. Bergmann, "The Wave Equation in a Medium with a Variable Index of Refraction," *The Journal of the Acoustical Society of America*, vol. 17, no. 4, pp. 329–333, Apr. 1946.

[38] H. Luke, "The origins of the sampling theorem," *IEEE Communications Magazine*, vol. 37, no. 4, pp. 106–108, Apr. 1999.

[39] H. Nyquist, "Certain Topics in Telegraph Transmission Theory," *Transactions of the American Institute of Electrical Engineers*, vol. 47, no. 2, pp. 617–644, Apr. 1928.

[40] C. Shannon, "Communication in the Presence of Noise," *Proceedings of the IRE*, vol. 37, no. 1, pp. 10–21, Jan. 1949.

[41] E. Williams, *Fourier Acoustics*. Elsevier, 1999.

[42] F. Harris, "On the use of windows for harmonic analysis with the discrete Fourier transform," *Proceedings of the IEEE*, vol. 66, no. 1, pp. 51–83, Jan. 1978.

[43] F. W. Kremkau, "Cancer therapy with ultrasound: A historical review," *Journal of Clinical Ultrasound*, vol. 7, no. 4, pp. 287–300, Aug. 1979.

[44] J. E. Kennedy, G. R. ter Haar, and D. Cranston, "High intensity focused ultrasound: surgery of the future?" *The British Journal of Radiology*, vol. 76, no. 909, pp. 590–599, Sep. 2003.

[45] F. J. Fry and J. E. Barger, "Acoustical properties of the human skull," *The Journal of the Acoustical Society of America*, vol. 63, no. 5, pp. 1576–1590, May 1978.

[46] W. J. Fry, W. H. Mosberg, J. W. Barnard, and F. J. Fry, "Production of focal destructive lesions in the central nervous system with ultrasound," *Journal of Neurosurgery*, vol. 11, no. 5, pp. 471–478, Sep. 1954.

[47] F. J. Fry *et al.*, "A Focused Ultrasound System for Tissue Volume Ablation in Deep Seated Brain Sites," in *IEEE 1986 Ultrasonics Symposium*, Nov. 1986, pp. 1001–1004.

[48] A. N. Guthkelch *et al.*, "Treatment of malignant brain tumors with focused ultrasound hyperthermia and radiation: results of a phase I trial," *Journal of Neuro-Oncology*, vol. 10, no. 3, pp. 271–284, Jun. 1991.

[49] F. J. Fry, "Transkull transmission of an intense focused ultrasonic beam," *Ultrasound in Medicine & Biology*, vol. 3, no. 2, pp. 179–184, Jan. 1977.

[50] F. J. Fry, S. A. Goss, and J. T. Patrick, "Transkull focal lesions in cat brain produced by ultrasound," *Journal of Neurosurgery*, vol. 54, no. 5, pp. 659–663, May 1981.

[51] J. G. Lynn, R. L. Zwemer, A. J. Chick, and A. E. Miller, "A NEW METHOD FOR THE GENERATION AND USE OF FOCUSED ULTRASOUND IN EXPERIMENTAL BIOLOGY," *The Journal of General Physiology*, vol. 26, no. 2, pp. 179–193, Nov. 1942.

[52] K. Hynynen, "MRI-guided focused ultrasound treatments," *Ultrasonics*, vol. 50, no. 2, pp. 221–229, Feb. 2010.

[53] K. Hynynen and R. M. Jones, "Image-guided ultrasound phased arrays are a disruptive technology for non-invasive therapy," *Physics in Medicine and Biology*, vol. 61, no. 17, pp. R206–248, 2016.

[54] S. W. Smith, D. J. Phillips, O. T. von Ramm, and F. L. Thurstone, "Some Advances in Acoustic Imaging through Skull," *Ultrasonic Tissue Characterization II*, no. 525, pp. 209–218, 1979.

[55] J. Thomas and M. A. Fink, "Ultrasonic beam focusing through tissue inhomogeneities with a time reversal mirror: application to transskull therapy," *IEEE Transactions on Ultrasonics, Ferroelectrics, and Frequency Control*, vol. 43, no. 6, pp. 1122–1129, Nov. 1996.

[56] J. Sun and K. Hynynen, "Focusing of therapeutic ultrasound through a human skull: A numerical study," *The Journal of the Acoustical Society of America*, vol. 104, no. 3, pp. 1705–1715, Sep. 1998.

[57] K. Hynynen *et al.*, "MR imaging-guided focused ultrasound surgery of fibroadenomas in the breast: a feasibility study," *Radiology*, vol. 219, no. 1, pp. 176–185, Apr. 2001.

[58] K. Hynynen, A. Darkazanli, E. Unger, and J. F. Schenck, "MRI-guided noninvasive ultrasound surgery," *Medical Physics*, vol. 20, no. 1, pp. 107–115, Jan. 1993.

[59] K. Hynynen and J. Sun, "Trans-skull ultrasound therapy: the feasibility of using image-derived skull thickness information to correct the phase distortion," *IEEE Transactions on Ultrasonics, Ferroelectrics, and Frequency Control*, vol. 46, no. 3, pp. 752–755, May 1999.

[60] J.-F. Aubry *et al.*, "Experimental demonstration of noninvasive transskull adaptive focusing based on prior computed tomography scans," *The Journal of the Acoustical Society of America*, vol. 113, no. 1, pp. 84–93, Jan. 2003.

[61] G. T. Clement, J. Sun, T. Giesecke, and K. Hynynen, "A hemisphere array for non-invasive ultrasound brain therapy and surgery," *Physics in Medicine & Biology*, vol. 45, no. 12, p. 3707, 2000.

[62] G. T. Clement and K. Hynynen, "A non-invasive method for focusing ultrasound through the human skull," *Physics in Medicine & Biology*, vol. 47, no. 8, p. 1219, 2002.

[63] K. Hynynen *et al.*, "500-element ultrasound phased array system for noninvasive focal surgery of the brain: A preliminary rabbit study with ex vivo human skulls," *Magnetic Resonance in Medicine*, vol. 52, no. 1, pp. 100–107, Jul. 2004.

[64] N. Lipsman *et al.*, "MR-guided focused ultrasound thalamotomy for essential tremor: a proof-of-concept study," *The Lancet Neurology*, vol. 12, no. 5, pp. 462–468, May 2013.

[65] T. Prabhala *et al.*, "External focused ultrasound treatment for neuropathic pain induced by common peroneal nerve injury," *Neuroscience Letters*, vol. 684, pp. 145–151, 2018.

[66] Y. Ma, G. Hsu, and F. Zhang, "The applicability and efficacy of magnetic resonance-guided high intensity focused ultrasound system in the treatment of primary trigeminal neuralgia," *Medical Hypotheses*, vol. 139, p. 109688, Jun. 2020.

[67] J.-G. Chang *et al.*, "Bilateral thermal capsulotomy with magnetic resonance-guided focused ultrasound for patients with treatment-resistant depression: A proof-of-concept study," *Bipolar Disorders*, Jun. 2020.

[68] B. Davidson *et al.*, "Magnetic resonance-guided focused ultrasound capsulotomy for refractory obsessive compulsive disorder and major depressive disorder: clinical and imaging results from two phase I trials," *Molecular Psychiatry*, pp. 1–12, May 2020.

[69] P. Fishman and N. Lipsman, "Focused ultrasound as an evolving therapy for Parkinson's disease," *Movement Disorders: Official Journal of the Movement Disorder Society*, vol. 34, no. 9, pp. 1241–1242, 2019.

[70] K. Abe *et al.*, "Magnetic resonance-guided focused ultrasound for mesial temporal lobe epilepsy: a case report," *BMC neurology*, vol. 20, no. 1, p. 160, Apr. 2020.

[71] R. Bauer *et al.*, "Noninvasive functional neurosurgery using transcranial MR imaging-guided focused ultrasound," *Parkinsonism & Related Disorders*, vol. 20, pp. S197–S199, Jan. 2014.

[72] W. Legon *et al.*, "Transcranial focused ultrasound modulates the activity of primary somatosensory cortex in humans," *Nature Neuroscience*, vol. 17, no. 2, pp. 322–329, Feb. 2014.

[73] O. Oralkan *et al.*, "Capacitive micromachined ultrasonic transducers: next-generation arrays for acoustic imaging?" *IEEE Transactions on Ultrasonics, Ferroelectrics, and Frequency Control*, vol. 49, no. 11, pp. 1596–1610, Nov. 2002.

[74] Y. Qiu *et al.*, "Piezoelectric Micromachined Ultrasound Transducer (PMUT) Arrays for Integrated Sensing, Actuation and Imaging," *Sensors*, vol. 15, no. 4, pp. 8020–8041, Apr. 2015.

[75] P. Muralt *et al.*, "Piezoelectric micromachined ultrasonic transducers based on PZT thin films," *IEEE Transactions on Ultrasonics, Ferroelectrics, and Frequency Control*, vol. 52, no. 12, pp. 2276–2288, Dec. 2005.

[76] S. H. Wong *et al.*, "Capacitive Micromachined Ultrasonic Transducers for Therapeutic Ultrasound Applications," *IEEE transactions on bio-medical engineering*, vol. 57, no. 1, pp. 114–123, Jan. 2010.

[77] D. Gross *et al.*, "A cMUT probe for ultrasound-guided focused ultrasound targeted therapy," *IEEE Transactions on Ultrasonics, Ferroelectrics, and Frequency Control*, vol. 62, no. 6, pp. 1145–1160, Jun. 2015.

[78] C. Chang *et al.*, "Acoustic lens for capacitive micromachined ultrasonic transducers," *Journal of Micromechanics and Microengineering*, vol. 24, no. 8, p. 085007, 2014.

[79] R. M. Jones *et al.*, "Echo-Focusing in Transcranial Focused Ultrasound Thalamotomy for Essential Tremor: A Feasibility Study," *Movement Disorders*, 2020.

[80] H. Weinberg and R. Burridge, "Horizontal ray theory for ocean acoustics," *The Journal of the Acoustical Society of America*, vol. 55, no. 1, pp. 63–79, Jan. 1974.

[81] M. Fink, "Time reversal of ultrasonic fields. I. Basic principles," *IEEE Transactions on Ultrasonics, Ferroelectrics, and Frequency Control*, vol. 39, no. 5, pp. 555–566, Sep. 1992.

[82] M. Fink *et al.*, "Time-reversed acoustics," *Reports on Progress in Physics*, vol. 63, no. 12, p. 1933, 2000.

[83] M. Fink, G. Montaldo, and M. Tanter, "Time Reversal Acoustics in Biomedical Engineering," *Annual Review of Biomedical Engineering*, vol. 5, pp. 465–497, Aug. 2003.

[84] M. Pernot, G. Montaldo, M. Tanter, and M. Fink, ""Ultrasonic stars" for time-reversal focusing using induced cavitation bubbles," *Applied Physics Letters*, vol. 88, no. 3, p. 034102, Jan. 2006.

[85] K. J. Haworth, J. B. Fowlkes, P. L. Carson, and O. D. Kripfgans, "Towards Aberration Correction of Transcranial Ultrasound Using Acoustic Droplet Vaporization," *Ultrasound in Medicine & Biology*, vol. 34, no. 3, pp. 435–445, Mar. 2008.

[86] J. Gâteau *et al.*, "Transcranial Ultrasonic Therapy Based on Time Reversal of Acoustically Induced Cavitation Bubble Signature," *IEEE Transactions on Biomedical Engineering*, vol. 57, no. 1, pp. 134–144, Jan. 2010.

[87] A. Kyriakou *et al.*, "A review of numerical and experimental compensation techniques for skull-induced phase aberrations in transcranial focused ultrasound," *International Journal of Hyperthermia*, vol. 30, no. 1, pp. 36–46, Feb. 2014.

[88] M. A. O'Reilly, R. M. Jones, and K. Hynynen, "Investigating a method for non-invasive ultrasound aberration correction through the skull bone," in *Medical Imaging 2014: Ultrasonic Imaging and Tomography*, vol. 9040. International Society for Optics and Photonics, Mar. 2014, p. 904013.

[89] K. Hynynen and F. A. Jolesz, "Demonstration of Potential Noninvasive Ultrasound Brain Therapy Through an Intact Skull," *Ultrasound in Medicine & Biology*, vol. 24, no. 2, pp. 275–283, Feb. 1998.

[90] J. White, G. T. Clement, and K. Hynynen, "Transcranial ultrasound focus reconstruction with phase and amplitude correction," *IEEE Transactions on Ultrasonics, Ferroelectrics, and Frequency Control*, vol. 52, no. 9, pp. 1518–1522, Sep. 2005.

[91] M. Pernot *et al.*, "In vivo transcranial brain surgery with an ultrasonic time reversal mirror," *Journal of Neurosurgery*, vol. 106, no. 6, pp. 1061–1066, Jun. 2007.

[92] A. Pulkkinen, B. Werner, E. Martin, and K. Hynynen, "Numerical simulations of clinical focused ultrasound functional neurosurgery," *Physics in Medicine and Biology*, vol. 59, no. 7, pp. 1679–1700, Mar. 2014.

[93] M. Tabei, T. D. Mast, and R. C. Waag, "Simulation of ultrasonic focus aberration and correction through human tissue," *The Journal of the Acoustical Society of America*, vol. 113, no. 2, pp. 1166–1176, Jan. 2003.

[94] R. M. Jones and K. Hynynen, "Comparison of analytical and numerical approaches for CT-based aberration correction in transcranial passive acoustic imaging," *Physics in Medicine and Biology*, vol. 61, no. 1, pp. 23–36, Nov. 2015.

[95] U. Vyas and D. Christensen, "Ultrasound beam simulations in inhomogeneous tissue geometries using the hybrid angular spectrum method," *IEEE Transactions on Ultrasonics, Ferroelectrics, and Frequency Control*, vol. 59, no. 6, pp. 1093–1100, Jun. 2012.

[96] U. Vyas, E. Kaye, and K. B. Pauly, "Transcranial phase aberration correction using beam simulations and MR-ARFI," *Medical Physics*, vol. 41, no. 3, p. 032901, Mar. 2014.

[97] S. A. Leung *et al.*, "A rapid beam simulation framework for transcranial focused ultrasound," *Scientific Reports*, vol. 9, no. 1, pp. 1–11, May 2019.

[98] V. V. Volkov and Y. Zhu, "Deterministic phase unwrapping in the presence of noise," *Optics Letters*, vol. 28, no. 22, pp. 2156–2158, Nov. 2003.

[99] R. S. C. Cobbold, *Foundations of Biomedical Ultrasound.* Oxford University Press, 2007.

[100] J. Gu and Y. Jing, "Modeling of wave propagation for medical ultrasound: a review," *IEEE Transactions on Ultrasonics, Ferroelectrics, and Frequency Control*, vol. 62, no. 11, pp. 1979–1992, Nov. 2015.

[101] B. E. Treeby, J. Jaros, A. P. Rendell, and B. T. Cox, "Modeling nonlinear ultrasound propagation in heterogeneous media with power law absorption using a k-space pseudospectral method," *The Journal of the Acoustical Society of America*, vol. 131, no. 6, pp. 4324–4336, Jun. 2012.

[102] R. Hooke, *The Posthumous Works of Robert Hooke, ... Containing His Cutlerian Lectures, and Other Discourses, Read at the Meetings of the Illustrious Royal Society. ... Illustrated with Sculptures. To These Discourses is Prefixt the Author's Life, ... Publish'd by Richard Waller.* Sam. Smith and Benj. Walford, 1705.

[103] F. A. Firestone, "The Supersonic Reflectoscope, an Instrument for Inspecting the Interior of Solid Parts by Means of Sound Waves," *The Journal of the Acoustical Society of America*, vol. 17, no. 3, pp. 287–299, Jan. 1946.

[104] J. J. Wild, "The use of ultrasonic pulses for the measurement of biologic tissues and the detection of tissue density changes," *Surgery*, vol. 27, no. 2, pp. 183–188, Feb. 1950.

[105] J. J. Wild and J. M. Reid, "Application of Echo-Ranging Techniques to the Determination of Structure of Biological Tissues," *Science*, vol. 115, no. 2983, pp. 226–230, Feb. 1952.

[106] K. T. Dussik, "Über die Möglichkeit, hochfrequente mechanische Schwingungen als diagnostisches Hilfsmittel zu verwerten," *Zeitschrift für die gesamte Neurologie und Psychiatrie*, vol. 174, no. 1, pp. 153–168, Dec. 1942.

[107] K. T. Dussik, F. Dussik, and L. Wyt, "Auf dem Wege zur Hyperphonographie des Gehirnes," *Wiener Medizinische Wochenschrift (1946)*, vol. 97, no. 38-39, pp. 425–429, Oct. 1947.

[108] R. Cobbald, *Foundations of Biomedical Ultrasound*, 1st ed. Oxford University Press, 2007.

[109] J. J. Choi *et al.*, "Non-invasive and real-time passive acoustic mapping of ultrasound-mediated drug delivery," *Physics in Medicine and Biology*, vol. 59, no. 17, pp. 4861–4877, Aug. 2014.

[110] R. M. Jones, M. A. O'Reilly, and K. Hynynen, "Transcranial passive acoustic mapping with hemispherical sparse arrays using CT-based skull-specific aberration corrections: a simulation study," *Physics in Medicine & Biology*, vol. 58, no. 14, p. 4981, 2013.

[111] M. Aryal *et al.*, "Enhancement in blood-tumor barrier permeability and delivery of liposomal doxorubicin using focused ultrasound and microbubbles: evaluation during tumor progression in a rat glioma model," *Physics in medicine and biology*, vol. 60, no. 6, pp. 2511–2527, Mar. 2015.

[112] C. D. Arvanitis *et al.*, "Mechanisms of enhanced drug delivery in brain metastases with focused ultrasound-induced blood-tumor barrier disruption." *Proceedings of the National Academy of Sciences of the United States of America*, vol. 115, no. 37, pp. E8717–E8726, Sep. 2018.

[113] C. D. Arvanitis, M. S. Livingstone, and N. McDannold, "Combined Ultrasound and MR Imaging to Guide Focused Ultrasound Therapies in the Brain," *Physics in medicine and biology*, vol. 58, no. 14, pp. 4749–4761, Jul. 2013.

[114] C. Crake *et al.*, "A dual-mode hemispherical sparse array for 3D passive acoustic mapping and skull localization within a clinical MRI guided focused ultrasound device," *Physics in Medicine & Biology*, vol. 63, no. 6, p. 065008, Mar. 2018.

[115] A. Patel, S. J. Schoen, and C. D. Arvanitis, "Closed-Loop Spatial and Temporal Control of Cavitation Activity With Passive Acoustic Mapping," *IEEE Transactions on Biomedical Engineering*, vol. 66, no. 7, pp. 2022–2031, Jul. 2019.

[116] M. Gyöngy and C. C. Coussios, "Passive Spatial Mapping of Inertial Cavitation During HIFU Exposure," *IEEE Transactions on Biomedical Engineering*, vol. 57, no. 1, pp. 48–56, Jan. 2010.

[117] C. Coviello *et al.*, "Passive acoustic mapping utilizing optimal beamforming in ultrasound therapy monitoring," *The Journal of the Acoustical Society of America*, vol. 137, no. 5, pp. 2573–2585, May 2015.

[118] R. M. Jones *et al.*, "Three-dimensional transcranial microbubble imaging for guiding volumetric ultrasound-mediated blood-brain barrier opening," *Theranostics*, vol. 8, no. 11, pp. 2909–2926, 2018.

[119] K. J. Haworth *et al.*, "Quantitative Frequency-Domain Passive Cavitation Imaging," *IEEE Transactions on Ultrasonics, Ferroelectrics, and Frequency Control*, vol. 64, no. 1, pp. 177–191, Jan. 2017.

[120] B. Treeby, F. Lucka, E. Martin, and B. T. Cox, "Equivalent-Source Acoustic Holography for Projecting Measured Ultrasound Fields Through Complex Media," *IEEE Transactions on Ultrasonics, Ferroelectrics, and Frequency Control*, vol. 65, no. 10, pp. 1857–1864, Oct. 2018.

[121] L. Deng *et al.*, "A multi-frequency sparse hemispherical ultrasound phased array for microbubble-mediated transcranial therapy and simultaneous cavitation mapping," *Physics in Medicine & Biology*, vol. 61, no. 24, p. 8476, 2016.

[122] R. M. Jones and K. Hynynen, "Advances in acoustic monitoring and control of focused ultrasound-mediated increases in blood-brain barrier permeability," *The British Journal of Radiology*, vol. 92, no. 1096, p. 20180601, Feb. 2019.

[123] S. J. Norton, B. J. Carr, and A. J. Witten, "Passive imaging of underground acoustic sources," *The Journal of the Acoustical Society of America*, vol. 119, no. 5, pp. 2840–2847, Apr. 2006.

[124] V. A. Salgaonkar, S. Datta, C. K. Holland, and T. D. Mast, "Passive cavitation imaging with ultrasound arrays," *The Journal of the Acoustical Society of America*, vol. 126, no. 6, pp. 3071–3083, Dec. 2009.

[125] K. J. Haworth *et al.*, "Passive imaging with pulsed ultrasound insonations," *The Journal of the Acoustical Society of America*, vol. 132, no. 1, pp. 544–553, Jul. 2012.

[126] P. Marmottant *et al.*, "A model for large amplitude oscillations of coated bubbles accounting for buckling and rupture," *The Journal of the Acoustical Society of America*, vol. 118, no. 6, pp. 3499–3505, Dec. 2005.

[127] L. Rayleigh, "VIII. On the pressure developed in a liquid during the collapse of a spherical cavity," *The London, Edinburgh, and Dublin Philosophical Magazine and Journal of Science*, vol. 34, no. 200, pp. 94–98, Aug. 1917.

[128] M. S. Plesset, "The Dynamics of Cavitation Bubbles," *Journal of Applied Mechanics*, vol. 16, pp. 277–282, Sep. 1949.

[129] K. E. Morgan *et al.*, "Experimental and theoretical evaluation of microbubble behavior: effect of transmitted phase and bubble size," *IEEE Transactions on Ultrasonics, Ferroelectrics, and Frequency Control*, vol. 47, no. 6, pp. 1494–1509, Nov. 2000.

[130] K. Vokurka, "On Rayleigh's model of a freely oscillating bubble. I. Basic relations," *Czechoslovak Journal of Physics B*, vol. 35, no. 1, pp. 28–40, Jan. 1985.

[131] C. D. Arvanitis, M. S. Livingstone, N. Vykhodtseva, and N. McDannold, "Controlled Ultrasound-Induced Blood-Brain Barrier Disruption Using Passive Acoustic Emissions Monitoring," *PLOS ONE*, vol. 7, no. 9, p. e45783, Sep. 2012.

[132] K. B. Bader and C. K. Holland, "Gauging the likelihood of stable cavitation from ultrasound contrast agents," *Physics in Medicine and Biology*, vol. 58, no. 1, pp. 127–144, Jan. 2013.

[133] M. Aryal, C. D. Arvanitis, P. M. Alexander, and N. McDannold, "Ultrasound-mediated blood–brain barrier disruption for targeted drug delivery in the central nervous system," *Advanced Drug Delivery Reviews*, vol. 72, no. Supplement C, pp. 94–109, Jun. 2014.

[134] T. Sun *et al.*, "Acoustic cavitation-based monitoring of the reversibility and permeability of ultrasound-induced blood-brain barrier opening," *Physics in Medicine and Biology*, vol. 60, no. 23, pp. 9079–9094, Nov. 2015.

[135] Z. Xu *et al.*, "Controlled Ultrasound Tissue Erosion," *IEEE transactions on ultrasonics, ferroelectrics, and frequency control*, vol. 51, no. 6, pp. 726–736, Jun. 2004.

[136] C. H. Farny, R. Glynn Holt, and R. A. Roy, "The Correlation Between Bubble-Enhanced HIFU Heating and Cavitation Power," *IEEE Transactions on Biomedical Engineering*, vol. 57, no. 1, pp. 175–184, Jan. 2010.

[137] P. Ghanouni *et al.*, "Transcranial MRI-Guided Focused Ultrasound: A Review of the Technologic and Neurologic Applications," *American Journal of Roentgenology*, vol. 205, no. 1, pp. 150–159, Jun. 2015.

[138] M. O. Culjat, D. Goldenberg, P. Tewari, and R. S. Singh, "A review of tissue substitutes for ultrasound imaging," *Ultrasound in Medicine & Biology*, vol. 36, no. 6, pp. 861–873, Jun. 2010.

[139] Y. N. Makov *et al.*, "Strong on-axis focal shift and its nonlinear variation in low-Fresnel-number ultrasound beams," *The Journal of the Acoustical Society of America*, vol. 119, no. 6, pp. 3618–3624, Jun. 2006.

[140] W. Lee *et al.*, "Image-Guided Transcranial Focused Ultrasound Stimulates Human Primary Somatosensory Cortex," *Scientific Reports*, vol. 5, Mar. 2015.

[141] J. M. Fitzpatrick and J. B. West, "The distribution of target registration error in rigid-body point-based registration," *IEEE Transactions on Medical Imaging*, vol. 20, no. 9, pp. 917–927, Sep. 2001.

[142] E. Abbe, "Beiträge zur Theorie des Mikroskops und der mikroskopischen Wahrnehmung," *Archiv für Mikroskopische Anatomie*, vol. 9, no. 1, pp. 413–468, Dec. 1873.

[143] L. Rayleigh, "XXXI. Investigations in optics, with special reference to the spectroscope," *The London, Edinburgh, and Dublin Philosophical Magazine and Journal of Science*, vol. 8, no. 49, pp. 261–274, Oct. 1879.

[144] B. R. Masters, *Superresolution Optical Microscopy: The Quest for Enhanced Resolution and Contrast.* Springer Nature, Mar. 2020.

[145] M. Born and E. Wolf, *Principles of Optics: Electromagnetic Theory of Propagation, Interference and Diffraction of Light.* CUP Archive, Feb. 2000.

[146] B. Huang, M. Bates, and X. Zhuang, "Super-Resolution Fluorescence Microscopy," *Annual Review of Biochemistry*, vol. 78, no. 1, pp. 993–1016, 2009.

[147] S. W. Hell *et al.*, "The 2015 super-resolution microscopy roadmap," *Journal of Physics D: Applied Physics*, vol. 48, no. 44, p. 443001, 2015.

[148] M. G. Gustafsson, D. A. Agard, and J. W. Sedat, "I5M: 3D widefield light microscopy with better than 100 nm axial resolution," *Journal of Microscopy*, vol. 195, no. Pt 1, pp. 10–16, Jul. 1999.

[149] B. Bailey, D. L. Farkas, D. L. Taylor, and F. Lanni, "Enhancement of axial resolution in fluorescence microscopy by standing-wave excitation," *Nature*, vol. 366, no. 6450, pp. 44–48, Nov. 1993.

[150] M. G. L. Gustafsson, "Surpassing the lateral resolution limit by a factor of two using structured illumination microscopy," *Journal of Microscopy*, vol. 198, no. 2, pp. 82–87, 2000.

[151] M. G. L. Gustafsson *et al.*, "Three-Dimensional Resolution Doubling in Wide-Field Fluorescence Microscopy by Structured Illumination," *Biophysical Journal*, vol. 94, no. 12, pp. 4957–4970, Jun. 2008.

[152] L. Schermelleh *et al.*, "Subdiffraction Multicolor Imaging of the Nuclear Periphery with 3D Structured Illumination Microscopy," *Science*, vol. 320, no. 5881, pp. 1332–1336, Jun. 2008.

[153] M. J. Rust, M. Bates, and X. Zhuang, "Sub-diffraction-limit imaging by stochastic optical reconstruction microscopy (STORM)," *Nature methods, Nature methods*, vol. 3, 3, no. 10, 10, pp. 793, 793–795, Oct. 2006.

[154] E. Betzig *et al.*, "Imaging Intracellular Fluorescent Proteins at Nanometer Resolution," *Science*, vol. 313, no. 5793, pp. 1642–1645, Sep. 2006.

[155] S. T. Hess, T. P. K. Girirajan, and M. D. Mason, "Ultra-High Resolution Imaging by Fluorescence Photoactivation Localization Microscopy," *Biophysical Journal*, vol. 91, no. 11, pp. 4258–4272, Dec. 2006.

[156] M. Bates, B. Huang, G. T. Dempsey, and X. Zhuang, "Multicolor Super-Resolution Imaging with Photo-Switchable Fluorescent Probes," *Science*, vol. 317, no. 5845, pp. 1749–1753, Sep. 2007.

[157] V. Sboros, C. M. Moran, S. D. Pye, and W. N. McDicken, "The behaviour of individual contrast agent microbubbles," *Ultrasound in Medicine & Biology*, vol. 29, no. 5, pp. 687–694, May 2003.

[158] O. M. Viessmann *et al.*, "Acoustic super-resolution with ultrasound and microbubbles," *Physics in Medicine & Biology*, vol. 58, no. 18, p. 6447, 2013.

[159] G. T. Clement, J. Huttunen, and K. Hynynen, "Superresolution ultrasound imaging using back-projected reconstruction," *The Journal of the Acoustical Society of America*, vol. 118, no. 6, pp. 3953–3960, Dec. 2005.

[160] A. Bar-Zion *et al.*, "Fast Vascular Ultrasound Imaging With Enhanced Spatial Resolution and Background Rejection," *IEEE transactions on medical imaging*, vol. 36, no. 1, pp. 169–180, Jan. 2017.

[161] Y. Liu, M. Lv, Y. Shu, and X. Liu, "Effect of PSF on super-resolution ultrasound imaging implemented by bSOFI method," in *SPIE/COS Photonics Asia 2018*, vol. 10820, Beijing, China, Oct. 2018, p. 95.

[162] A. Liu, X. Zhou, G. Huang, and G. Hu, "Super-resolution imaging by resonant tunneling in anisotropic acoustic metamaterials," *The Journal of the Acoustical Society of America*, vol. 132, no. 4, pp. 2800–2806, Oct. 2012.

[163] K. Christensen-Jeffries *et al.*, "Super-resolution Ultrasound Imaging," *Ultrasound in Medicine & Biology*, vol. 46, no. 4, pp. 865–891, Apr. 2020.

[164] Y. Desailly, J. Pierre, O. Couture, and M. Tanter, "Resolution limits of ultrafast ultrasound localization microscopy," *Physics in Medicine & Biology*, vol. 60, no. 22, p. 8723, 2015.

[165] W. F. Walker and G. E. Trahey, "A fundamental limit on delay estimation using partially correlated speckle signals," *IEEE Transactions on Ultrasonics, Ferroelectrics, and Frequency Control*, vol. 42, no. 2, pp. 301–308, Mar. 1995.

[166] O. Couture *et al.*, "Ultrasound Localization Microscopy and Super-Resolution: A State of the Art," *IEEE Transactions on Ultrasonics, Ferroelectrics, and Frequency Control*, vol. 65, no. 8, pp. 1304–1320, Aug. 2018.

[167] D. Ackermann and G. Schmitz, "Detection and Tracking of Multiple Microbubbles in Ultrasound B-Mode Images," *IEEE Transactions on Ultrasonics, Ferroelectrics, and Frequency Control*, vol. 63, no. 1, pp. 72–82, Jan. 2016.

[168] F. Foroozan and P. Sadeghi, "Super-resolution ultrawideband ultrasound imaging using focused frequency time reversal music," in *2015 IEEE International Conference on Acoustics, Speech and Signal Processing (ICASSP)*, Apr. 2015, pp. 887–891.

[169] G. P. Luke, A. S. Hannah, and S. Y. Emelianov, "Super-Resolution Ultrasound Imaging in Vivo with Transient Laser-Activated Nanodroplets," *Nano Letters*, vol. 16, no. 4, pp. 2556–2559, Apr. 2016.

[170] S. Vilov, B. Arnal, and E. Bossy, "Overcoming the acoustic diffraction limit in photoacoustic imaging by the localization of flowing absorbers," *Optics Letters*, vol. 42, no. 21, pp. 4379–4382, Nov. 2017.

[171] T. Opacic *et al.*, "Motion model ultrasound localization microscopy for preclinical and clinical multiparametric tumor characterization," *Nature Communications*, vol. 9, no. 1, p. 1527, Apr. 2018.

[172] K. Christensen-Jeffries *et al.*, "Microbubble Axial Localization Errors in Ultrasound Super-Resolution Imaging," *IEEE Transactions on Ultrasonics, Ferroelectrics, and Frequency Control*, vol. 64, no. 11, pp. 1644–1654, Nov. 2017.

[173] O. Couture *et al.*, "Microbubble ultrasound super-localization imaging (MUSLI)," in *2011 IEEE International Ultrasonics Symposium*, Oct. 2011, pp. 1285–1287.

[174] Y. Desailly, O. Couture, M. Fink, and M. Tanter, "Sono-activated ultrasound localization microscopy," *Applied Physics Letters*, vol. 103, no. 17, p. 174107, Oct. 2013.

[175] J. Zhu *et al.*, "A holey-structured metamaterial for acoustic deep-subwavelength imaging," *Nature Physics*, vol. 7, p. 52, Nov. 2010.

[176] K. Christensen-Jeffries *et al.*, "In Vivo Acoustic Super-Resolution and Super-Resolved Velocity Mapping Using Microbubbles," *IEEE Transactions on Medical Imaging*, vol. 34, no. 2, pp. 433–440, Feb. 2015.

[177] P. Song *et al.*, "Improved Super-Resolution Ultrasound Microvessel Imaging With Spatiotemporal Nonlocal Means Filtering and Bipartite Graph-Based Microbubble Tracking," *IEEE Transactions on Ultrasonics, Ferroelectrics, and Frequency Control*, vol. 65, no. 2, pp. 149–167, Feb. 2018.

[178] S. Harput *et al.*, "Two-Stage Motion Correction for Super-Resolution Ultrasound Imaging in Human Lower Limb," *IEEE Transactions on Ultrasonics, Ferroelectrics, and Frequency Control*, vol. 65, no. 5, pp. 803–814, May 2018.

[179] V. Hingot *et al.*, "Microvascular flow dictates the compromise between spatial resolution and acquisition time in Ultrasound Localization Microscopy," *Scientific Reports*, vol. 9, no. 1, p. 2456, Dec. 2019.

[180] F. Lin *et al.*, "3-D Ultrasound Localization Microscopy for Identifying Microvascular Morphology Features of Tumor Angiogenesis at a Resolution Beyond the Diffraction Limit of Conventional Ultrasound," *Theranostics*, vol. 7, no. 1, pp. 196–204, Jan. 2017.

[181] F. Foroozan, M. A. O'Reilly, and K. Hynynen, "Microbubble Localization for 3D Super-Resolution Ultrasound Imaging Using Curve Fitting and Deconvolution Methods," *IEEE Transactions on Biomedical Engineering*, vol. PP, no. 99, pp. 1–1, 2018.

[182] E. Bullitt *et al.*, "Computerized assessment of vessel morphological changes during treatment of glioblastoma multiforme: Report of a case imaged serially by MRA over four years," *NeuroImage*, vol. 47, no. SUPPL. 2, Aug. 2009.

[183] S. E. Shelton *et al.*, "Quantification of microvascular tortuosity during tumor evolution utilizing acoustic angiography," *Ultrasound in medicine & biology*, vol. 41, no. 7, pp. 1896–1904, Jul. 2015.

[184] M. Simons *et al.*, "State-of-the-Art Methods for Evaluation of Angiogenesis and Tissue Vascularization: A Scientific Statement From the American Heart Association," *Circulation Research*, vol. 116, no. 11, pp. e99–132, May 2015.

[185] H. W. Kuhn, "The Hungarian method for the assignment problem," *Naval Research Logistics Quarterly*, vol. 2, no. 1-2, pp. 83–97, 1955.

[186] R. M. Haralick, S. R. Sternberg, and X. Zhuang, "Image Analysis Using Mathematical Morphology," *IEEE Transactions on Pattern Analysis and Machine Intelligence*, vol. PAMI-9, no. 4, pp. 532–550, Jul. 1987.

[187] L. Vincent, "Morphological grayscale reconstruction in image analysis: applications and efficient algorithms," *IEEE Transactions on Image Processing*, vol. 2, no. 2, pp. 176–201, Apr. 1993.

[188] J. Brown *et al.*, "Investigation of microbubble detection methods for super-resolution imaging of microvasculature," in *2017 IEEE International Ultrasonics Symposium (IUS)*, Sep. 2017, pp. 1–4.

[189] ——, "Development of Simultaneous Optical Imaging and Super-Resolution Ultrasound to Improve Microbubble Localization Accuracy," in *2018 IEEE International Ultrasonics Symposium (IUS)*, Oct. 2018, pp. 1–4.

[190] N. Srebro and T. Jaakkola, "Weighted Low-rank Approximations," in *Proceedings of the Twentieth International Conference on International Conference on Machine Learning*, ser. ICML'03. Washington, DC, USA: AAAI Press, 2003, pp. 720–727.

[191] I.-K. Lee, "Curve reconstruction from unorganized points," *Computer Aided Geometric Design*, vol. 17, no. 2, pp. 161–177, Feb. 2000.

[192] R. C. Prim, "Shortest connection networks and some generalizations," *The Bell System Technical Journal*, vol. 36, no. 6, pp. 1389–1401, Nov. 1957.

[193] E. W. Dijkstra, "A Note on Two Problems in Connexion with Graphs," *Numer. Math.*, vol. 1, no. 1, pp. 269–271, Dec. 1959.

[194] J. H. Friedman, J. L. Bentley, and R. A. Finkel, "An Algorithm for Finding Best Matches in Logarithmic Expected Time," *ACM Transactions on Mathematical Software*, vol. 3, no. 3, pp. 209–226, Sep. 1977.

[195] C. C. Church, "The effects of an elastic solid surface layer on the radial pulsations of gas bubbles," *The Journal of the Acoustical Society of America*, vol. 97, no. 3, pp. 1510–1521, Mar. 1995.

[196] N. de Jong, R. Cornet, and C. T. Lancée, "Higher harmonics of vibrating gas-filled microspheres. Part one: simulations," *Ultrasonics*, vol. 32, no. 6, pp. 447–453, Nov. 1994.

[197] J. Tu *et al.*, "Microbubble Sizing and Shell Characterization Using Flow Cytometry," *IEEE transactions on ultrasonics, ferroelectrics, and frequency control*, vol. 58, no. 5, pp. 955–963, May 2011.

[198] C. Huang *et al.*, "Noninvasive Contrast-Free 3D Evaluation of Tumor Angiogenesis with Ultrasensitive Ultrasound Microvessel Imaging," *Scientific Reports*, vol. 9, no. 1, p. 4907, Mar. 2019.

[199] M. R. Lowerison *et al.*, "Ultrasound localization microscopy of renal tumor xenografts in chicken embryo is correlated to hypoxia," *Scientific Reports*, vol. 10, no. 1, pp. 1–13, Feb. 2020.

[200] T. Matsushige *et al.*, "Lessons from Vessel Wall Imaging of Intracranial Aneurysms: New Era of Aneurysm Evaluation beyond Morphology," *Neurologia medico-chirurgica*, vol. 59, no. 11, pp. 407–414, 2019.

[201] O. Solomon, R. J. v. Sloun, M. Mischi, and Y. C. Eldar, "Super-resolution Using Flow Estimation in Contrast Enhanced Ultrasound Imaging," in *ICASSP 2019 - 2019 IEEE International Conference on Acoustics, Speech and Signal Processing (ICASSP)*, May 2019, pp. 1338–1342.

[202] C. Huang *et al.*, "Short Acquisition Time Super-Resolution Ultrasound Microvessel Imaging via Microbubble Separation," *Scientific Reports*, vol. 10, no. 1, p. 6007, Apr. 2020.

[203] T. G. Muir and E. L. Carstensen, "Prediction of nonlinear acoustic effects at biomedical frequencies and intensities," *Ultrasound in Medicine & Biology*, vol. 6, no. 4, pp. 345–357, Jan. 1980.

[204] M. F. Hamilton and D. T. Blackstock, Eds., *Nonlinear Acoustics*. Acoustical Society of America, 2008.

[205] E. L. Carstensen, W. K. Law, N. D. McKay, and T. G. Muir, "Demonstration of nonlinear acoustical effects at biomedical frequencies and intensities," *Ultrasound in Medicine & Biology*, vol. 6, no. 4, pp. 359–368, Jan. 1980.

[206] G. Fubini, "Anomalie nella propagazione di ande acustiche de grande ampiezza," *Alta Frequenza*, vol. 4, pp. 530–581, 1935.

[207] F. H. Fenlon, "Derivation of the multiple frequency Bessel-Fubini series via Fourier analysis of the preshock time waveform," *The Journal of the Acoustical Society of America*, vol. 53, no. 6, pp. 1752–1754, Jun. 1973.

[208] Rayleigh, "On the pressure of vibrations," *The London, Edinburgh, and Dublin Philosophical Magazine and Journal of Science*, vol. 3, no. 15, pp. 338–346, Mar. 1902.

[209] ——, "On the momentum and pressure of gaseous vibrations, and on the connexion with the virial theorem," *The London, Edinburgh, and Dublin Philosophical Magazine and Journal of Science*, vol. 10, no. 57, pp. 364–374, Sep. 1905.

[210] R. T. Beyer, "Radiation pressure—the history of a mislabeled tensor," *The Journal of the Acoustical Society of America*, vol. 63, no. 4, pp. 1025–1030, Apr. 1978.

[211] S. J. Lighthill, "Acoustic streaming," *Journal of Sound and Vibration*, vol. 61, no. 3, pp. 391–418, Dec. 1978.

[212] N. Riley, "Acoustic Streaming," *Theoretical and Computational Fluid Dynamics*, vol. 10, no. 1, pp. 349–356, Jan. 1998.

[213] R. E. Apfel, "Acoustic Cavitation," in *Methods in Experimental Physics*, ser. Ultrasonics, P. D. Edmonds, Ed. Academic Press, Jan. 1981, vol. 19, pp. 355–411.

[214] T. G. Leighton, *The Acoustic Bubble.* San Diego: Academic Press, Inc., 1994.

[215] U. Ingard and D. C. Pridmore-Brown, "Scattering of Sound by Sound," *The Journal of the Acoustical Society of America*, vol. 28, no. 3, pp. 367–369, May 1956.

[216] P. J. Westervelt, "Scattering of Sound by Sound," *The Journal of the Acoustical Society of America*, vol. 29, no. 2, pp. 199–203, Feb. 1957.

[217] ——, "Parametric Acoustic Array," *The Journal of the Acoustical Society of America*, vol. 35, no. 4, pp. 535–537, Apr. 1963.

[218] H. O. Berktay, "Possible exploitation of non-linear acoustics in underwater transmitting applications," *Journal of Sound and Vibration*, vol. 2, no. 4, pp. 435–461, Oct. 1965.

[219] H. O. Berktay and C. A. Al-Temimi, "Virtual arrays for underwater reception," *Journal of Sound and Vibration*, vol. 9, no. 2, pp. 295–307, Mar. 1969.

[220] J. L. S. Bellin and R. T. Beyer, "Experimental Investigation of an End-Fire Array," *The Journal of the Acoustical Society of America*, vol. 34, no. 8, pp. 1051–1054, Aug. 1962.

[221] T. G. Muir and J. G. Willette, "Parametric Acoustic Transmitting Arrays," *The Journal of the Acoustical Society of America*, vol. 52, no. 5B, pp. 1481–1486, Nov. 1972.

[222] M. B. Bennett and D. T. Blackstock, "Parametric array in air," *The Journal of the Acoustical Society of America*, vol. 57, no. 3, pp. 562–568, Mar. 1975.

[223] M. Fatemi and J. F. Greenleaf, "Ultrasound-Stimulated Vibro-Acoustic Spectrography," *Science*, vol. 280, no. 5360, pp. 82–85, Apr. 1998.

[224] T. Karjalainen, J. Thierman, and K. Hynynen, "Ultrasound acoustic stimulated emission for controlling thermal surgery," in *1999 IEEE Ultrasonics Symposium. Proceedings. International Symposium (Cat. No.99CH37027)*, vol. 2, Oct. 1999, pp. 1397–1400 vol.2.

[225] E. Konofagou, J. Thierman, and K. Hynynen, "A focused ultrasound method for simultaneous diagnostic and therapeutic applications—a simulation study," *Physics in Medicine and Biology*, vol. 46, no. 11, pp. 2967–2984, Oct. 2001.

[226] M. M. Iversen *et al.*, "Low-intensity ultrasound activates vestibular otolith organs through acoustic radiation force," *The Journal of the Acoustical Society of America*, vol. 141, no. 6, pp. 4209–4219, Jun. 2017.

[227] J. Kubanek *et al.*, "Ultrasound Elicits Behavioral Responses through Mechanical Effects on Neurons and Ion Channels in a Simple Nervous System," *Journal of Neuroscience*, vol. 38, no. 12, pp. 3081–3091, Mar. 2018.

[228] F. J. Pompei, "Sound from ultrasound : the parametric array as an audible sound source," Thesis, Massachusetts Institute of Technology, 2002.

[229] H. S. Ju and Y.-H. Kim, "Near-field characteristics of the parametric loudspeaker using ultrasonic transducers," *Applied Acoustics*, vol. 71, no. 9, pp. 793–800, Sep. 2010.

[230] Y. Je, H. Lee, and W. Moon, "The impact of micromachined ultrasonic radiators on the efficiency of transducers in air." *Ultrasonics*, vol. 53, no. 6, pp. 1124–1134, Mar. 2013.

[231] Y. Je, H. Lee, K. Been, and W. Moon, "A micromachined efficient parametric array loudspeaker with a wide radiation frequency band," *The Journal of the Acoustical Society of America*, vol. 137, no. 4, pp. 1732–1743, Apr. 2015.

[232] Y. Ochiai, T. Hoshi, and I. Suzuki, "Holographic Whisper: Rendering Audible Sound Spots in Three-dimensional Space by Focusing Ultrasonic Waves," in *Proceedings of the 2017 CHI Conference on Human Factors in Computing Systems*, ser. CHI '17. New York, NY, USA: ACM, 2017, pp. 4314–4325.

[233] L. E. Kinsler, A. R. Frey, A. B. Coppens, and J. V. Sanders, *Fundamentals of Acoustics.* New York: John Wiley and Sons, Inc., 2000.

[234] R. T. Beyer, *Nonlinear Acoustics.* Acoustical Society of America, 1997.

[235] H. Hobæk, "Experimental investigation of an acoustical end-fire array," *Journal of Sound and Vibration*, vol. 6, no. 3, pp. 460–463, Nov. 1967.

[236] B. G. Lucas, J. N. Tjo/tta, and T. G. Muir, "Field of a parametric focusing source," *The Journal of the Acoustical Society of America*, vol. 73, no. 6, pp. 1966–1971, Jun. 1983.

[237] O. V. Rudenko, "The 40th anniversary of the Khokhlov-Zabolotskaya equation," *Acoustical Physics*, vol. 56, no. 4, pp. 457–466, Jul. 2010.

[238] E. A. Zabolotskaya and R. V. Khokhlov, "Quasi-plane waves in the nonlinear acoustics of confined beams," *Soviet Physics - Acoustics*, vol. 15, pp. 35–40, 1969.

[239] V. P. Kuznetsov, "Equations of Nonlinear Acoustics," *Soviet Physics - Acoustics*, vol. 16, pp. 467–470, 1971.

[240] Y. Lee and M. F. Hamilton, "Time-domain modeling of pulsed finite-amplitude sound beams," *The Journal of the Acoustical Society of America*, vol. 97, no. 2, pp. 906–917, Feb. 1995.

[241] R. O. Cleveland, M. F. Hamilton, and D. T. Blackstock, "Time-domain modeling of finite-amplitude sound in relaxing fluids," *The Journal of the Acoustical Society of America*, vol. 99, no. 6, pp. 3312–3318, Jun. 1996.

[242] S. I. Aanonsen, T. Barkve, J. N. Tjo/tta, and S. Tjo/tta, "Distortion and harmonic generation in the nearfield of a finite amplitude sound beam," *The Journal of the Acoustical Society of America*, vol. 75, no. 3, pp. 749–768, Mar. 1984.

[243] N. S. Bakhvalov, *Nonlinear Theory of Sound Beams*. New York: Amer Inst of Physics, Feb. 1987.

[244] J. Kelly and R. McGough, "A time-space decomposition method for calculating the nearfield pressure generated by a pulsed circular piston," *IEEE Transactions on Ultrasonics, Ferroelectrics, and Frequency Control*, vol. 53, no. 6, pp. 1150–1159, Jun. 2006.

[245] G. Pinton, J.-F. Aubry, M. Fink, and M. Tanter, "Effects of nonlinear ultrasound propagation on high intensity brain therapy," *Medical Physics*, vol. 38, no. 3, pp. 1207–1216, 2011.

[246] Y. Jing, T. Wang, and G. T. Clement, "A k-Space Method for Moderately Nonlinear Wave Propagation," *IEEE Transactions on Ultrasonics Ferroelectrics, and Frequency Control*, vol. 59, no. 8, pp. 1664–1673, Aug. 2012.

[247] W. Chen and S. Holm, "Fractional Laplacian time-space models for linear and nonlinear lossy media exhibiting arbitrary frequency power-law dependency," *The Journal of the Acoustical Society of America*, vol. 115, no. 4, pp. 1424–1430, Mar. 2004.

[248] K. Wang, E. Teoh, J. Jaros, and B. E. Treeby, "Modelling nonlinear ultrasound propagation in absorbing media using the k-Wave toolbox: experimental validation," in *2012 IEEE International Ultrasonics Symposium*, Oct. 2012, pp. 523–526.

[249] H. Azhari, "Appendix A: Typical Acoustic Properties of Tissues," in *Basics of Biomedical Ultrasound for Engineers*. John Wiley & Sons, Ltd, 2010, pp. 313–314.

[250] P. B. Rosnitskiy *et al.*, "Simulation of nonlinear trans-skull focusing and formation of shocks in brain using a fully populated ultrasound array with aberration correction," *The Journal of the Acoustical Society of America*, vol. 146, no. 3, pp. 1786–1798, Sep. 2019.

[251] Y. Jing, M. Tao, and J. Cannata, "An improved wave-vector frequency-domain method for nonlinear wave modeling," *IEEE Transactions on Ultrasonics, Ferroelectrics, and Frequency Control*, vol. 61, no. 3, pp. 515–524, Mar. 2014.

[252] J. Gu and Y. Jing, "Simulation of the Second-Harmonic Ultrasound Field in Heterogeneous Soft Tissue Using a Mixed-Domain Method," *IEEE Transactions on Ultrasonics, Ferroelectrics, and Frequency Control*, vol. 66, no. 4, pp. 669–675, Apr. 2019.

[253] E. M. Salomons, *Computational Atmospheric Acoustics*. Springer Science & Business Media, Nov. 2001.

[254] S. W. Lee, N. Bong, W. F. Richards, and R. Raspet, "Impedance formulation of the fast field program for acoustic wave propagation in the atmosphere," *The Journal of the Acoustical Society of America*, vol. 79, no. 3, pp. 628–634, Mar. 1986.

[255] T. Pham and B. Sadler, "Adaptive wideband aeroacoustic array processing," in *Proceedings of 8th Workshop on Statistical Signal and Array Processing*, Jun. 1996, pp. 295–298.

[256] F. B. Jensen, W. A. Kuperman, M. B. Porter, and H. Schmidt, *Computational Ocean Acoustics*, 2nd ed., ser. Modern Acoustics and Signal Processing. Springer, 2011.

[257] B. Maranda, "Efficient digital beamforming in the frequency domain," *The Journal of the Acoustical Society of America*, vol. 86, no. 5, pp. 1813–1819, Nov. 1989.

[258] P.-Y. Chen *et al.*, "Novel magnetic/ultrasound focusing system enhances nanoparticle drug delivery for glioma treatment," *Neuro-Oncology*, vol. 12, no. 10, pp. 1050–1060, Oct. 2010.

[259] C. Chi, Z. Li, and Q. Li, "Fast Broadband Beamforming Using Nonuniform Fast Fourier Transform for Underwater Real-Time 3-D Acoustical Imaging," *IEEE Journal of Oceanic Engineering*, vol. 41, no. 2, pp. 249–261, Apr. 2016.

[260] D. E. Soulioti, D. Espíndola, P. A. Dayton, and G. F. Pinton, "Super-Resolution Imaging Through the Human Skull," *IEEE Transactions on Ultrasonics, Ferroelectrics, and Frequency Control*, vol. 67, no. 1, pp. 25–36, Jan. 2020.

[261] I. Kostin and G. Panasenko, "Khokhlov–Zabolotskaya–Kuznetsov type equation: nonlinear acoustics in heterogeneous media," *Comptes Rendus Mécanique*, vol. 334, no. 4, pp. 220–224, Apr. 2006.

[262] S. Schoen Jr and C. D. Arvanitis, "Heterogeneous Angular Spectrum Method for Trans-Skull Imaging and Focusing," *IEEE Transactions on Medical Imaging*, vol. 39, no. 5, pp. 1605–1614, May 2020.

[263] D. T. Blackstock, *Fundamentals of Physical Acoustics*. John Wiley & Sons, Apr. 2000.

[264] ——, "Propagation of Plane Sound Waves of Finite Amplitude in Nondissipative Fluids," *The Journal of the Acoustical Society of America*, vol. 34, no. 1, pp. 9–30, Jan. 1962.

[265] P. Song *et al.*, "Accelerated Singular Value-Based Ultrasound Blood Flow Clutter Filtering With Randomized Singular Value Decomposition and Randomized Spatial Downsampling," *IEEE Transactions on Ultrasonics, Ferroelectrics, and Frequency Control*, vol. 64, no. 4, pp. 706–716, Apr. 2017.

[266] C. Demené *et al.*, "Spatiotemporal Clutter Filtering of Ultrafast Ultrasound Data Highly Increases Doppler and fUltrasound Sensitivity," *IEEE Transactions on Medical Imaging*, vol. 34, no. 11, pp. 2271–2285, Nov. 2015.

[267] E. J. Candès, X. Li, Y. Ma, and J. Wright, "Robust principal component analysis?" *Journal of the ACM*, vol. 58, no. 3, pp. 11:1–11:37, Jun. 2011.

[268] D. C. Lay, *Linear Algebra and Its Applications, 4th Edition*, 4th ed. Boston: Pearson, Jan. 2011.

[269] G. H. Golub and C. F. V. Loan, *Matrix Computations*, 4th ed. Baltimore: Johns Hopkins University Press, Feb. 2013.

[270] J. Baranger *et al.*, "Adaptive Spatiotemporal SVD Clutter Filtering for Ultrafast Doppler Imaging Using Similarity of Spatial Singular Vectors," *IEEE Transactions on Medical Imaging*, vol. 37, no. 7, pp. 1574–1586, Jul. 2018.

Index

Vita

Scott Schoen Jr graduated from the Franklin Public School system in 2007, in which time he studied math and physics with Tim Hoar, Elena Menize, Barbara Mitchell, and Christine Johnson, as well as music with Peter Light, Leighanne Rudsit, Mike Sartini, Nancy Schoen, and Greg Takemoto. He will join the Center for Ultrasound Research and Translation at Massachusetts General Hospital and Harvard Medical School as a research fellow in 2021.